SEISMIC REFLECTION IMAGING WITH CONVENTIONAL AND UNCONVENTIONAL SOURCES

A Dissertation

Presented to the Faculty of the Graduate School

of Cornell University

In Partial Fulfillment of the Requirements for the Degree of

Doctor of Philosophy

by

Diego Alonso Quiros Ugalde

January 2017

SEISMIC REFLECTION IMAGING WITH CONVENTIONAL AND UNCONVENTIONAL SOURCES

Diego Alonso Quiros Ugalde, Ph. D.

Cornell University 2017

This manuscript reports the results of research using both conventional and unconventional energy sources as well as conventional and unconventional analysis to image crustal structure using reflected seismic waves. The work presented here includes the use of explosions to investigate the Taiwanese lithosphere, the use of 'noise' from railroads to investigate the shallow subsurface of the Rio Grande rift, and the use of microearthquakes to image subsurface structure near an active fault zone within the Appalachian mountains.

Chapter 1 uses recordings from the land refraction and wide-angle reflection component of the Taiwan Integrated Geodynamic Research (TAIGER) project. The most prominent reflection feature imaged by these surveys is an anomalously strong reflector found in northeastern Taiwan. The goal of this chapter is to analyze the TAIGER recordings and to place the reflector into a geologic framework that fits with the modern tectonic kinematics of the region.

Chapter 2 uses railroad traffic as a source for reflection profiling within the Rio Grande rift. Here the railroad recordings are treated in an analogous way to Vibroseis recordings. These results suggest that railroad noise in general can be a valuable new tool in imaging and characterizing the shallow subsurface in environmental and geotechnical studies.

In chapters 3 and 4, earthquakes serve as the seismic imaging source. In these

studies the methodology of Vertical Seismic Profiling (VSP) is borrowed from the oil and gas industry to develop reflection images. In chapter 3, a single earthquake is used to probe a small area beneath Waterboro, Maine. In chapter 4, the same method is applied to multiple earthquakes to take advantage of the increased redundancy that results from multiple events illuminating the same structure. The latter study demonstrates how dense arrays can be a powerful new tool for delineating, and monitoring temporal changes of deep structure in areas characterized by significant seismic activity.

BIOGRAPHICAL SKETCH

Diego was born in Ciudad Quesada, Costa Rica, to Mario Quiros M.D. and Ana Ligia Ugalde. He spent his childhood and teenage years in Ciudad Quesada, where he attended Juan Bautista Solis Rodriguez and San Francisco de Asis primary schools, and Maria Inmaculada High School. His primary interests during those years where literature, science, and sports. From the age of twelve Diego represented Costa Rica in tennis and consistently ranked among the top players in the country in each age group. Through tennis, Diego would get the opportunity to travel throughout the Americas (i.e. North, South, and Central), and to attend the Olympic Games in Sydney, Australia, as part of the Costa Rican Olympic Team. At Sydney, he participated in the Olympic Youth Camp (OYC), an event organized for future athletes from all countries participating in the Sydney games. Such exposure reaffirmed Diego's desire to study and practice sports abroad.

In August 2002 Diego earned a tennis scholarship at a NCAA Division 1 school. He started his undergraduate degree in Physics at Longwood University, Virginia, where he studied until the end of his sophomore year. In August 2004, he transferred to the Florida Institute of Technology (Florida Tech) thanks to the help of scholarships in tennis, academics, and soccer, and the assistance of his parents. It was on his senior year at Florida Tech that he encountered a class in geophysics, then offered by Dr. Hamid Rassoul. Diego took the geophysics course as an independent study directed by Dr. Rassoul and enjoyed quite a bit. In December 2006 Diego received his B.Sc. in Physics from Florida Tech.

In August 2007 Diego started a Ph.D. in Physics at Florida Atlantic University (FAU) in Boca Raton, Florida. At FAU Diego met Prof. Xavier Comas from the Department of Geosciences and started assisting Prof. Comas with field work at the Everglades National Park and the Grassy Waters Preserve. Diego then took part of

laboratory experiments at the FAU Environmental Geophysics Lab where he investigated peatland gas dynamics with ground penetrating radar under the direction of Prof. Comas. The positive field experience acquired during the time working with Prof. Comas was central to Diego's decision to change his academic concentration.

In August 2009, Diego started a Ph.D. at Cornell under the direction of Prof. Larry Brown, which resulted in the dissertation presented in this manuscript.

ACKNOWLEGEMENTS

The work presented in this dissertation was not possible without the funding provided by the department of Earth and Atmospheric Sciences (EAS), the College of Engineering, the Atkinson Center for a Sustainable Future (ACSF), and the National Science Foundation (NSF). Funding received during my years at Cornell include: The College of Engineering McMullen Fellowship, research and teaching assistantships within EAS, travel grants from EAS and the Cornell Graduate School, ACSF grant AVF-U268703 and NSF grants (EAR-0410155, EAR-0943906, EAR-215789, EAR-1440036).

Many thanks are owed to individuals who have help me throughout my years at different institutions. From Florida Tech, Dr. Hamid Rassoul an introduction to geophysics and for serving as my unofficial undergraduate advisor. Marcus Hohlmann gave me my first opportunity in undergraduate research. Bill Macom for being an excellent mentor on and off the court. From Florida Atlantic University (FAU), Dr. Xavi Comas for the opportunity to do geophysical field work, for providing space in his lab, and for serving as my mentor during my time at FAU. Dr. Luc Wille and Dr. Pedro Marronetti for providing excellent instruction and advice.

At Cornell, I have been fortunate to interact with a large portion of the EAS department and with folks outside the department, many of whom I consider my friends. Thanks to all the members of the EAS community, especially to the members of the geophysics, sedimentology, and stratigraphy lab, my home for the majority of the years I spent at EAS; plenty of people have come through this lab, thanks to everyone. Thanks to everyone at the seismology lab and to everyone in 4144 Snee for opening your door for a summer. Special thanks to Prof. Rowena Lohman for involving me in the Salton Sea project, for providing me with funding, and for dedicating time to introduce some of the methods in her research. Also thanks to Prof.

Lohman and Prof. Pritchard for welcoming me into their research group meetings. Special thanks to Prof. Katie Keranen for involving me in her Ethiopia project, for providing summer support, and for the opportunity to travel throughout Ethiopia. To Prof. Emeritus Muawia Barazangi, thank you for your invaluable lessons in tectonics, seismology, history, the Middle East, and research, thank you for reading my manuscripts, and for constantly worrying about me. Thanks to Prof. Rick Allmendinger for all his help with structural geology and being supportive and understanding. Thanks to George Hade for providing me with a detailed history of the department, and countless hours of conversations about analog circuits, seismometers, and amazing field work stories. Thanks to Steve Gallow for teaching me about computer parts, Linux, software, and everything that entailed making my research work for several years while I learned enough to stand on my own. Thank you to the administrative staff, Amy Colvin, Savannah Sawyer, Judy Starr, Carol Armstrong for all your assistance, you really made everything easier for me.

Thanks to my collaborators, for providing constructive critiques and sharing many experiences, including field work. Chen Chen, Kathy Davenport, Liang Han, John Hole, Hao Kuo-Chen, David Okaya, Francis Wu, Martin Chapman, John Ebel, Doyeon Kim, Anastasija Cabolova, Ted Bertrand, Justin Starr, Walter Mooney.

Special thanks to IRIS Passcal members: Pnina Miller, George Slad, Steve Azevedo, Bridget O'Neill, Noël Barstow, Mouse Reusch, and Bruce Beaudoin, for providing tech support any time, any day, rain or shine. Thanks to Patrick Bastien for first teaching me how to program and download data from Texan recorders, it really has been a useful skill for my graduate work. Thanks to Alex Ferguson, Neil Fenning, Amy Radakovich, Jennifer Jay, Bill Barnhart, Francisco Delgado, Ole Gustafson, Frank Horowitz, Steve Bernsen, Dave Parmalee, Dylan Rose-Coss, Kyle Murray, and Susan Bilek, for providing help with field work and or logistics during deployments.

Thanks to Schlumberger for providing the Vista 3D and Omni 3D software packages, thanks to the Vista and Omni support team for their invaluable help. Many of the work presented here was facilitated by freely available software and scripts, thank you all for making it open source. Thank you to Laurie Green at Hess Corporation for giving me the opportunity of doing a summer internship at Hess.

Naturally, many friends have supported me throughout my studies. Friends made in Costa Rica, Virginia, Florida, Ithaca and some faraway places, have been vital for making my journey here as smooth as it has been. Many thanks to all who have been there for me.

Thanks to my family for supporting me, my dad and mom have given me every opportunity possible within their reach, and for that I am truly grateful. My siblings Andres, Alfonso, Mario and Irene, have always supported me as well, and for that I want to say thank you. Special thanks to Andres for spending a month in Ithaca, making sure I would not get distracted, which allowed me to write the last version of this manuscript.

Thanks to my committee. To Prof. Matt Pritchard, for giving me the chance of investigating my home country through InSAR, and for teaching me about tectonics and providing a different perspective of science. To Prof. David Hysell, for providing the opportunity of learning about radar from an engineering perspective, and for instilling that writing is one of the most fundamental aspects of being a scientist. To both Prof. Pritchard and Prof. Hysell, for being supportive of my research and for providing corrections to my dissertation.

Infinite thanks to Prof. Larry Brown. For reading the email about my interest in attending Cornell, for being patient with me and letting me learn at my own pace, for being extremely supportive in good and bad times, for teaching me about seismic deployments, seismology and pretty much everything I asked about. For sending me to

some pretty incredible places all over the world and for letting me get involved in all the field work I could get my hands on. Working with Prof. Brown has been one of the smartest decisions I have ever made, thank you for everything Larry.

TABLE OF CONTENTS

CHAPTER 1

INTRODUCTION

1.1 Introduction

Reflection seismology is a method that reflects elastic waves off the subsurface to reveal the geologic structures beneath [*Sheriff and Geldart*, 1995]. The oil and gas industry has systematically carried out reflection profiling to identify resources in the sedimentary veneer of the oceanic and continental crust. In spite of success in exploration of the sedimentary basins of the uppermost crust, reflection profiling was not widely used for studies of deep continental structure until the later 1970s [*Brown*, 2013]. Before that, the primary techniques used to image the crust and mantle were based on either the analysis of the dispersion of surface waves or the refraction of body waves as they propagate through the Earth [*Brown*, 2013]. The first reported seismic reflections obtained from the crystalline basement [*Junger*, 1951; *Widess and Taylor*, 1959] were found because seismic crews extended recording times in the course of standard exploration work [*Brewer and Oliver*, 1980]. These early examples led to more systematic attempts to explore the deep structure. The first of this new wave of geophysical exploration was the Consortium for Continental Reflection Profiling (COCORP) based at Cornell University [*Brown*, 2013]. The first COCORP full-scale field effort was completed in Hardeman County, Texas, in 1975, which found contained abundant reflections and diffractions from the deep basement [*Oliver et al.*, 1976].

Reflection profiling has evolved rapidly since the 1930's, with instrumentation, sources, and survey designs going through many iterations to this day. In 1940, most

seismic crews used 10 to 12 channels (receivers). In the late 1960s, 48 channels became common [*Sheriff and Geldart*, 1995], and today, most crews use thousands of channels and sometimes appreciably more [*Lin et al.*, 2013]. Similarly, surveys have progressed from linear profiles to areal arrays that more accurately reveal structure in three dimensions, to 4D surveys which monitor the change in seismic response with time. Sources in reflection profiling have also progressed significantly, with explosive sources giving way to more environmentally benign alternatives such as Vibroseis on land and airguns in the oceans [*Sheriff and Geldart*, 1995]. Recently, attention has turned to using unconventional energy sources, including microearthquakes and seismic 'noise' [*Draganov et al.*, 2007] in reflection imaging, made feasible by advances in recording technology, particularly the advent of nodal recording devices which can operate in large numbers while recording continuously [*Lin et al.*, 2013].

This dissertation reports the results of research using both conventional and unconventional energy sources as well as conventional and unconventional analysis to image crustal structure using reflected seismic waves. The work presented here includes the use of chemical explosions to investigate the Taiwanese lithosphere, the use of 'noise' from railroad traffic to investigate the shallow subsurface of the Rio Grande rift, and the use of microearthquake aftershocks to image subsurface structure near an active fault within the Appalachian mountains.

Chapter 1 uses recordings from the land seismic refraction and wide-angle reflection component of the Taiwan Integrated Geodynamic Research (TAIGER) project. TAIGER included three east-west seismometer deployments which traversed the key tectonic provinces of Taiwan as well as three northeast-southwest

supplementary profiles that parallel the tectonic grain of the island. Ten land explosions were recorded by the seismic profiles. The most prominent reflection feature imaged by these surveys is an anomalously strong reflector found in northeastern Taiwan, beneath Datong Township. The goal of this chapter is to analyze the TAIGER recordings and to place the reflector into a geologic framework that fits with the modern tectonic kinematics of the region.

Chapter 2 uses railroad traffic as a source for reflection profiling within the Rio Grande rift [*Quiros et al.*, 2016]. Here the railroad recordings are treated in an analogous way to Vibroseis [*Crawford et al.*, 1960] recordings, where a vibratory source impacts the surface with a range of frequencies, producing an extended seismic pulse. In the Vibroseis method, the extended pulse is "collapsed" by a cross-correlation method [*Wardell*, 1970], and in a similar way the railroad recordings are processed by a cross-correlation method to produce virtual source-gathers that are then used to produce a reflection profile of the subsurface. These results suggest that railroad noise can be a valuable new tool in imaging and characterizing the shallow subsurface in environmental and geotechnical studies.

In chapters 3 and 4, earthquakes serve as the seismic imaging source. In these studies, the methodology of Vertical Seismic Profiling (VSP) is borrowed from the oil and gas industry to develop reflection images with sources at depth [*Quiros et al.*, 2015a, 2015b]. In chapter 3, a single earthquake is used to probe a small area beneath Waterboro, Maine [*Quiros et al.*, 2015b]. In chapter 4, the same method is applied to multiple earthquakes to take advantage of the increased redundancy that results from multiple events illuminating the same structure. The latter study demonstrates how

dense arrays of modern nodal equipment can be a powerful new tool for delineating, and monitoring temporal changes of deep structure in areas characterized by significant seismic activity.

REFERENCES

Brewer, J. A., and J. E. Oliver (1980), Seismic reflection studies of deep crustal structure, *Annu. Rev. Earth Planet. Sci., 8*, 205.

Brown, L. D. (2013), From layer cake to complexity: 50 years of geophysical investigations of the Earth, *Geol. Soc. Am. Spec. Pap., 500*, 233–257.

Crawford, J., W. Doty, and M. Lee (1960), Continuous signal seismograph, *Geophysics, 25*(1), 95–105, doi:10.1190/1.1438707.

Draganov, D., K. Wapenaar, W. Mulder, J. Singer, and A. Verdel (2007), Retrieval of reflections from seismic background-noise measurements, *Geophys. Res. Lett., 34*(L04305).

Junger, A. (1951), Deep basement reflections in Big Horn County, Montana, *Geophysics*, *16*(3), 499–505.

Lin, F.-C., D. Li, R. W. Clayton, and D. Hollis (2013), High-resolution 3D shallow crustal structure in Long Beach, California: Application of ambient noise tomography on a dense seismic array, *Geophysics*, *78*(4), Q45–Q56.

Oliver, J., M. Dobrin, S. Kaufman, R. Meyer, and R. Phinney (1976), Continuous seismic reflection profiling of the deep basement, Hardeman County, Texas, *Geol. Soc. Am. Bull., 87*(11), 1537–1546.

Quiros, D., L. D. Brown, A. Cabolova, C. Chen, K. Davenport, J. Hole, L. Han, M. C. Chapman, W. Mooney, and others (2015a), Reflection Imaging using Earthquake Sources: A Novel Application of Reverse Vertical Seismic Profiling (RVSP), in *2015 SEG Annual Meeting*, Society of Exploration Geophysicists.

Quiros, D. A., A. Cabolova, L. D. Brown, C. Chen, J. E. Ebel, and J. Starr (2015b), Aftershock Imaging with Dense Arrays (AIDA) Following the Mw 4.0 Waterboro Earthquake of 16 October 2012 Maine, U.S.A., *Seismol. Res. Lett.*, doi: 10.1785/0220140169.

Quiros, D. A., L. D. Brown, and D. Kim (2016), Seismic interferometry of railroad induced ground motions: body and surface wave imaging, *Geophys. J. Int.*, *205*(1), 301–313.

Sheriff, R. E., and L. P. Geldart (1995), *Exploration seismology*, Cambridge University Press Cambridge.

Wardell, J. (1970), A comparison of land seismic sources, *Geoexploration*, *8*(3), 205–229, doi: 10.1016/0016-7142(70)90033-5.

Widess, M. B., and G. L. Taylor (1959), Seismic reflections from layering within the pre-Cambrian basement complex, Oklahoma, *Geophysics*, *24*(3), 417–425.

CHAPTER 2

THE DATONG BRIGHT SPOT: EVIDENCE OF RIFT MAGMATISM IN NORTHEASTERN TAIWAN?

2.1 Abstract

The land seismic refraction and wide-angle reflection component of the Taiwan Integrated Geodynamic Research (TAIGER) project included three east-west seismometer deployments which traversed the key tectonic provinces of Taiwan as well as three northeast-southwest supplementary profiles that parallel the tectonic grain of the island. Ten land explosions were recorded by transects T4B, T5, T6, T7, T8, and T9. The most prominent reflection feature imaged by these surveys is an anomalously strong reflector that underlies the Lishan fault at a depth of approximately 18 km near the southwest apex of the Ilan plain. Located beneath Datong Township, this unusual reflector is similar in general appearance and depth with reflection bright spots reported from other regions, most of which have been interpreted as fluid in the deep crust. The Datong bright spot (DBS) appears to represent a body that extends laterally about 13 km along the seismic profile. Furthermore, local earthquake recordings show a reflector in close proximity to the DBS at approximately the same depth. We interpret this as an extension of the DBS. We suggest that the bright spot is an intrusive body associated with the opening of the Ilan Plain as the southwest extension of the Okinawa trough.

2.2 Introduction

At present, active arc-continent collisions are occurring in East Timor, Papua New Guinea, and Taiwan [*Huang et al.*, 2000]. Taiwan, which sits on the complex

boundary between the Philippine Sea Plate (PSP) and the Eurasian Plate (EUP) is the result of oblique convergence between the Luzon Volcanic Arc (LVA) on the PSP and EUP margin. The collision has developed a young orogen that displays the entire evolution of an arc-continent collision, from initiation to collapse [*Shyu et al.*, 2005]. The complex tectonic setting exhibits a large range of kinematics. Offshore southern Taiwan the EUP plunges under the PSP, going from normal subduction to initial collision at around ~21° N. North of ~21° N the Manilla trench loses its morphological characteristics and is replaced by the deformation front of the Taiwan region [*Liu et al.*, 1997]. East of Taiwan at about 23.7° N the PSP subducts under the EUP at the foot of the Ryukyu accretionary wedge [*Wu et al.*, 2009]. North of the Ryukyu trench is the Okinawa Trough (OT), the back-arc basin of the Ryukyu subduction system [*Teng*, 1990].

Taiwan is generally divided into eight tectono-stratigraphic provinces (Fig. 2.1) that are the result of the collisional process. *Ho* [1986] refined the boundaries of these units, with the Penghu Islands (PH), formed from Pleistocene flood basalts, as the westernmost of these provinces. East of the Penghu Islands is the Coastal Plain (CP), which consists of relatively undeformed, poorly consolidated sedimentary deposits that regionally dip to the east and overlay Eurasian continental margin [*Hickman et al.*, 2002]. The Western Foothills (WF), a classic example of a fold-and-thrust belt [*Suppe*, 1980] that bounds the CP, is comprised of unmetamorphosed shallow marine sediments that are imbricated along numerous folds and thrusts that dip east to southeast [*Tillman and Byrne*, 1995]. Further east of the WF is the

Cenozoic slate belt, an uplift commonly subdivided into the Hsüehshan Range (HR) and the Backbone

Range (BR). The HR consists of thick sequences of Eocene and Oligocene sedimentary rocks, metamorphosed at prehnite-pumpellyite facies in the west and to lower greenschist facies in the east [*Gourley et al.*, 2007]. The eastern zone of the slate belt, the Backbone Range, is dominated by slate and phyllite, rocks more intensely metamorphosed than in the HR [*Ho*, 1986]. The two ranges are divided by the Lishan Fault (LF), a fault zone which has been given many interpretations, perhaps reflecting a polyphase history [*Lee et al.*, 1997]. The LF follows the deeply incised Lanyang valley and extends from central Taiwan to the southwest apex of the Ilan Plain [*Kuo-Chen et al.*, 2015, p.]. The Ilan Plain (IP), usually attributed to the opening of the Okinawa Trough [*Ho*, 1986], is a triangular, deltaic plain, bordered by the Hsüehshan Range to the northwest and the Eastern Central Range (ECR) to the southeast. The Eastern Central Range (ECR) is a pre-Tertiary metamorphic basement complex, representing the Asiatic continental crust and is the oldest lithotectonic unit of Taiwan [*Ho*, 1986]. It consists of high grade multi-deformed schists, gneisses and marble that have been exposed after deep burial [*Wu et al.*, 1997]. The ECR exposes the highest metamorphic grade rocks of Taiwan, and marks the eastern boundary of rocks with Eurasian Plate affinity [*Bertrand et al.*, 2012]. East of the ECR is the Longitudinal Valley (LV), a linear, narrow and fault-bounded valley that extends from Hualien (~24º N) to Taitung (~22.5º N) [*Ho*, 1986]. The valley is the widely accepted suture zone between the Eurasian and Philippine Sea plates in eastern Taiwan [*Biq*, 1971].

East of LV is the Coastal Range (CoR), an extension of the Luzon volcanic arc [*Ho*, 1986].

Taiwan provides an ideal natural laboratory to study the time-evolution of processes involved in arc-continent collision from beginning to end [*Bertrand et al.*, 2012]. To study these processes a multifaceted experiment known as TAIGER (Taiwan Integrated Geodynamics Research) was started in 2004. The TAIGER project collected lithospheric-scale seismic (land and marine) [*Huang et al.*, 2013; *Van Avendonk et al.*, 2014] and magnetotelluric [*Bertrand et al.*, 2009, 2012] data, along with structural and geochronology studies.

The land-based refraction and wide-angle reflection component of the TAIGER project deployed more than 2200 vertical-component seismographs (i.e. 4.5 Hz geophone and Ref Tek 125A "Texan" digitizers) along three E-W transects that traversed the key tectonic provinces of Taiwan, and three NE-SW profiles that paralleled the tectonic grain of Taiwan (Fig. 2.1). An important objective of the TAIGER project was to complete a seismic reflection line across Taiwan, however this line had to be cancelled for logistical reasons, leaving only seismic refraction and wide-angle reflection data available. While the marine component of TAIGER recorded wide-angle and multichannel seismic reflection data around the island [*Lester et al.*, 2012, 2013; *Eakin et al.*, 2014].

In this study we concentrate on the northern part of the island where the wide-angle reflection and local earthquake data show especially prominent reflection feature.

2.3 Seismic Texan Deployment

The TAIGER refraction and wide-angle reflection experiment employed a station spacing of ~200 m along the E-W transects that traversed the tectonic provinces of the island and a coarser ~ 3.0 km spacing for the three supplementary NE-SW profiles. Ten large (500 to 3000 kg) chemical charges were detonated for the recording of refractions and wide-angle (maximum offsets ~ 250 km) reflections. The T6 transect, comprised of 456 Texan seismographs, recorded continuously for 40 hours. During these 40 hours hundreds of local, and regional earthquakes were recorded in addition to the five explosive charges (N1 – N5) that were detonated along the line.

The seismic recordings of the five shot gathers examined in this study were filtered to remove the nonzero mean value (DC component) of the waveforms inherent in the Texan recorders. The records were then scaled with automatic gain control of 5 s applied to bring up weak signals such as reflections. Next, the direct P-wave was manually picked and a "top mute" was applied to remove any energy arriving before the first arrival, as this energy could not have been generated by explosive sources and is considered noise.

2.3.1 Shot N1

Shot N1 was located within the Coastal Plain east of Hsinchu city (Fig. 2.1). Inspection of the record for explosion N1 (Fig. 2.2a) shows high energy phases arriving after the direct arrival. These are most prominent for negative offsets (receiver 1-65), but are also present with lower amplitudes for some positive offsets (receivers 66-250). Fig. 2.2b shows the top 10 s of the record in Fig. 2.2a. The curved direct

arrival (light blue) suggests a diving wave caused by the high velocity gradient expected for a thick sequence of alluvial sediments. Following the direct arrival there are at least three visible high amplitude phases (marked in red, green, and yellow) that are multiple diving waves generated by steep velocity gradients in sediment layers of the Coastal Plain [*Huang et al.*, 2013].

The most significant feature of the recording for shot N1 is the relative absence of clear reflections. The absence of reflections could indicate a lack of penetration of seismic energy or geologic homogeneity at depth. Amplitude decay curves for the N1 recordings (Fig. 2.3) clearly shows source generated energy at amplitudes above background down to at least 15 s, well below the expected Moho depth. We therefore suggest that the lack of clear reflectivity is an indication of relative geologic homogeneity.

Moreover a Moho reflection is a feature missing from all shot gathers along transect T6. Although lack of energy penetration could be the cause, this is unlikely as amplitude decay curves (Figs 2.3 and 2.7b) show source generated energy at amplitudes above background down to at least 15 s, well below the expected Moho depth. We therefore suspect the Moho in northern Taiwan is mostly a gradational boundary, and not sharp boundary as in other regions such as southern Tibet [*Brown et al.*, 1996].

2.3.2 Shot N2

The record section for explosion N2 (Fig. 2.4) lacks the strong diving waves present in the recordings for shot N1. This is consistent with a higher degree of lithification expected for rocks in the Western Foothills and the Hsüehshan Range in which shot

N2 is located. Similarly, a lack of clear reflected energy in the recording of shot N2 supports a generally non-reflective character for the crust in northern Taiwan.

2.3.3 Shots N3 and N4

In contrast, the recordings for shots N3 and N4 (Fig. 2.5) exhibit an anomalously strong reflector at near offsets (i.e. beneath Datong Township). This feature underlies the Lishan fault near the southwest apex of the Ilan Plain (Fig. 2.1). The high amplitudes of this reflector are similar to those of reflection bright spots reported for the crust and upper mantle in many other areas [e.g. *Brown et al.,* 1979, 1996; *Smythe et al.,* 1982; *Hauser et al.,* 1987; *Jarchow et al.,* 1993; *Bannister et al.,* 2009]. Originally the term 'bright spot' was often used synonymously with hydrocarbon indicators [*Sheriff,* 1975], but the use of the term has expanded considerably. Nowadays any anomalously high amplitude reflection may be so labelled, and not surprisingly, bright spots occur in a variety of tectonic environments and are given diverse interpretations.

The first intrabasement bright spot reported from deep seismic reflection surveys was the Socorro bright spot beneath the Rio Grande rift in central New Mexico [*Brown et al.,* 1979]. The COCORP surveys identified an usually strong P-wave reflection dipping from 18 to 20 km depth where [*Sanford et al.,* 1973] had previously suggested the presence of magma based on anomalous shear wave reflected phases (S_zP, and S_zS) on microearthquake records. Additionally, high heat flow [*Reiter et al.,* 1979], nearby quaternary volcanism [*Chapin et al.,* 1980] and the active rift setting are consistent with the magma interpretation. Other examples of intrabasement bright spots within the Basin and Range province are the Death Valley

bright spot, interpreted as a lateral package of melt at a depth of 15 km [*de Voogd et al.*, 1986], and the Snake Range bright spots in eastern Nevada, a sequence of lateral reflectors between 15 and 20 km depth which *Hauser et al.*, [1987] suggests could be the result of magmatic intrusions. Other bright spots, such as the prominent reflections from the DEKORP program in Germany have been interpreted as related to non-magmatic fluids and porosity changes [*Lüschen et al.*, 1987, 1993].

The aforementioned bright spots are all located within the crust. However, bright spots are also present at greater depths. For example, the Buena Vista bright spot in northwestern Nevada, was interpreted as magmatic underplating beneath the Moho (depth ~ 30 km) on the basis of P_zS reflections [*Jarchow et al.*, 1993]. While *Stern et al.*, [2015] observed strong reflections from the base of the lithosphere (depth ~ 100 km) beneath North Island, New Zealand.

The Datong bright spot appears as a continuous multi-cyclic reflector at near-vertical incidence on both records (Fig. 2.5). It lies at 6.1 s two-way time (twt) and spans at least 13 km along the seismic profile. Furthermore it exhibits little or no dip and no observable offset that could be related to a vertically oriented fault. Time to depth conversion using the velocity model of *Kuo-Chen et al.*, [2012] places the reflector at a depth of approximately 17.4 km near the southwest apex of the Ilan Plain (Fig. 2.6).

A local occurrence of anomalously high amplitude is generally the defining parameter for bright spots [*Sheriff*, 1975], and in the case of the Datong anomaly relative amplitude values are approximately 17 dB above background energy on unstacked records (Fig. 2.7). This value is comparable to that of other reported bright

spots, particularly those interpreted as magma, for example, 8.5 dB for the Socorro bright spot [*Brown et al.*, 1979], 10 dB for the Snake Range bright spots [*Hauser et al.*, 1987], 17 dB for the Buena Vista bright spot [*Jarchow et al.*, 1993], and 22 dB for the southern Tibet bright spots [*Brown et al.*, 1996]. The seismic display in Fig. 2.7 also indicates a possible reflection (Pr) beneath the DBS at about 8.5 s twt. The reflection interpretation is based on the flattening of the arrival after the NMO correction was applied to the record, making it unlikely that this arrival is a multiple. Time to depth conversion places the Pr reflector at approximately 24 km, or about 6.6km beneath the DBS. This reflector might be an unrelated feature, or possibly the bottom of the unit causing the DBS; neither possibility can be ruled out.

Before attributing the Datong bright spot to an unusual lithologic contrast at depth, other factors that affect reflection amplitudes must be considered and/or corrected. Although geometrical focusing is known to produce local reflection amplitude anomalies there is no evidence of reflector curvature for the Datong event. Interference or tuning due to thin layers with thickness on the order of the dominant wavelength can increase the amplitudes of reflection up to a maximum factor of 2 [*Kallweit and Wood*, 1982]. The presence of signal amplification by tuning can sometimes be inferred from the occurrence of resonant frequencies in the amplitude spectra of a signal [*Brocher*, 1981]. Fourier analysis of the record for shot N4 containing the DBS (Fig. 2.8) reveals that the spectral component of the source is relatively broadband in character (0 – 40 Hz) with maximum amplitudes at around 5 Hz. The spectrum returned by the DBS was also broadband in character (2 – 23 Hz),

albeit with significantly larger amplitudes present between 6 and 11 Hz. This spectrum suggested tuning may be a factor, but not dominate.

While *Pratt et al.*, [1991] and *Brown et al.*, [1996] were able to discriminate the polarity of the Surrency and Tibetan bright spots, respectively, similar approaches were not definitive when applied to the DBS records as the multi-cyclic character of the reflectors makes it impossible to pick an onset. Furthermore, estimation of the impedance contrast between the Datong reflector and the surroundings were unsuccessful because there were no reflections recorded from known lithologic contrasts that could be used to calibrate it against.

2.4 Local Earthquakes

During the 40 hours that the Texans recorded continuously 318 local and regional earthquakes were registered. These events were located by *Kuo-Chen et al.*, [2012]. We examined the records of these events and selected those with nearby epicenters to the Texan receiver line to further inspect for possible reflected and converted phases off the Datong bright spot. We found three events with high signal-to-noise near the receiver line. One of these events exhibited a clear seismic arrival following the direct P-wave that did not correspond to the direct S-wave (Figure 10). The seismic record (i.e. earthquake-gather) for the event is shown in Fig. 2.10. The event shows a clear direct P-wave (Pd) and unidentified arrival just below the P-wave (Fig. 2.10a). To investigate if this unidentified arrival corresponds to a reflection off the DBS we generated a synthetic earthquake-gather using the Omni (® Schlumberger) software package. The synthetic record was created using the Texan receiver geometry, the event's hypocenter, and a simple three-dimensional two-layer

structural model. The 3D model consisted of a surface layer and a reflecting flat layered at a depth of 17 km to mimic the DBS reflector. The surface layered was generated using a digital elevation model of northern Taiwan. The surface layer had a constant P- and S-wave velocity of 5.3 and 3.0 km s^{-1}. These velocities correspond to the average root-mean-squared P- and S-wave velocities for the region covered in the map section (Fig. 2.9) to a depth of 17 km [*Kuo-Chen et al.*, 2012]. The synthetic earthquake-gather (Fig. 2.10b) shows the direct P arrival (Pd), the expected reflected arrival from the model interface at depth, and the direct S-wave (Sd). Inspection of Figs 2.10a and 2.10b suggests that the unidentified arrival observed on the real earthquake-gather likely corresponds to a reflection generated by a feature that exhibits little or no-dip. In Figs 2.10c and 2.10d we have displayed offset gathers of the real and synthetic event, respectively for the receivers west of the epicenter (i.e. negative offsets). The unidentified arrival (Fig. 2.10c) shows the clear hyperbolic moveout characteristic of reflections. Based on the character of the arrival on the real earthquake-gathers, and its arrival time (Figs 2.10a and 2.10c) we suggest that this phase corresponds to a reflection from a structure located at a depth of approximately 17 km. The reflection points location place the structure approximately 11.5 km SE from the DBS and at a similar depth (17 km).

2.5 Discussion

The seismic refraction and wide-angle reflection data collected during project TAIGER has as its more prominent feature the Datong bright spot (Fig. 2.3), an anomalously high reflector located near the SW apex of the Ilan Plain (Fig. 2.6) at a depth of about 17 km. Other important features observed in the TAIGER recordings

are the reflector (Pr) underlining the DBS at a depth of approximately 24 km, a reflected phase present in an earthquake record generated at a depth of about 17 km, and the lack of Moho reflections across the profiles.

The nature of the reflectors observed could likely be attributed to fluids, a crystallized intrusion, or to variations in physical properties of the medium (i.e. velocity and/or density). A 2-D resistivity model of long-period magnetotelluric (MT) data collected as part of project TAIGER [*Bertrand et al.*, 2012] does not show any particular anomaly at the location of the DBS. Instead the results by *Bertrand et al.*, [2012] show a resistive feature (i.e. resistivity ~ 100 – 1000 Ω m) that extends to 20 km beneath the surface trace of the Lishan Fault. The absence of a low resistivity feature corresponding to the DBS suggests that it probably results from a seismic impedance contrast from a solid-solid interface rather than a contrast involving fluids. Because of the large range and overlaps in resistivity for different lower crustal rocks [*Haak and Hutton*, 1986] it is not possible to differentiate between potential lithological contrasts that could give rise to the observed reflectivity based on resistivity values alone. However, the occurrence of arc, and back-arc volcanism [*Kizaki*, 1986; *Sibuet et al.*, 1998], of diking and extensional tectonics [*Tong et al.*, 2008; *Hou et al.*, 2009; *Lai et al.*, 2009; *Konstantinou et al.*, 2013; *Kang et al.*, 2015] suggest that the area in which the DBS is located could accommodate a frozen magmatic intrusion without the need of invoking the presence of fluids at 18 – 25 km depth.

The DBS is a multi-cyclic feature underlined by the reflector (Pr) at about 8.5 s twt (Fig. 2.7). The relation between the DBS and Pr is difficult to ascertain, however

we suggest that either (1) the Pr event represents the bottom of the feature generating the DBS, or (2) the two are separate, but perhaps related, features. If the former is true, the thickness of the feature generating both reflectors depends on its interval velocity, if the velocity of the feature is similar to the surrounding rock the time to depth conversion applied in section 2.3 will yield a reliable thickness estimate of approximately 6.6 km. The issue with this scenario is that the large amplitude of the DBS must then be explained by density differences, alone, which is unrealistic. Thus we need constraints on the interval velocity of the feature. It could be argued that simply using the Dix equation [*Dix*, 1955] will result in the interval velocity of the structure generating the DBS. However, the resolution of the velocity model (4 km x 4 km x 2 km) by *Kuo-Chen et al.*, [2012] could be on the same order of magnitude as the feature generating the DBS, if this is the case, there could be averaging of the velocity of the DBS with that of the surrounding material, resulting in an inaccurate interval velocity for the DBS.

The average interval velocity for the region encompassing the DBS (Fig. 2.6) between the depths of 18 – 24 km is approximately 5.75 km s^{-1} [*Kuo-Chen et al.*, 2012], while a density of 2700 kg m^{-3}, comparable to that of slate at 20 km [*Christensen and Mooney*, 1995], is used to estimate the seismic impedance of the country rock. By using a range of velocities and densities for rocks at approximately 20 km depth we can estimate the thickness of the feature generating the DBS. Values for compositions ranging from basalt (ρ = 2894 kg m^{-3}, v = 5.918 km s^{-1}) to pyroxenite (ρ = 3280 kg m^{-3}, v = 7.862 km s^{-1}) given by *Christensen and Mooney*, [1995] are used to estimate thickness and reflection coefficient. Using those velocity values we obtain

a thickness estimate that ranges from 7.1 to 8.1 km. While the reflection coefficient estimate ranges from 0.04 to 0.24. As the relative amplitude of the DBS is considerably larger than the background reflectivity (Fig. 2.7), is reasonable to expect a high reflection coefficient ($c > 0.1$). Under the assumption that the reflector results from a solid-solid interface we suggest that a mafic to ultramafic frozen intrusion could be the source of the DBS.

The other scenario we must consider is that the DBS and the Pr reflector are separate features. The earthquake-gather (Fig. 2.9) shows no trace of a deeper reflection that would correspond to that observed at 8.5 s in Fig. 2.7, which suggests that the Pr arrival is a localized feature and likely independent of the DBS. As an independent feature the DBS would have to be considerably thinner than the above estimates, but identifying a distinct reflection from its base to determine its thickness was not possible. As *Jarchow et al.*, [1993] argued for the Buena Vista bright spot, there are two explanations for not finding a reflection from the base of the DBS (1) the feature generating the DBS is too thin for the base to be resolved as a separate reflection, or (2) the base is gradational and consequently nonreflective. If the feature is too thin the vertical dimension of the feature generating the DBS can be constrained using the dominant wavelength at a depth of 17 km (i.e. 540 m). Assuming a threshold of $\lambda/4$ [*Yilmaz*, 2001] the DBS should be 135 m thick or less so that its base reflection is indistinguishable from the top reflection. If there is a gradational change in seismic impedance that causes a nonreflective lower boundary for the DBS, seismic data alone will not suffice to constraint the thickness of the feature.

An important feature recorded during the Texan deployment is the reflected arrival shown in the earthquake-gather of Fig. 2.10. The depth of the feature generating this arrival is less constrained than the depth of the DBS as a result of the uncertainty in the event's hypocenter. However, our modeling suggests that the arrival is generated at a depth of about 17 km, very similar to that of the Datong bright spot. Inspection of the reflection point locations for the DBS and the reflection observed in the earthquake-gather (Fig. 2.9) shows that they are separated by a distance of ~11.5 km. However, the possibility that these features are connected outside the vertical plane of the survey cannot be ruled out. In any case, given their relative proximity and depth similarity we suggest that we are likely observing at least the same type of feature being illuminated at different locations.

The Datong bright spot is located in northeastern Taiwan, in a region experiencing the transition between collision and back-arc extension (Fig. 2.11), facilitated by the effect of the suction force related to the retreat of the Ryukyu trench [*Hou et al.*, 2009]. The bright spot is adjacent to the Chingshui geothermal field and to the SW apex of Ilan Plain (Fig. 2.11), considered by many as the on-land extension of the Okinawa Trough [*Teng*, 1990; *Liu*, 1995]. The plain is known to be experiencing horizontal displacements between 1.9 – 43.0 mm yr^{-1} in a direction between 38 – 143° relative to the stable continental margin (Fig. 2.9), resulting in remarkable extensional strain rates (e.g. 2.66 μstrain yr^{-1}) in its SW and SE apexes [*Hou et al.*, 2009]. Seismic reflection profiles identified a series of faults buried below the alluvial deposits of the Ilan Plain reaching down to basement depths [*Jhiang*, 1976], with *Tong et al.*, [2008] associating the locations of some of these faults to diking events in the top 10 km

under the Ilan plain based on geomagnetic data. Recent studies reveal active seismogenic structures responsible for shallow seismicity beneath and offshore the Ilan Plain [*Ku et al.*, 2009; *Lai et al.*, 2009; *Konstantinou et al.*, 2013]. *Lai et al.*, [2009] and *Konstantinou et al.*, [2013] present evidence of tensile faulting in the focal mechanisms of shallow (i.e. depth < 15 km) local events, with dyke intrusion under and offshore the plain as the likely source of some of these events. Furthermore, fluid samples from the plain and the nearby Kueishantao Holocene volcanic islet (i.e. 53 km from the DBS) exhibit significant excess of ^{3}He, indicating that the mantle component plays an important role for their gas sources [*Yang et al.*, 2005].

The Choshui Fault (Fig. 2.11) originally imaged by *Jhiang*, [1976] and later traced from a geomagnetic survey [*Tong et al.*, 2008] links with the Lishan Fault (Fig. 2.9) and possibly represents the extension of the Lishan Fault under the Ilan Plain. The Lishan Fault separates two major tectonostratigraphic units of Taiwan [*Ho*, 1986], the Hsüehshan Range and the Backbone Range, which differ in lithology, ages of sediments, metamorphic grades and deformation styles [*Lee et al.*, 1997]. The fault has experience N-S extension during the last 2 Ma at its northern segment, near the Ilan Plain. As the DBS lies beneath the surface trace of the LF is natural to ask what the relation is between these two features. Unfortunately, the relation between the DBS and the LF is ambiguous, mostly because the nature of the fault at depth is unknown. If we assume the LF to be a near-vertical fault, the DBS's lack of apparent vertical offset suggests that either the fault does not reach down to the depth of the bright spot (i.e. ~ 18 km) or that the bright spot was emplaced after the last significant movement along the LF.

Although the fluid or "frozen" nature of the bright spot still needs further study, the tensile faulting solutions under the Ilan Plain, the large extensional rates of the region, nearby active volcanism and geothermal activity, and the likely mantle interaction of surface fluids all are consistent with the interpretation of the DBS as an intrusion, most likely related to the ongoing extension of northeastern Taiwan.

2.6 Conclusions

The controlled source on-land seismic experiment of project TAIGER included the recording of 5 dynamite explosions along transect T6 across northern Taiwan. These recordings are largely lacking in any clear reflections from the crust, with notable exception of a pronounced reflector near the SW apex of the Ilan Plain. This anomalous reflector extends at least 13 km along the seismic profile and lies at a depth of 17.4 km beneath the surface trace of the Lishan Fault. The occurrence of this feature within extending crust and its similarity to bright spots in other tensional settings suggest that the Datong Bright spot marks magma at depth. However, magnetotelluric measurements indicate no corresponding conductivity anomaly, indicating that if molten this feature may be too small to be detected by such measurements. Alternatively, the strong reflectivity could be indicative of a mafic sill emplace in more granitic crust (Fig. 2.12). A bright reflector is also indicated by one of the nearby earthquake recordings collected during the seismic experiment. Modeling suggests that this reflector lies at a similar depth (~ 17 km) as the Datong bright spot, albeit about 11.5 km further east. We suggests that this reflection and the bright spot form the same, or a closely related, feature. A more localized reflector was imaged below the Datong bright spot (Fig. 2.7) at a depth of 24 km. It is our

interpretation that this reflector (Pr) is not the base of the DBS, but a distinct reflector that may be a related intrusion.

2.7 Figures

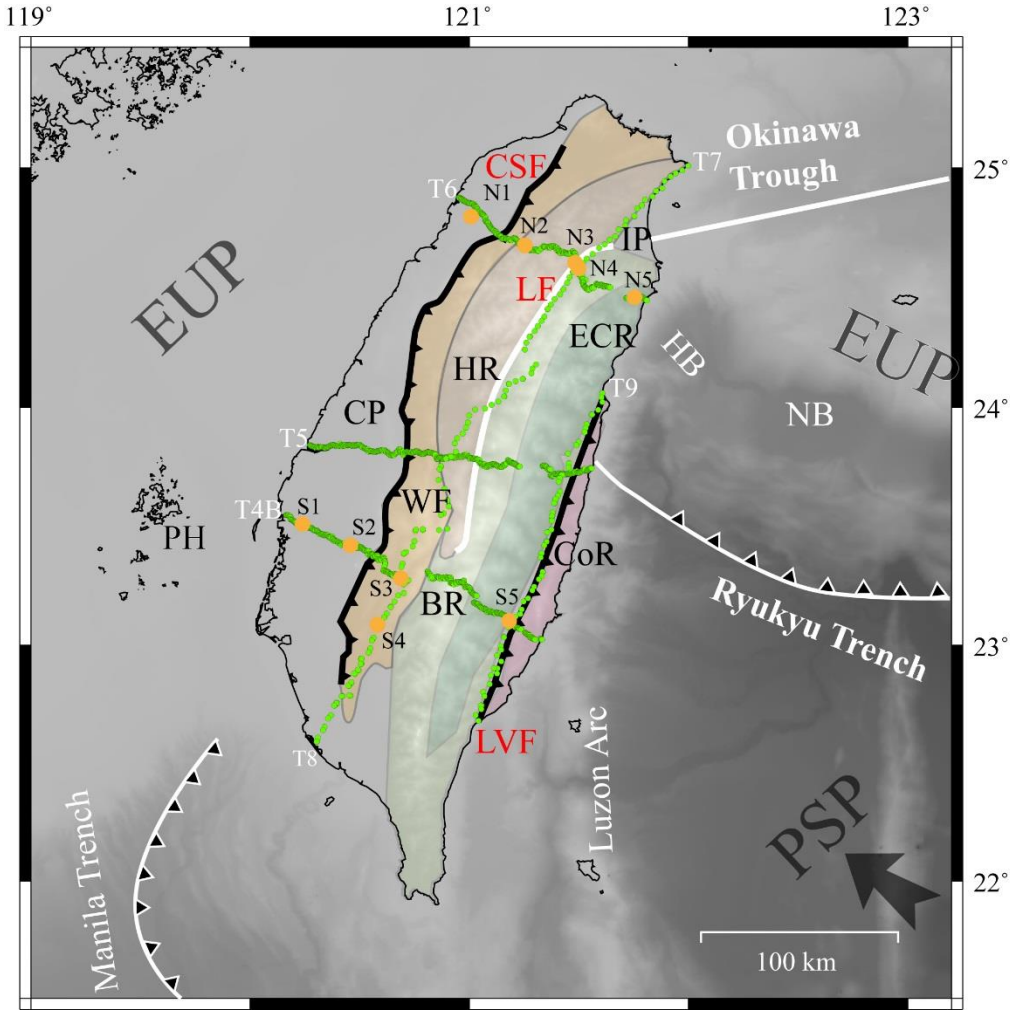

Figure 2.1: Geologic and tectonic map of Taiwan with the locations of the TAIGER seismic lines. Main geological provinces are abbreviated as follows: Penghu Islands (PH), Coastal Plain (CP), Western Foothills (WF), Hsüehshan Range (HR), Backbone Range (BR), Eastern Central Range (ECR), Ilan Plain (IP), Coastal Range (CoR). Major faults are abbreviated as follows: Chelungpu and Shuangtung Faults (CSF), Lishan Fault (LF), and Longitudinal Valley Fault (LVF). The location of Texan recorders (green dots) and chemical charges (orange dots) are shown. Large gray arrow indicates PSP motion.

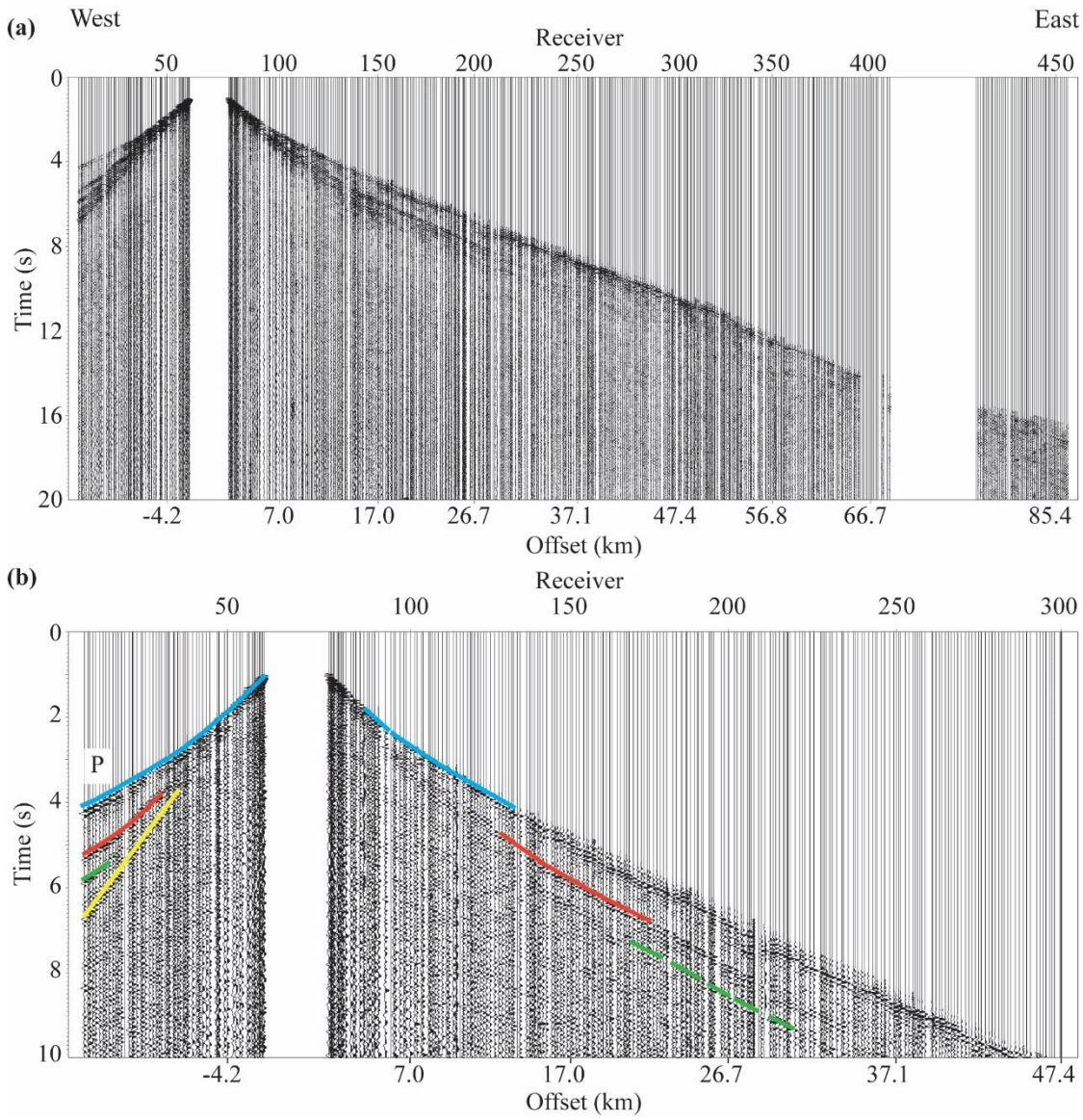

Figure 2.2: (a) Controlled source shot-gather N1 recorded along transect T6. (b) Top 10 s of data. Colored lines mark arrivals corresponding to multiple diving P waves traveling along the sedimentary section of the Coastal Plain, similarly to those observed by [*Huang et al.*, 2013] in the Texan data of southern Taiwan across transect T4B.

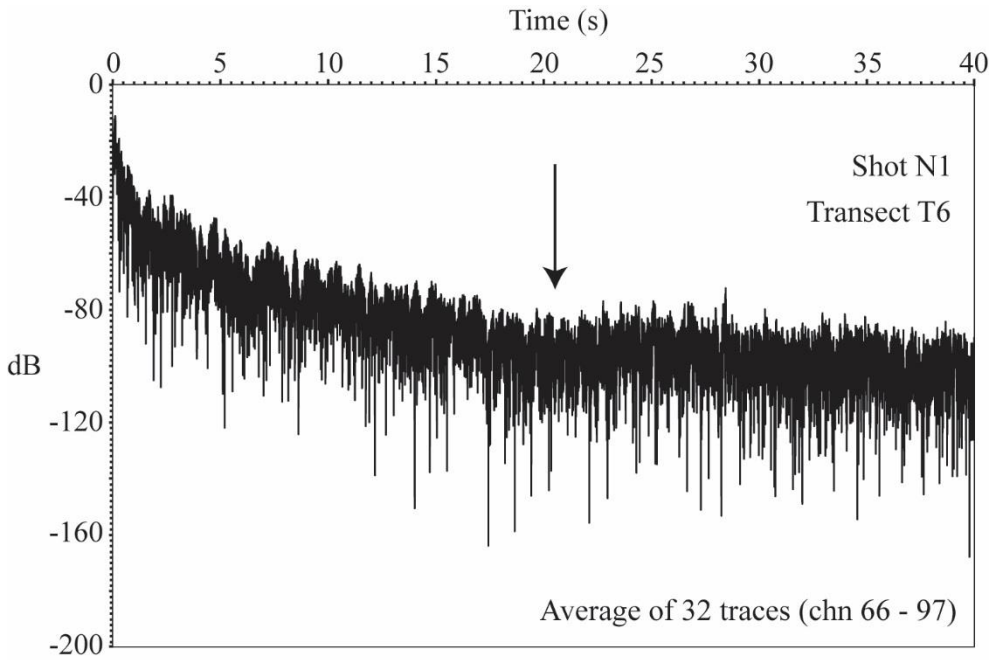

Figure 2.3: Average amplitude decay curve for 32 near-vertical traces (i.e. channel 66 – 97) of shot N1. Arrow indicates where source generated energy is indistinguishable from background energy.

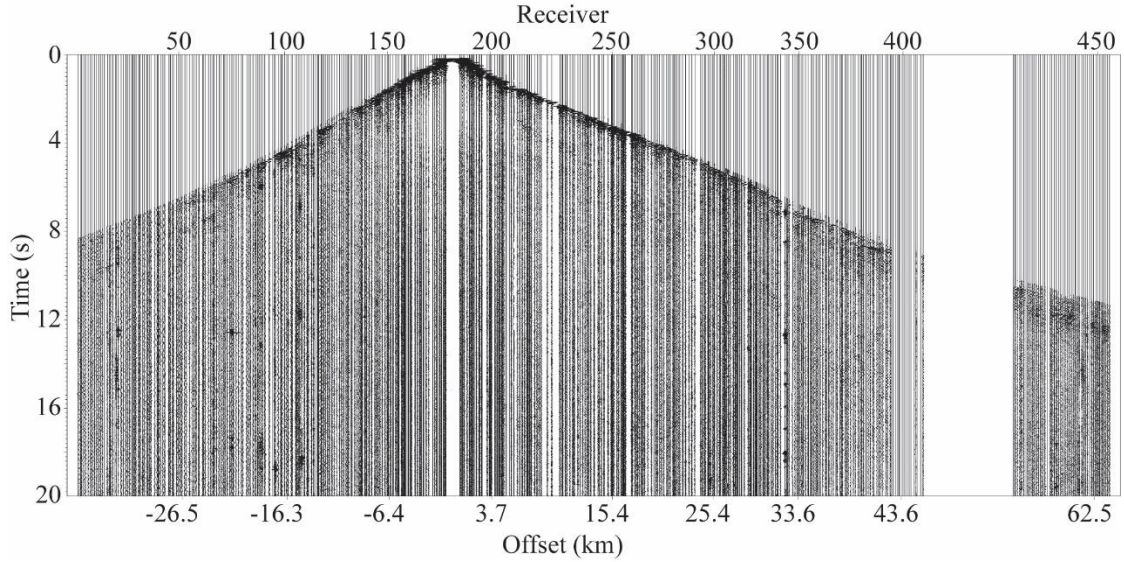

Figure 2.4: Controlled source shot-gather for shot N2.

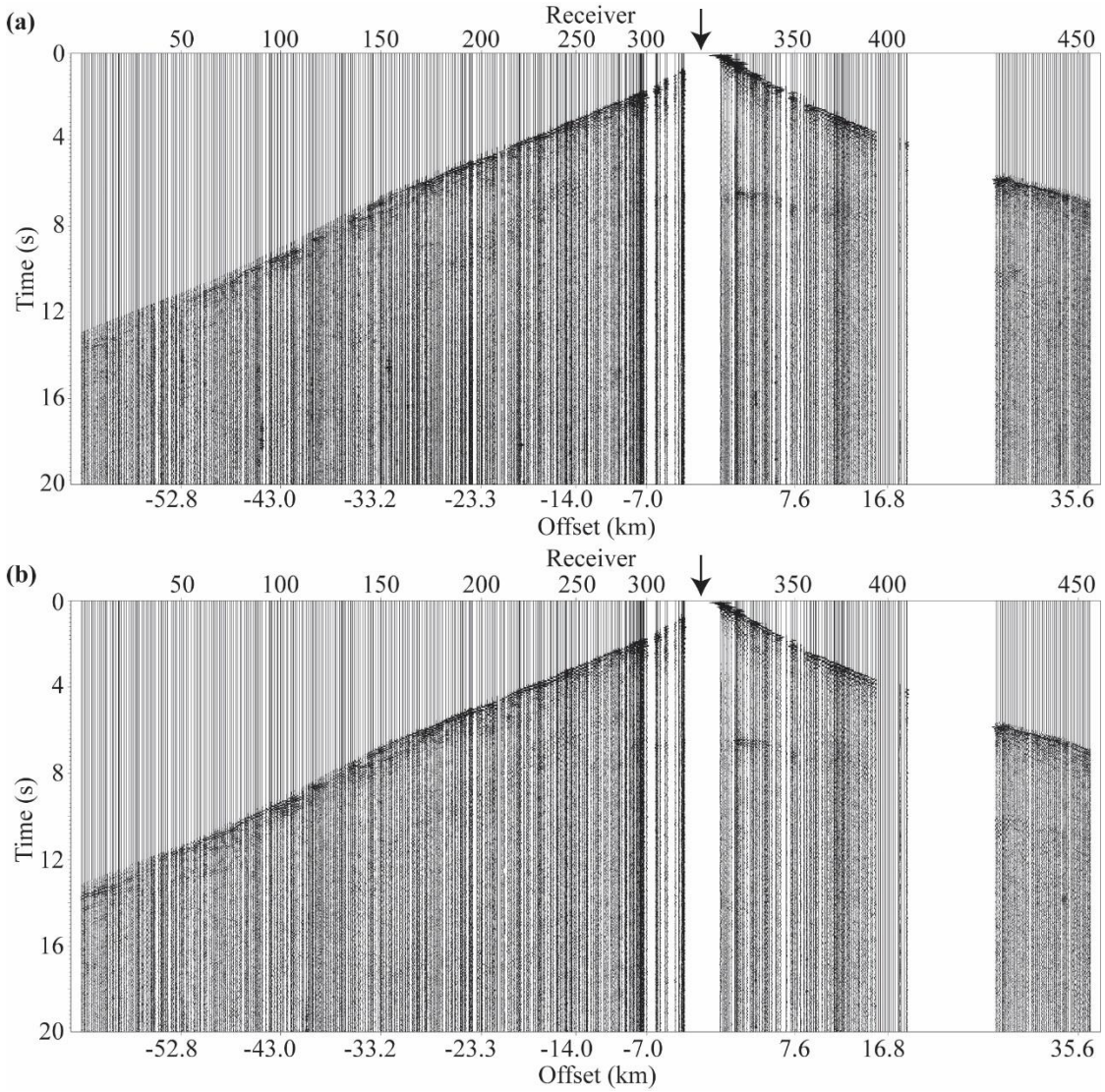

Figure 2.5: Controlled source shot gathers recorded along transect T6 for (a) shot N3 and (b) shot N4. Black arrow indicates the location of the Lishan Fault (Fig. 2.1) and shots N3 and N4 relative to the receivers.

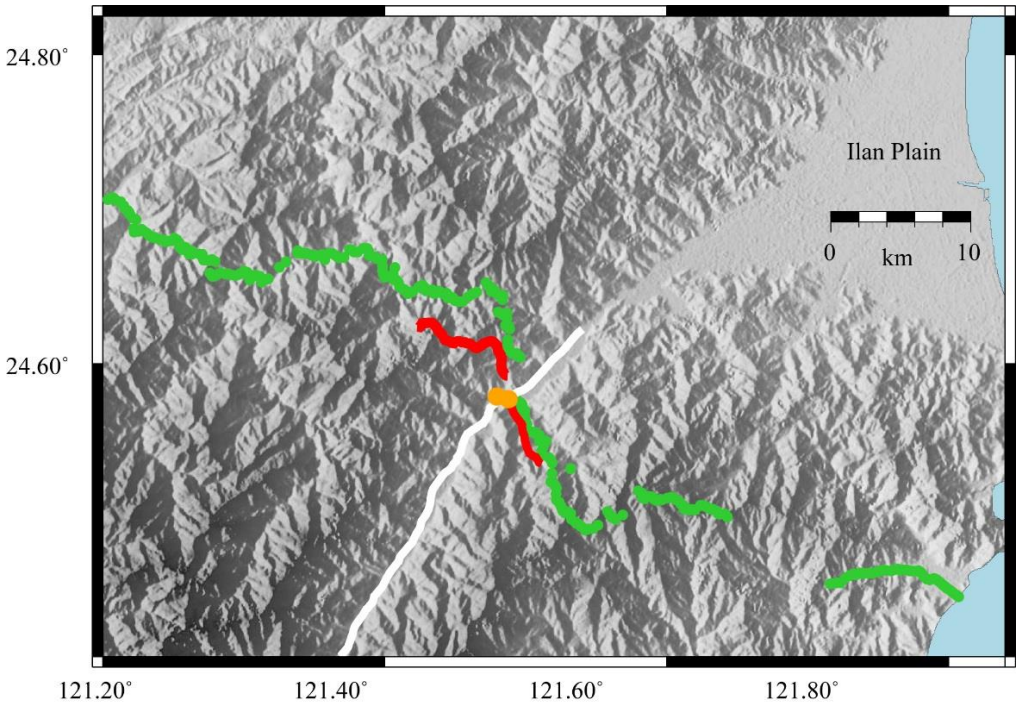

Figure 2.6: Northeastern Taiwan with the location of the seisimic stations (green dots) and the explosions N3 and N4 (orange dots). The Lishan Fault is indicated by a thick white line, while the extent of the DBS is shown with the thick red lines.

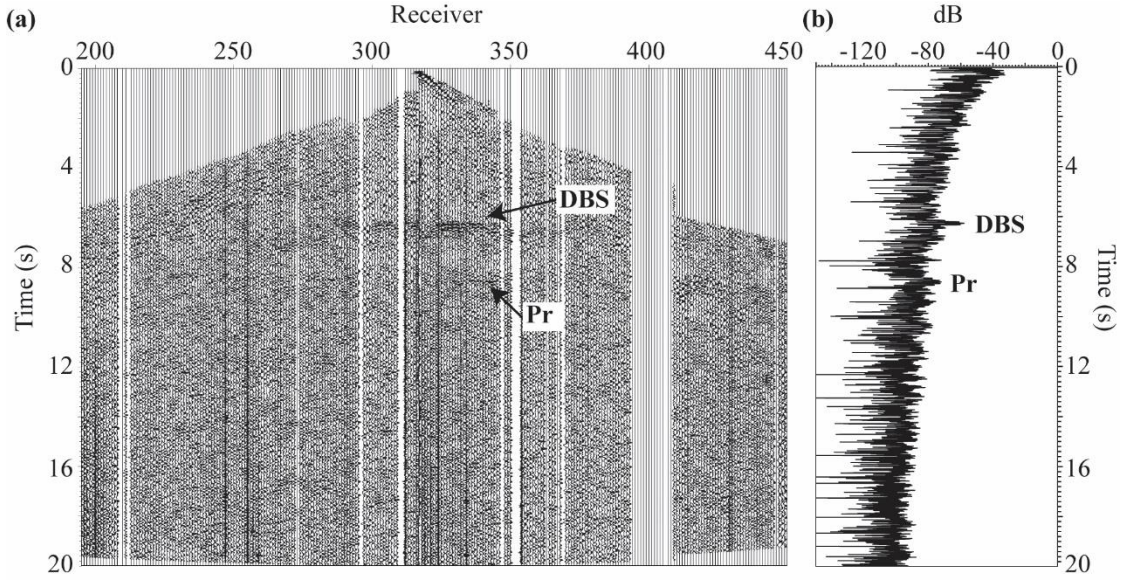

Figure 2.7: (a) Record of shot gather N4 after elevation statics, and NMO correction. The figure shows the DBS and another arrival (Pr). The second arrival is interpreted as a reflection based on its flattening after the NMO correction. (b) Average amplitude decay curve of 50 traces containing the Datong Bright Spot (DBS). The DBS relative amplitude values are approximately 17 dB above background energy, while the Pr relative amplitude values are about 8 dB above background energy.

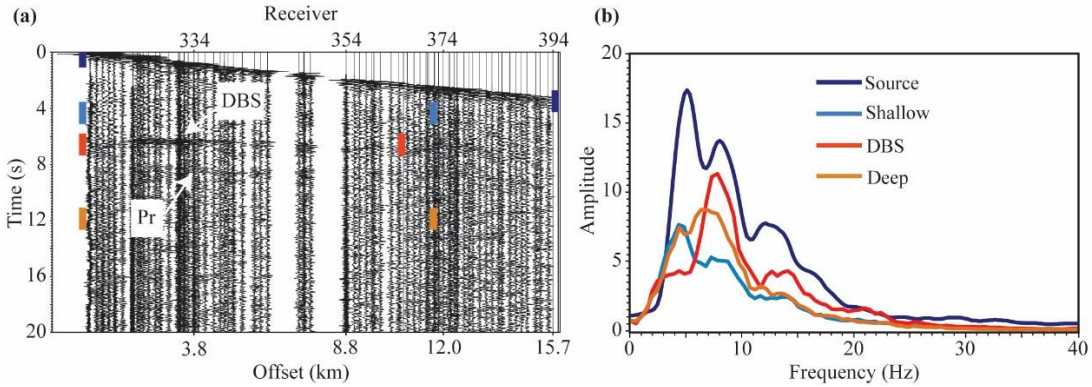

Figure 2.8. (a) Record of shot gather N4 showing positive offsets after NMO correction. Horizontal bars of the same color represent a window, the height of the bars represent the window length. Traces within bars of the same color were used to calculate and average amplitude spectra for the window. A possible second reflection is visible at ~8.4 s twt between 2.5 – 4.5 km offsets. (b) Shows different amplitude spectra calculated for the windows in (a).

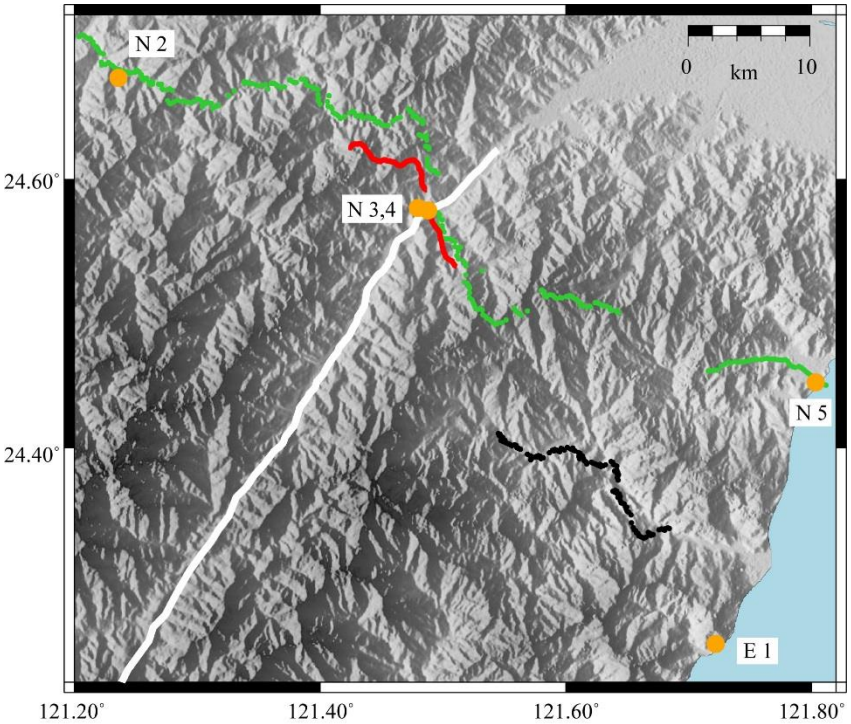

Figure 2.9: Northeastern Taiwan with the location of the seismic stations (green dots) and the epicenter E1 (yellow dot) of the earthquake discussed in the text. Also shown are the locations of 4 dynamite shots (yellow dots). The Lishan Fault is indicated by a thick white line, while the observed extent of the DBS is shown with the thick red lines. The back dots represent the location of the reflection points for the earthquake (E1) illuminating a horizontal reflector at 17 km depth.

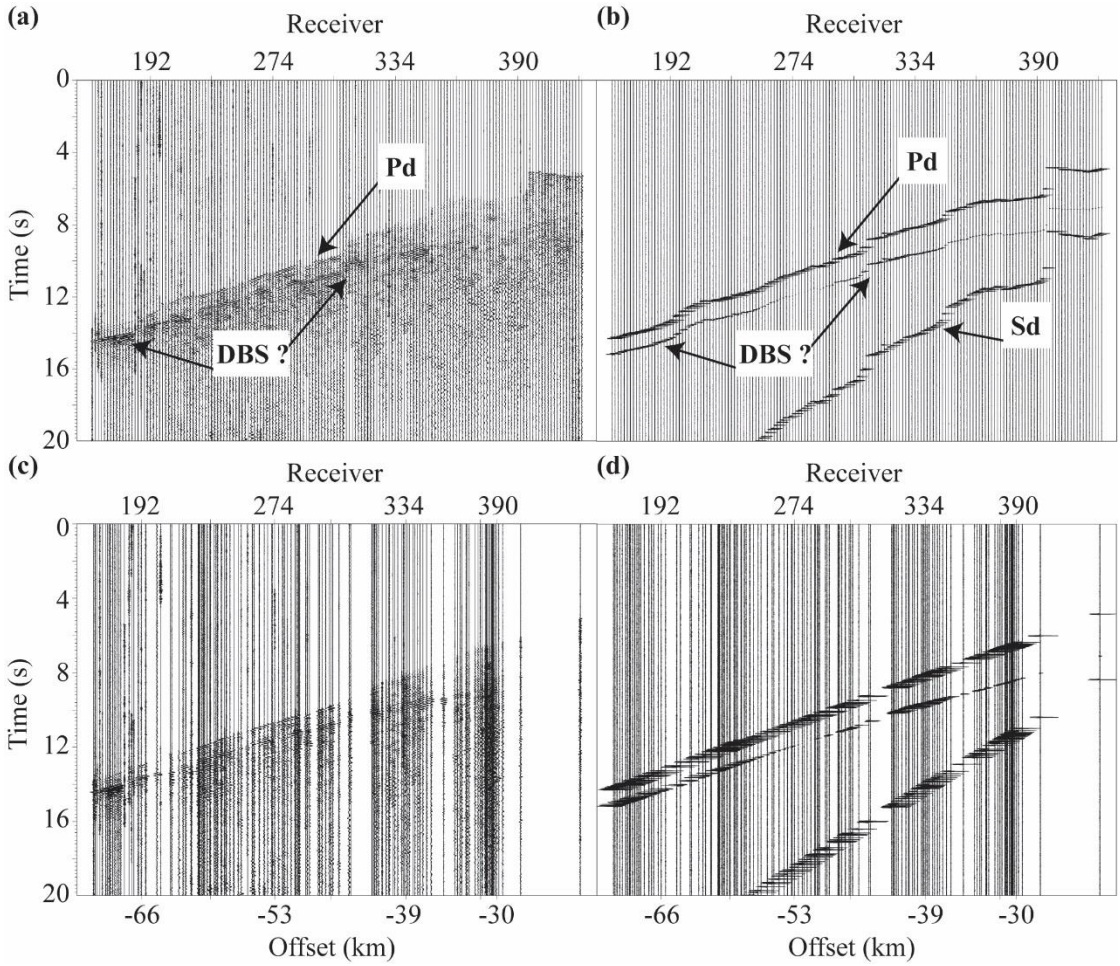

Figure 2.10: Event recorded during the TAIGER Texan deployment. (a) Earthquake-gather showing two clear wide angle arrivals, labeled Pd (direct arrival) and Pr a later arrival. (b) Synthetic earthquake-gather generated using a simple 2 layer model, the TAIGER receiver geometry, and the event hypocenter. The top layer of the model corresponds to the topography of northern Taiwan. This layer has constant P- and S-wave velocities of 5000 and 2890 ms^{-1}, respectively. The second layer is flat reflector that spans the island at a depth of 17 km. (c) Earthquake-gather displayed by distance from the source (i.e. offset) and showing only stations located west of the epicenter. (d) Synthetic earthquake-gather plotted with the same parameters as (c). The similarity between the synthetic and the observed earthquake gather suggest at Pr is a reflection from approximately 17 km depth.

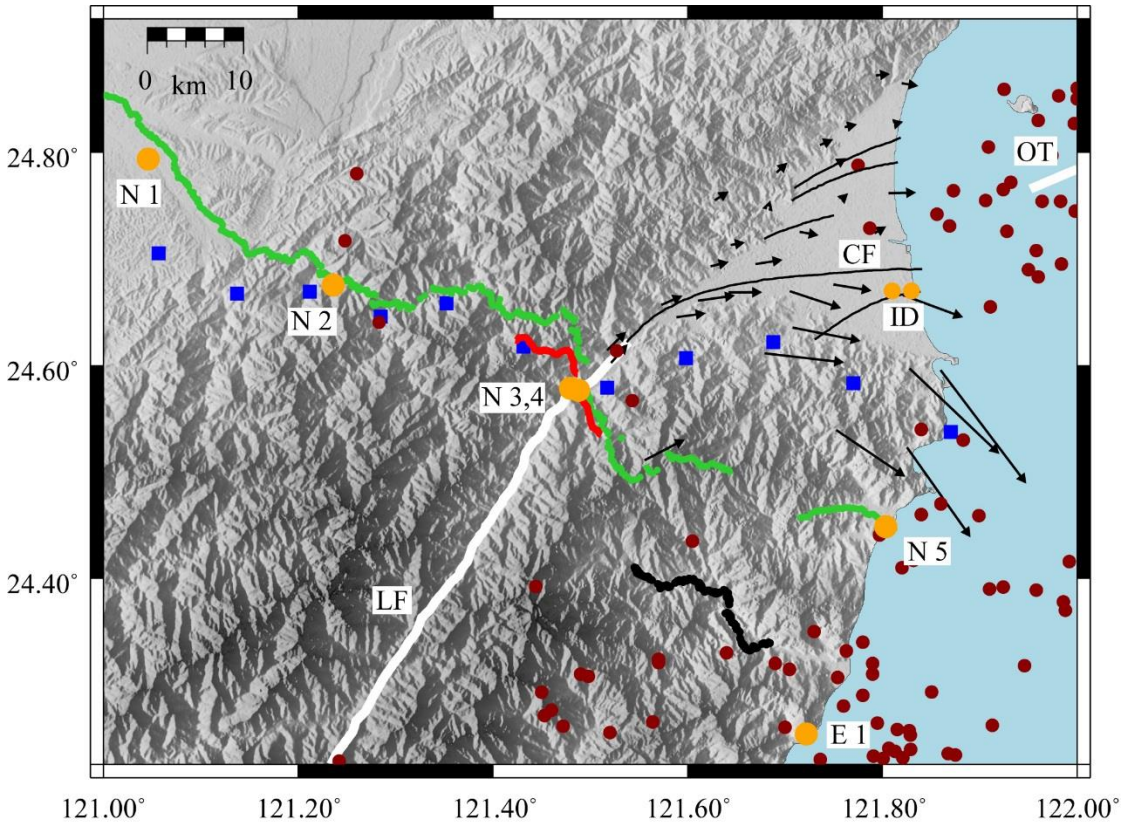

Figure 2.11: Northeastern Taiwan with the location of the seismic stations (green dots) and the explosions (N1 – N5). The Lishan Fault (LF) and the Okinawa Trough (OT) are indicated by thick white lines. Location of earthquake (E1) shown in Fig. 2.10. Location of a magnitude ML 5.9 earthquake doublet (ID: Ilan Doublet) linked to dyke intrusions under the Ilan Plain [*Lai et al.*, 2009]. Seismicity shallower than 30 km between 2005 and 2016 (red dots). Horizontal displacements around the Ilan Plain are shown by black arrows [*Hou et al.*, 2009]. Basement faults within the Ilan Plain are numbered 1 through 5. The Choshui Fault (CF), fault 4 is suspected to be an extension of the Lishan Fault [*Jhiang*, 1976]. Magnetotelluric stations are shown as blue squares [*Bertrand et al.*, 2012].

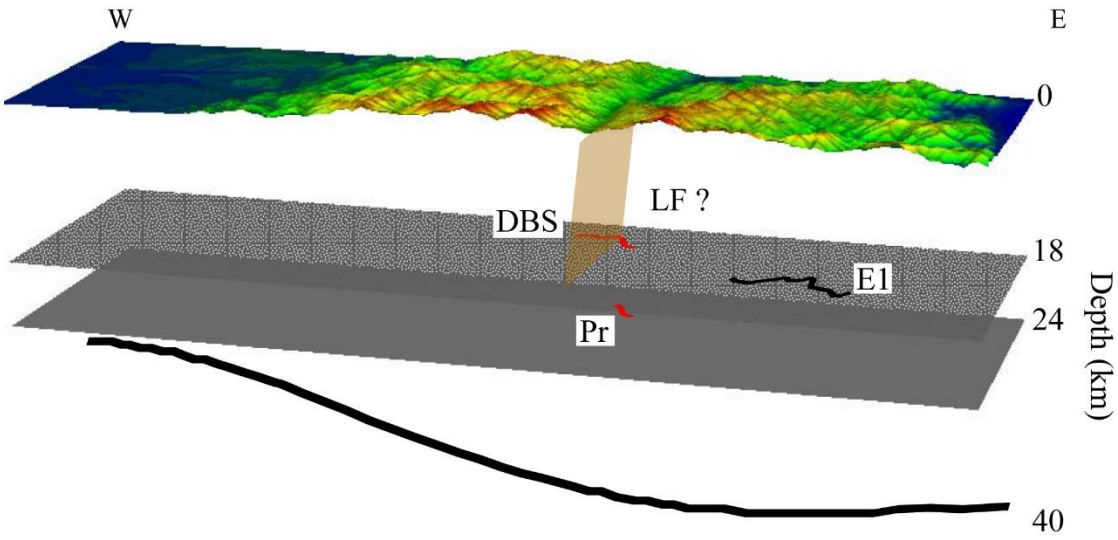

Figure 2.12: Simplified model of the section of northeastern Taiwan investigated by transect T6 (see Fig. 2.1). The length of this 3D cross-section is approximately 100 km. The DBS, Pr, and reflector in the earthquake gather are shown on top of constant depth surfaces. The black curve line indicates Moho depth variation across the profile [*Van Avendonk et al.*, 2016].

REFERENCES

Bannister, S., F. Davey, and D. Woodward (2009), A lower crustal "bright spot" under the Bay of Plenty, North Island, New Zealand, *Tectonophysics*, *472*(1–4), 62–71, doi:10.1016/j.tecto.2008.09.044.

Bertrand, E., M. Unsworth, C.-W. Chiang, C.-S. Chen, C.-C. Chen, F. Wu, E. Türkoğlu, H.-L. Hsu, and G. Hill (2009), Magnetotelluric evidence for thick-skinned tectonics in central Taiwan, *Geology*, *37*(8), 711–714, doi:10.1130/G25755A.1.

Bertrand, E. A., M. J. Unsworth, C.-W. Chiang, C.-S. Chen, C.-C. Chen, F. T. Wu, E. Türkoğlu, H.-L. Hsu, and G. J. Hill (2012), Magnetotelluric imaging beneath the Taiwan orogen: An arc-continent collision, *J. Geophys. Res. Solid Earth 1978–2012*, *117*(B1).

Biq, C.-C. (1971), Some aspects of post-orogenic block tectonics in Taiwan. Recent crustal movements, *Bull R Soc NZ*, *9*, 19–24.

Brocher, T. M. (1981), Geometry and physical properties of the Socorro, New Mexico, magma bodies, *J. Geophys. Res.*, *86*(B10), PAGES 9420–9432.

Brown, L. D., P. A. Krumhansl, C. E. Chapin, A. R. Sanford, F. A. Cook, S. Kaufman, J. E. Oliver, and F. S. Schilt (1979), COCORP seismic reflection studies of the Rio Grande rift, *Rio Gd. Rift Tecton. Magmat.*, 169–184.

Brown, L. D., W. Zhao, K. D. Nelson, M. Hauck, D. Alsdorf, A. Ross, M. Cogan, M. Clark, X. Liu, and J. Che (1996), Bright spots, structure, and magmatism in southern Tibet from INDEPTH seismic reflection profiling, *Science*, *274*(5293), 1688.

Chapin, C. E., A. R. Sanford, and L. D. Brown (1980), Past and present magmatic and hydrothermal systems at Socorro, New Mexico, *Eos Trans AGU*.

Christensen, N. I., and W. D. Mooney (1995), Seismic velocity structure and composition of the continental crust: A global view, *J. Geophys. Res. Solid Earth*, *100*(B6), 9761–9788.

Dix, C. H. (1955), Seismic velocities from surface measurements, *Geophysics*, *20*(1), 68–86.

Eakin, D. H., K. D. McIntosh, H. J. A. Van Avendonk, L. Lavier, R. Lester, C.-S. Liu, and C.-S. Lee (2014), Crustal-scale seismic profiles across the Manila subduction zone: The transition from intraoceanic subduction to incipient collision, *J. Geophys. Res. Solid Earth*, *119*(1), 2013JB010395, doi:10.1002/2013JB010395.

Gourley, J. R., T. Byrne, Y.-C. Chan, F. Wu, and R.-J. Rau (2007), Fault geometries illuminated from seismicity in central Taiwan: implications for crustal scale structural boundaries in the northern Central Range, *Tectonophysics*, *445*(3), 168–185.

Haak, V., and R. Hutton (1986), Electrical resistivity in continental lower crust, *Geol. Soc. Lond. Spec. Publ.*, *24*(1), 35.

Hauser, E., C. Potter, T. Hauge, S. Burgess, S. Burtch, J. Mutschler, R. Allmendinger, L. Brown, S. Kaufman, and J. Oliver (1987), Crustal structure of eastern Nevada from COCORP deep seismic reflection data, *Geol. Soc. Am. Bull.*, *99*(6), 833–844, doi:10.1130/0016-7606(1987)99<833:CSOENF>2.0.CO;2.

Hickman, J. B., D. V. Wiltschko, J. H. Hung, P. Fang, and Y. Bock (2002), Structure and evolution of the active fold-and-thrust belt of southwestern Taiwan from Global Positioning System analysis, *Geol. Geophys. Arc-Cont. Collis. Taiwan*, 75–92.

Ho, C. S. (1986), A synthesis of the geologic evolution of Taiwan, *Tectonophysics*, *125*(1–3), 1–16.

Hou, C. S., J. C. Hu, K. E. Ching, Y. G. Chen, C. L. Chen, L. W. Cheng, C. L. Tang, S. H. Huang, and C. H. Lo (2009), The crustal deformation of the Ilan Plain acted as a westernmost extension of the Okinawa Trough, *Tectonophysics*, *466*(3–4), 344–355.

Huang, B. S., C. Y. Wang, D. Okaya, S.-J. Lee, Y.-C. Lai, F. T. Wu, W.-T. Liang, and W.-G. Huang (2013), Multiple Diving Waves and Steep Velocity Gradients in the Western Taiwan Coastal Plain: An Investigation Based on the TAIGER Experiment, *Bull. Seismol. Soc. Am.*, *103*(2A), 925–935, doi:10.1785/0120110047.

Huang, C.-Y., P. B. Yuan, C.-W. Lin, T. K. Wang, and C.-P. Chang (2000), Geodynamic processes of Taiwan arc–continent collision and comparison with analogs in Timor, Papua New Guinea, Urals and Corsica, *Tectonophysics*, *325*(1–2), 1–21, doi:10.1016/S0040-1951(00)00128-1.

Jarchow, C. M., G. A. Thompson, R. D. Catchings, and W. D. Mooney (1993), Seismic evidence for active magmatic underplating beneath the Basin and Range province, western United States, *J. Geophys. Res.*, *98*(B12), 22095.

Jhiang, S. C. (1976), Seismic exploration of the Ilan Plain, *Min Tech Dig*, *14*, 215–221.

Kallweit, R. S., and L. C. Wood (1982), The limits of resolution of zero-phase wavelets, *Geophysics*, *47*, 1035.

Kang, C.-C., C.-P. Chang, L. Siame, and J.-C. Lee (2015), Present-day surface deformation and tectonic insights of the extensional Ilan Plain, NE Taiwan, *J. Asian Earth Sci.*, *105*, 408–417, doi:10.1016/j.jseaes.2015.02.013.

Kizaki, K. (1986), Geology and tectonics of the Ryukyu Islands, *Tectonophysics*, *125*(1–3), 193–207, doi: 10.1016/0040-1951(86)90014-4.

Konstantinou, K. I., C.-Y. Pan, and C.-H. Lin (2013), Microearthquake activity around Kueishantao island, offshore northeastern Taiwan: Insights into the volcano–tectonic interactions at the tip of the southern Okinawa Trough, *Tectonophysics*, *593*, 20–32, doi:10.1016/j.tecto.2013.02.019.

Ku, C.-Y., S.-K. Hsu, J.-C. Sibuet, C.-H. Tsai, and others (2009), The Neo-tectonic structure of the southwestern tip of the Okinawa Trough, *Terr. Atmospheric Ocean. Sci.*, *20*(5), 749.

Kuo-Chen, H., F. T. Wu, and S. W. Roecker (2012), Three-dimensional P velocity structures of the lithosphere beneath Taiwan from the analysis of TAIGER and related seismic data sets, *J. Geophys. Res. Solid Earth*, *117*(B6), B06306, doi: 10.1029/2011JB009108.

Kuo-Chen, H., F. Wu, W.-L. Chang, C.-Y. Chang, C.-Y. Cheng, and N. Hirata (2015), Is the Lishan fault of Taiwan active?, *Tectonophysics*, *661*, 210–214.

Lai, K.-Y., Y.-G. Chen, Y.-M. Wu, J.-P. Avouac, Y.-T. Kuo, Y. Wang, C.-H. Chang, and K.-C. Lin (2009), The 2005 Ilan earthquake doublet and seismic crisis in

northeastern Taiwan: evidence for dyke intrusion associated with on-land propagation of the Okinawa Trough, *Geophys. J. Int.*, *179*(2), 678–686.

Lee, J. C., J. Angelier, and H. T. Chu (1997), Polyphase history and kinematics of a complex major fault zone in the northern Taiwan mountain belt: the Lishan Fault, *Tectonophysics*, *274*(1–3), 97–115.

Lester, R., L. L. Lavier, K. McIntosh, H. J. A. V. Avendonk, and F. Wu (2012), Active extension in Taiwan's precollision zone: A new model of plate bending in continental crust, *Geology*, *40*(9), 831–834, doi:10.1130/G33142.1.

Lester, R., K. McIntosh, H. J. A. Van Avendonk, L. Lavier, C.-S. Liu, and T. K. Wang (2013), Crustal accretion in the Manila trench accretionary wedge at the transition from subduction to mountain-building in Taiwan, *Earth Planet. Sci. Lett.*, *375*, 430–440, doi:10.1016/j.epsl.2013.06.007.

Liu, C. C. (1995), The Ilan plain and the southwestward extending Okinawa trough, *J.-Geol. Soc. CHINA-TAIWAN-*, *38*, 229–242.

Liu, C. S., I. L. Huang, and L. S. Teng (1997), Structural features off southwestern Taiwan, *Mar. Geol.*, *137*(3–4), 305–319.

Lüschen, E., F. Wenzel, K. J. Sandmeier, D. Menges, T. Rühl, M. Stiller, W. Janoth, F. Keller, W. Söllner, and R. Thomas (1987), Near-vertical and wide-angle seismic surveys in the Black Forest, SW Germany, *J Geophys*, *62*, 1–30.

Lüschen, E., S. Sobolev, U. Werner, W. Söllner, K. Fuchs, B. Gurevich, and P. Hubral (1993), Fluid reservoir (?) beneath the KTB drillbit indicated by seismic shear-wave observations, *Geophys. Res. Lett.*, *20*(10), PP. 923-926, doi: 199310.1029/93GL00685.

Pratt, T. L., E. C. Hauser, T. M. Hearn, and T. J. Reston (1991), Reflection polarity of the midcrustal Surrency bright spot beneath southeastern Georgia: Testing the fluid hypothesis, *J Geophys Res*, *96*, 10–145.

Reiter, M., A. J. Mansure, and C. Shearer (1979), Geothermal characteristics of the Rio Grande Rift within the southern Rocky Mountain complex, *Rio Gd. Rift Tecton. Magmat.*, 253–297.

Sanford, A. R., O. Alptekin, and T. R. Toppozada (1973), Use of reflection phases on microearthquake seismograms to map an unusual discontinuity beneath the Rio Grande rift, *Bull. Seismol. Soc. Am.*, *63*(6–1), 2021.

Sheriff, R. E. (1975), Factors affecting seismic amplitudes, *Geophys. Prospect.*, *23*(1), 125–138.

Shyu, J. B. H., K. Sieh, Y.-G. Chen, and C.-S. Liu (2005), Neotectonic architecture of Taiwan and its implications for future large earthquakes, *J. Geophys. Res. Solid Earth*, *110*(B8), B08402, doi: 10.1029/2004JB003251.

Sibuet, J. C., B. Deffontaines, S. K. Hsu, N. Thareau, and others (1998), Okinawa trough backarc basin: Early tectonic and magmatic evolution, *J. Geophys. Res.*, *103*(B12), 30245.

Smythe, D. K., A. Dobinson, R. McQuillin, J. A. Brewer, D. H. Matthews, D. J. Blundell, and B. Kelk (1982), Deep structure of the Scottish Caledonides revealed by the MOIST reflection profile, *Nature*, *299*, 338–340.

Stern, T. A., S. A. Henrys, D. Okaya, J. N. Louie, M. K. Savage, S. Lamb, H. Sato, R. Sutherland, and T. Iwasaki (2015), A seismic reflection image for the base of a tectonic plate, *Nature*, *518*(7537), 85–88.

Suppe, J. (1980), Imbricated structure of western foothills belt, southcentral Taiwan, *Pet. Geol Taiwan*, *17*, 1–16.

Teng, L. S. (1990), Geotectonic evolution of late Cenozoic arc-continent collision in Taiwan, *Tectonophysics*, *183*(1–4), 57–76, doi: 10.1016/0040-1951(90)90188-E.

Tillman, K. S., and T. B. Byrne (1995), Kinematic analysis of the Taiwan Slate Belt, *Tectonics*, *14*(2), 322–341, doi: 10.1029/94TC02451.

Tong, L. T., S. Ouyang, T. R. Guo, C. R. Lee, K. H. Hu, C. L. Lee, and C. J. Wang (2008), Insight into the geothermal structure in Chingshui, Ilan, Taiwan, *Terr Atmos Ocean Sci*, *19*, doi:10.3319/TAO.2008.19.4.000(T).

Van Avendonk, H. J., K. D. McIntosh, H. Kuo-Chen, L. L. Lavier, D. A. Okaya, F. T. Wu, C.-Y. Wang, C.-S. Lee, and C.-S. Liu (2016), A lithospheric profile across northern Taiwan: from arc-continent collision to extension, *Geophys. J. Int.*, *204*(1), 331–346.

Van Avendonk, H. J. A., H. Kuo-Chen, K. D. McIntosh, L. L. Lavier, D. A. Okaya, F. T. Wu, C. Y. Wang, C. S. Lee, and C. S. Liu (2014), Deep crustal structure of an arc-continent collision: Constraints from seismic traveltimes in central Taiwan and the Philippine Sea, *J. Geophys. Res. Solid Earth*, *119*(11), 8397–8416.

de Voogd, B., L. Serpa, L. Brown, E. Hauser, S. Kaufman, J. Oliver, B. W. Troxel, J. Willemin, and L. A. Wright (1986), Death Valley bright spot: A midcrustal magma body in the southern Great Basin, California?, *Geology*, *14*(1), 64–67, doi:10.1130/0091-7613(1986)14<64:DVBSAM>2.0.CO;2.

Wu, F. T., R. J. Rau, and D. Salzberg (1997), Taiwan orogeny: thin-skinned or lithospheric collision? *Tectonophysics*, *274*(1–3), 191–220.

Wu, F. T., W. T. Liang, J. C. Lee, H. Benz, and A. Villasenor (2009), A model for the termination of the Ryukyu subduction zone against Taiwan: A junction of collision, subduction/separation, and subduction boundaries, *J Geophys Res*, *114*.

Yang, T. F., T. F. Lan, H.-F. Lee, C.-C. Fu, P.-C. Chuang, C.-H. Lo, C.-H. Chen, C.-T. A. Chen, and C.-S. Lee (2005), Gas compositions and helium isotopic ratios of fluid samples around Kueishantao, NE offshore Taiwan and its tectonic implications, *Geochem. J.*, *39*(5), 469–480.

Yilmaz, Ö. (2001), *Seismic Data Analysis*, Investigations in Geophysics, Society of Exploration Geophysicists.

CHAPTER 3

SEISMIC INTERFEROMETRY OF RAILROAD INDUCED GROUND MOTIONS: BODY AND SURFACE WAVE IMAGING

3.1 Abstract

Seismic interferometry applied to 120 hours of railroad traffic recorded by an array of vertical component seismographs along a railway within the Rio Grande rift has recovered surface and body waves characteristic of the geology beneath the railway. Linear and hyperbolic arrivals are retrieved that agree with surface (Rayleigh), direct and reflected P waves observed by nearby conventional seismic surveys. Train-generated Rayleigh waves span a range of frequencies significantly higher than those recovered from typical ambient noise interferometry studies. Direct P wave arrivals have apparent velocities appropriate for the shallow geology of the survey area. Significant reflected P wave energy is also present at relatively large offsets. A common midpoint stack produces a reflection image consistent nearby conventional reflection data. We suggest that for sources at the free surface (e.g. trains) increasing the aperture of the array to record wide angle reflections, in addition to longer recording intervals, might allow the recovery of deeper geologic structure from railroad traffic. Frequency-wavenumber analyses of these recordings indicate that the train source is symmetrical (i.e. approaching and receding) and that deeper refracted energy is present although not evident in the time-offset domain. These results confirm that train generated vibrations represent a practical source of high resolution

The material in Chapter 3 has been published under Quiros et al., Seismic interferometry of railroad induced ground motions: body and surface wave imaging. *Geophys. J. Int.* (2016) **205**, 301-313

subsurface information, with particular relevance to geotechnical and environmental applications.

3.2 Introduction

Claerbout, [1968] showed that the autocorrelation of the transmission response of a horizontally layered medium results in its reflection response. He later suggested that by cross-correlating the records from two locations on the surface, one can retrieve the response that would be recorded at one of these locations as if there were a source at the other. Although early seismological attempts to confirm Claerbout's conjecture were inconclusive [*Baskir and Weller*, 1975; *Cole*, 1995], independent work in helioseismology [*Duvall et al.*, 1993] and ultrasonics [*Lobkis and Weaver*, 2001; *Weaver and Lobkis*, 2001] demonstrated its validity. The work of *Lobkis and Weaver*, [2001] on diffuse ultrasonic fields, for example, established from both theoretical and experimental approaches that the Green's function (i.e. the response to an impulsive source) between two receivers could be recovered by temporal cross-correlation of those records. This concept, now known as seismic interferometry, has been developed by a number of authors, including *Schuster*, [2001], *Snieder et al.*, [2002], *Wapenaar*, [2003], [2004], *Bakulin and Calvert*, [2004], *Schuster et al.*, [2004], *Snieder*, [2004], and *Wapenaar and Fokkema*, [2006].

Many seismic interferometry studies to date have concentrated on the ambient seismic field generated by natural processes. This natural field has been shown to be generated by different mechanisms at different frequency bands. For example, one widely used source of natural energy are microseisms (surface waves) observed between 0.04 – 0.08 Hz, which have been linked to ocean swells at coastal regions

[*Haubrich et al.*, 1963]. The random pressure fluctuations generated by ocean waves have been shown sufficient to generate microseisms of considerable amplitude [*Hasselmann*, 1963]. *Longuet-Higgins*, [1950] established that a secondary type of microseismic energy, with dominant peak frequencies between 0.1 – 0.16 Hz, results from the nonlinear interaction of pairs of ocean swell trains. The low frequency (0.001 – 0.01 Hz) part of the Earth's background free oscillations, the "hum", is the least understood. Some have attributed this to atmospheric turbulence [*Nishida et al.*, 2000; *Tanimoto*, 2001], though recent work indicates that the "hum" results from the mechanisms responsible for the primary and/or secondary microseism [*Webb*, 2007, 2008; *Traer and Gerstoft*, 2014; *Ardhuin et al.*, 2015].

The ambient seismic field from natural sources is well known to be dominated by fundamental mode surface waves below frequencies of 0.1 Hz [*Haubrich et al.*, 1963; *Toksöz and Lacoss*, 1968; *Ekström*, 2001]. As a result ambient noise tomography using surface waves has developed into a robust imaging technique, allowing seismologists to image the Earth at local [*Brenguier et al.*, 2007; *Lin et al.*, 2013b], regional [*Shapiro et al.*, 2005; *Kang and Shin*, 2006; *Yao et al.*, 2006; *Yang et al.*, 2007], and global scales [*Nishida et al.*, 2009]. At frequencies above 0.1 Hz the ambient seismic field is a complicated mixture of fundamental mode surface waves, higher mode surface waves, and body waves [*Bonnefoy-Claudet et al.*, 2006; *Koper et al.*, 2010]. The extraction of body waves from the ambient seismic field generated by natural processes has proven to be more difficult than for surface waves, although various degrees of success have been reported [*Roux et al.*, 2005; *Draganov et al.*,

2007, 2009; *Zhan et al.*, 2010; *Poli et al.*, 2011; *Ruigrok et al.*, 2011; *Ryberg*, 2011; *Lin et al.*, 2013a].

The anthropogenic contribution to the ambient seismic field has been addressed by only a few interferometry studies. Thus far, *Matsuoka et al.*, [2006] and *Shiraishi et al.*, [2006], to our knowledge, are the first attempts to image geologic structure using seismic interferometry with vehicles as sources. *Halliday et al.*, [2008] also recovered surface waves from vehicles. *Miyazawa et al.*, [2008] observed vertical P and S wave propagation in a monitoring well from vibrations caused by mechanical equipment operating around the top of the well. *Nakata et al.*, [2011] retrieved shear-wave (i.e. refracted and reflected) and Love-wave energy from recordings of railways and highways. *Behm and Snieder*, [2013] and *Behm et al.*, [2014] extracted surface waves from highway records. Imaging with drilling noise in oil exploration is perhaps the most mature example of the use of anthropogenic "noise" in this context [*Rector III and Marion*, 1991; *Poletto and Miranda*, 2004].

The work presented here reports our attempt to use the ambient seismic field generated by trains to produce virtual records of surface and body waves for imaging the subsurface.

3.3 The Belen Experiment

In May 2014 one hundred vertical component geophones (Geospace GS-11D 4.5 Hz) coupled with Ref Tek 125A recorders (Texans) were deployed parallel to a busy section of the Burlington Northern Santa Fe (BNSF) railway near Belen, New Mexico (Fig. 3.1). The array used a spacing of approximately 25 m between seismographs for a total array length of 2475 m. The Texans acquired data

continuously for 120 hours between 29 May and 3 June 2014. We had excellent data recovery, with only one station failing completely. A sampling rate of 0.004 s (250 Hz) was used, corresponding to a Nyquist frequency of 125 Hz.

The site was chosen for several reasons: a) it has one of the largest volumes of train traffic in the southern transcontinental corridor, approximately 90 trains per day with some being 3 km long [*Frailey*, 2007], b) it is in close proximity to the IRIS-PASSCAL instrument center which provided the instrumentation for the deployment, and c) it is located within the Rio Grande rift, an area which has been subject to many previous geophysical studies [*Sanford and Long*, 1965; *Schmucker*, 1970; *Decker and Smithson*, 1975; *Ramberg and Smithson*, 1975], including the COCORP deep seismic reflection surveys in 1976 and 1977 [*Brown et al.*, 1979].

3.3.1 Inspection of Recordings

The continuous data set of 120 hours was divided into hour-long sections and filtered to remove the nonzero mean value (DC component) of the waveforms inherent in the Texan recorders. While inspecting the raw records we recognized 2 major types of signals: trains and road vehicles (cars and trucks). Trains were identified based on the temporal length of the vibrations at each station and the velocity of the signal as it traversed the array, while vehicle signatures on the two main gravel roads parallel to the railroad are identified from field notes, relative amplitudes, and temporal length of the vibrations. A third type of signal, bursts of "noise" of much lower relative amplitude to trains and vehicles, we associate with wind gusts. The records contained 231 clear train signals traveling westbound and 199 clear train signals traveling eastbound, along with 59 vehicles, and 94 bursts of noise. These represent a total of

583 specific “events” averaging 116.6 per day. The time interval between trains ranged from a few seconds for trains traveling in opposite directions (the railroad consisted of 2 parallel tracks) to over an hour between trains. Fig. 3.2 shows an example of an hour-long record that contains signals that correspond to trains and other vehicles.

3.3.2 Spectral character of recordings

The train signals T 1, T 2, and T 5 in Fig. 3.2 were investigated using a master trace (top row Fig. 3) derived from summing all traces after aligning the train signals using a time shift (i.e. linear moveout correction) obtained from the average velocity of the train. Spectrograms and amplitude spectra for these master traces are shown in Fig. 3.3. The spectra show substantial energy from about 4.5 Hz (the geophone natural frequency) up to about 50 Hz, with discernible energy as high as 110 Hz. Peak amplitudes occur between 5 to 20 Hz. Note that a Doppler effect is evident in the spectrograms, with higher frequency content present at earlier times (i.e. approaching train) and the absence of those higher frequencies at later times (i.e. receding train).

3.4 Seismic Interferometry

Initial interferometric processing consisted of treating all hour-long records equally, without making a distinction among different signals (i.e. trains, cars, wind noise, quiet periods). Several frequency band-pass filters and amplitude-normalization routines were tested for pre-processing of the records (details below). After pre-processing, the positive lags of the cross-correlation are computed in the time domain for each hour-long record. The procedure selects a station to cross-correlate against the remaining stations, resulting in 120 cross-correlation records for the selected station.

These cross-correlation panels are then normalized by the root-mean square (rms) value of the amplitude of the panel, to equalize the amplitude from panel to panel, and then summed (stacked). This is then repeated for all stations, resulting in the computation of the negative lags of the cross-correlation (note that computing the positive lags of the cross-correlation of station A with station B and of station B with station A results in the complete cross-correlation function). The positive lags of the correlation are what we here refer to as a virtual-shot gather, while the negative lags are what we here refer to as a virtual-receiver gather. The sum of both the positive and negative lags for each station results in what we here refer to as a virtual-source gather.

Fig. 3.4 shows several versions of a typical virtual-shot gather (positive lags only) corresponding to the selection of receiver 55 as the source. Each panel varies in terms of the pre-processing steps applied. Fig. 3.4(a) results from applying an rms normalization with a 1 hour window to each trace, and an rms panel-to-panel normalization prior to the correlation step. The result shows relatively weak energy propagating linearly with apparent velocities between 300 and 800 m/s, velocities that suggest surface wave energy. One-bit amplitude normalization (e.g. sign-bit) [*Bond and Cahn*, 1958] applied to the raw recordings prior to correlation results in the recovery of much stronger linear, and quasi-linear, arrivals (Fig. 3.4b). Again, based on their apparent velocities, we interpret these as Rayleigh waves. Moreover, as a range of slopes (apparent velocity) is evident for this energy, we infer that it is dispersive. As we will show later in this paper, these arrivals are a robust basis for velocity inversion using surface-wave techniques. Because normalizing with respect to

the entire trace (1 hour window) runs the risk of anomalous scaling by strong amplitude signals (e.g. noise bursts or spikes), various moving windows were also tested to normalize the amplitude prior to cross-correlation. Those tests mimic the results obtained in Fig. 3.4(a) for very large windows (30 minutes), and those obtained in Fig. 3.4(b) for very small windows (20 seconds). In order to suppress the surface-wave contributions and enhance body-wave recovery, an rms amplitude scaling using a window of 12500 samples (i.e. 50 s windows) and a 16 – 100 Hz band-pass filter were applied prior to computing the correlations. The resulting virtual-shot gather (Fig. 3.4c) clearly exhibits linear arrivals with much higher apparent velocities for at least the positive offsets. Application of a 16 – 100 Hz filter followed by one-bit normalization prior to correlation (Fig. 3.4d) recovered the same linear events observed in Fig. 3.4(c), propagating in the positive and negative offset directions with much stronger amplitudes. These events have much higher apparent velocities than those of the surface waves observed in Figs 3.4a and b, and as argued below, represent P waves. Clearly one-bit amplitude normalization is an effective tool for enhancing virtual energy associated with both surface and body waves when applied in conjunction with the appropriate band-pass filter. As noted by *Cupillard et al.*, [2011] this method retrieves any coherent energy present between two receivers, in the case of Fig. 3.4(b) the most abundant energy corresponds to surface waves, while in Fig. 3.4(d), one-bit pre-processing is retrieving coherent energy present at higher frequencies.

Inspection of the positive and negative lags of the cross-correlations shows that for the retrieved surface (Fig. 3.5a) and body (Fig. 3.5b) waves the illumination can be

considered close to symmetric, implying that railroad vibrations illuminate the array in the same manner for either travel direction of the trains. This is to be expected since each train "broadcasts" in both directions to the array as it approaches and recedes (see also FK analysis below).

Comparison (Fig. 3.4d) of our virtual-shot gathers with physical shot gathers from the COCORP survey collected within similar Tertiary-Quaternary sedimentary rocks of the Rio Grande valley shows that the high velocities (i.e. ~ 2100 m/s) associated with the linear first arrivals recovered from interferometry correspond closely with the velocity of the real P waves traveling in the near-surface sedimentary rocks (Fig. 3.6).

In addition to what we interpret as clear direct P waves on the virtual gathers, there are later arrivals that exhibit curvature suggestive of the hyperbolic moveout expected of reflections. The hyperbolic events, most obvious in virtual source gathers at larger offsets, correspond to a reflector at approximately 0.72 s vertical two-way time (twt) or ~ 750 below the surface, and a normal moveout (NMO) velocity of approximately 2075 m/s (Fig. 3.7). The reflected arrival is not fully aligned at large offsets by the standard NMO correction (e.g. Fig. 3.7c). This may be due to the presence of a shallow weathering layer and or by use of an NMO correction where the 4^{th} and higher order terms are neglected [*Yilmaz*, 2001]. Frequency distortion (NMO stretching) is common at large offsets and shallow arrival times [*Yilmaz*, 2001]. Usually data that suffer NMO stretching are muted prior to processing. However, since the energy of interest lies completely within the “stretch” regime, an alternative approach is taken here. Fig. 3.7(e) shows the virtual-shot gather in Fig. 3.6(a) after

applying a constant normal moveout (CNMO) correction [*Shatilo and Aminzadeh*, 2000], which assumes that the seismic wavelet is primarily from a single interface at depth. The travel times of this particular reflected phase agree with the two-way times (0.6 – 0.9 s) observed by *Russell and Snelson,* [1994] for the contact between upper Tertiary sedimentary rocks (Santa Fe group) and Paleozoic sedimentary rocks 10 km south of our array.

3.5 Frequency-wavenumber Analysis of Train Sources

While body and surface waves can be retrieved with relative simple pre-processing, up to this point it is unclear which components of the recordings (e.g. background "noise", approaching vs. receding train, etc.) contribute to the emergence of the different seismic phases observed. To address this issue we carried systematic frequency-wavenumber (f-k) analyses of the raw recordings using short time windows (i.e. 100 s) on several records. Fig. 3.8 shows three hour-long records of raw data (filtered to remove nonzero mean value and amplitude normalized) that are adjacent in time (hour 12, hour 13, and hour 14). Hour 12 contains four train signals (the signal at the beginning of the record corresponds to a train close to the one hour mark on the record for the preceding hour 11). Three windows of data were extracted from hour 12 to represent the approaching, passing, and receding part of the fourth train signal. Hour 13 is the only 60 minute record in the entire data set that does not appear to contain any train signals or vehicles. The first window in this record was chosen to start after an hour had passed since the last train went by the array. Hour 14 contains three train signals. The first window extracted from this record represents a "quiet" period; the second and third windows correspond to the approaching and receding

parts of the train signal in the record. Each window (red rectangle) in Fig. 3.8 was transformed into the f-k domain. The convention used in the f-k plots shown here (Fig. 3.9) is that events that dip down to the right (i.e. direction of travel is northwest to southeast in Fig. 3.1b) are assigned negative wavenumbers, while events that dip up to the right (i.e. direction of travel is southeast to northwest in Fig. 3.1b) are assigned positive wavenumbers.

The f-k transforms in Figs 3.9a-c correspond to the three windows selected in hour 12 (Fig. 3.8a), from earliest to last. The approaching train signal in Fig. 3.8(a) (earliest window) has a negative wavenumber according to the convention used here, corresponding to travel direction from northwest to southeast. Fig. 3.9(a) shows strong-amplitude signals with negative wavenumbers. The linear energy bands in the f-k plots represent surface and body waves, with the latter corresponding to the steeper slopes (high apparent velocities). Two distinct bands of "slow" energy are apparent in Fig. 3.9(a), which we attribute to the fundamental mode (V ~ 400 m/s), spatially aliased at about 8 Hz, and a higher mode (V ~ 600 m/s), spatially aliased at about 11 Hz, of surface wave propagation.

Fig. 3.9(b) suggests that most of the energy arrives with infinite (e.g. horizontal) apparent velocity, consistent with the train being largely parallel to and spanning the array. In this case the seismic energy is largely arriving broadside to the array.

Fig. 3.9(c) shows the train signal as it is receding. As expected, the energy propagates in the direction opposite to that when the train was approaching (e.g. Fig. 3.9a). Similarly to Fig. 3.9(a), Fig. 3.9(c) clearly shows events whose slopes suggest

both body and surface waves. Here, however, at least three distinct bands of surface wave energy are evident, with apparent velocities of 400, 600, and 750 m/s. We again interpret these a fundamental and higher mode surface waves. In Figs 3.9a-c there are also horizontal bands of energy (e.g. at 12, 18, 24, and 30 Hz). Such monotonic noise can be a serious contaminant in cross-correlations, especially if this noise is stationary in time and space, effectively "drowning out" recovery of propagating seismic energy [*Draganov et al.*, 2009]. This does not seem to be a problem with this dataset, possibly due to these energy bands being unstable in time.

Figs 3.9d-f correspond to the time windows in Fig. 3.8(b) where much less, if any, train energy should be present. These plots therefore characterize the "background" seismic energy upon which the train energy is presumably superimposed. All three of the background f-k plots show surface-wave energy propagating somewhat more symmetrically than when the train energy is dominant. Slopes corresponding to body-wave energy are also present, albeit at somewhat weaker levels and dominantly traveling from northwest to southeast. We speculate that the surface-wave energy may be due to cultural noise from the town of Belen (Fig. 3.1), or perhaps highway traffic noise from the several highways which pass near Belen with a north-south orientation. Whereas the body-wave energy is perhaps excited by a distant train traveling from northwest to southeast, towards the railroad station in the town of Belen.

Figs 3.9g-i correspond to the three windows in hour 14 (Fig. 3.8c). The f-k plot in Fig. 3.9(g) examines a "quiet" period within hour 14. Although hints of surface-wave energy are present no body-wave energy is visible. Notice that background

amplitudes for this window are even lower than the ones in record 13. Figs 3.9h and 3.9i represent the approaching and receding train signal, respectively. The reversals in the slopes of body and surface-wave energy correspond to the signal directivity.

The direct wave that is so clear in the virtual-shot gathers (e.g. Figs 3.4c and 3.4d) is also prominent in all of the f-k spectra with a velocity (V ~ 2.1 km/s) that matches that derived from the slope of the virtual travel time curves. Like the surface waves, it appears strongest in the direction toward the approaching or receding train source. However, we also note that in some of the spectra there appears to be two linear arrivals with body wave type velocities. These are most evident in Figs 3.9c and 3.9h, with apparent velocities of approximately 4 km/s. We interpret these (e.g. P_r in Fig. 3.9h) as corresponding to critically refracted, or head wave, energy from deeper subsurface discontinuities. Corresponding linear arrivals are not evident in any of the virtual gathers computed by the various pre-processing sequences (e.g. Fig. 3.4), implying that such energy is fairly weak compared to the direct P energy, which is often the case for head waves [e.g. *Grant and West*, 1965]. *Mikesell et al.*, [2009] describe the interferometric treatment of these refracted arrivals, and introduce the term *virtual refraction* to refer to the spurious energy observed in virtual gathers due to these phases. Interestingly, these faster linear arrivals are also evident in the f-k spectra for the background noise (e.g. Fig. 3.9e and f) as well as those for the train sources.

The f-k analysis in Fig. 3.9 indicates that the most useful energy from the train sources occur when the trains are either approaching or leaving the array. When the train is “on the array”, energy arriving “broadside” is clearly swamping any useful

surface or body wave information. However, this energy could be useful for instruments placed perpendicular to our array.

While applying the same f-k analysis to signals such as vehicles and sources other than trains (i.e. wind gusts) surface waves are clearly observed but body waves do not appear to be present (Fig. 3.10). This suggests that these sources are not as efficient as trains, at least in generating body-wave energy.

3.5.1 Seismic interferometry guided by f-k analysis

To determine if body waves might be more effectively extracted if the "broadside" train, vehicle, and wind energy were removed from the correlations, the results shown in Fig. 3.11 were computed. Fig. 3.11(a) shows a brute correlation using all the energy (as in Fig. 3.4d). Fig. 3.11(b) shows the result of pre-processing with a 50 s rms window for amplitude normalization, panel-to-panel equalization, a band-pass filter (16-100), and muting (i.e. deleting) of signals from vehicles, wind, and broadside train energy. Similarly, Fig. 3.11(c) shows of the result of the same pre-processing with the addition of a 20 Hz notch filter. The notch filter was chosen to eliminate a narrow peak present in the amplitude spectrum of Figs 3.11a and 3.11b. Fig. 3.11(d) shows the result of pre-processing with a 50 s rms window for amplitude normalization, panel-to-panel equalization, an f-k filter, and the same muting used in Figs 3.11b and 3.11c. In spite of our expectation that this muting would be helpful, the resulting virtual-shot gathers (Fig. 3.11b) show no significant improvement in terms of recovery of body-wave energy. We also tried applying a notch filter prior to correlation and stacking to remove a 20 Hz monotonic energy present in Figs 3.11b and 3.11c. As mentioned early, monotonic "noise" can frequently obscure propagating

seismic energy. However, the removal of this particular frequency does not result in any improvement in the virtual shot gather (Fig. 3.11c). In general we see little evidence of the influence of monotonic noise in our correlations, perhaps because the frequencies of such noise are unstable in time (e.g. Fig. 3.9). In addition, f-k filtering was tested as a means to remove surface-wave energy prior to computing the correlations without sacrificing any low-frequency body wave energy that might be present. However, the result (Fig. 3.11d) fails to show any significant new body wave arrivals.

3.6 Reflection Imaging

The obvious next step in using the virtual-source gathers (i.e. sum of positive and negative correlation lags) is to apply common midpoint (CMP) processing to generate a stacked seismic section. The processing sequence included linear moveout velocity picks to guide automated first arrival picks, editing of first arrival picks, mute function for first arrivals, elevation statics, amplitude scaling, surface consistent deconvolution, constant NMO correction [*Shatilo and Aminzadeh*, 2000], CMP stacking, and amplitude scaling.

The resulting stacked section (Fig. 3.12) shows coherent events, but only down to 0.8 s twt. The most prominent event is the reflector previously identified in Fig. 3.7 at about 0.72 s twt. We associate this reflector with the contact between Tertiary and Paleozoic sedimentary rocks based on the interpretation of conventional seismic data nearby [e.g. *Russell and Snelson*, 1994]. Although shallow reflectivity is apparently recovered, it is far from strong and deeper events are not observed. It is also apparent from inspection of the virtual shot gathers that the energy that is contributing to the

reflection stack is coming at "wide" vs. "near-vertical" angles. Given the limited aperture of our spread (ca. 2.5 km), only the shallow reflectors correspond to illumination at relatively wide angles.

Draganov et al., [2006] and *Forghani and Snieder,* [2010] make clear the importance of the source distribution in seismic interferometry. Ideally for near-vertical reflection imaging using interferometry, sources should be distributed beneath the recording array [*Draganov et al.,* 2006; *Ruigrok et al.,* 2010]. In contrast, the train source is restricted to the surface with most of its energy propagating horizontally across our array.

The studies of *Zhan et al.,* [2010] and *Poli et al.,* [2011] which report deep reflections (e.g. Moho) suggest that relevant illumination occurs near-horizontally, with the retrieved reflections observed at wide angles. *Zhan et al.,* [2010] reason that sources must be distributed within the crust (at the free surface and at depth), but that the crust behaves as a wave guide for near-horizontally travelling body-wave energy (i.e. SmS^n).

The lack of deeper reflections recovered by our analysis could also be due in part to the very short length of our recording period, 5 days. *Zhan et al.,* [2010] and *Poli et al.,* [2011] reported their wide-angle Moho reflections based on 6 months and 1 year of data, respectively. Although *Ruigrok et al.,* [2011] report Moho reflections from approximately 40 hours of data collected over the Northeast Abu Gharadig Basin in Egypt, they attribute their success to having near surface noise sources sufficiently far away that the relevant energy is actually arriving near vertically from beneath the array due to the velocity gradient in the crust and mantle.

Based on these observations as well as our own analysis, we suggest that deeper reflection imaging with train sources will require a much larger virtual source to receiver offsets, and longer recording time.

3.7 Surface Waves

It is abundantly clear from Figs 3.4 and 3.9 that trains are an exceptionally good source of surface-wave energy, with substantial potential for mapping subsurface structure via inversion of their dispersion curves. Moreover, the surface-wave energy provided by trains is richer in high frequencies (1-14 Hz) than those from microseism-based interferometry at both crustal [*Bensen et al.*, 2007] and shallow [*Lin et al.*, 2013b] scale frequencies (i.e. crustal 0.05-2 Hz, shallow 0.5-4 Hz).

Here, by way of demonstration, we computed a simple 1-D shear-wave velocity model by inversion of the dispersion curve for a particular virtual-shot gather. Fig. 3.13(a) shows the virtual-shot gather for station 5 generated via one-bit normalization pre-processing, together with its corresponding dispersion curve (Fig. 3.13b). The dispersion curve clearly shows both fundamental- and higher-mode Rayleigh wave energy. Inversion of the fundamental mode [*Wathelet et al.,* 2004; *Wathelet*, 2008] in the frequency range 0 – 8 Hz (unaliased surface waves) resulted in the 1-D shear wave velocity model shown in Fig. 3.13(c). We did not attempt inversion of the higher mode energy as it may have been inaccurately recovered [*Halliday and Curtis*, 2008; *Kimman and Trampert*, 2010]. Note that direct correlation of the surface wave velocity structure with the body wave reflectivity is of limited valued, since the surface waves probe only the very shallowest portion (e.g. less than 200 m, or 0.2 s twt) of the subsurface, a portion that is non-reflective in the seismic

section in Fig. 3.12. However, the P wave velocity of ca 2.0 km/s derived from the virtual shot gather is consistent with the S wave velocities indicated by the surface-wave inversion (ca 1.0 km/s).

Our surface-wave results are comparable to those reported by *Nakata et al.*, [2011] also using highway and train recordings. These suggest that train energy represents a promising source for mapping shallow shear-wave velocity variations at shallow depths, with possible application to geotechnical issues, ranging from hydrology to seismic site response.

3. 8 Conclusions

Virtual gathers obtained from cross-correlation of railroad traffic exhibit robust dispersive surface wave (Rayleigh) energy at frequencies higher than those obtained from conventional interferometry using microseism energy. As such, data generated by train traffic should prove valuable for a range of near-surface applications of surface-wave tomography. Potentially useful body-wave (P) energy can also be recovered for refraction/reflection imaging of the subsurface. Although the reflection image produced in this case only reaches to 1 km depth, in principle greater depths and fidelity should be attained by simply recording/stacking for longer periods of time and or using more favorable recording geometries (e.g. larger apertures).

The results presented here and from previous studies suggest that careful consideration should be given to using the "noise" from railroads as an effective source for surface wave and reflection imaging of at least the shallow subsurface over large areas at relatively low cost.

3.9 Figures

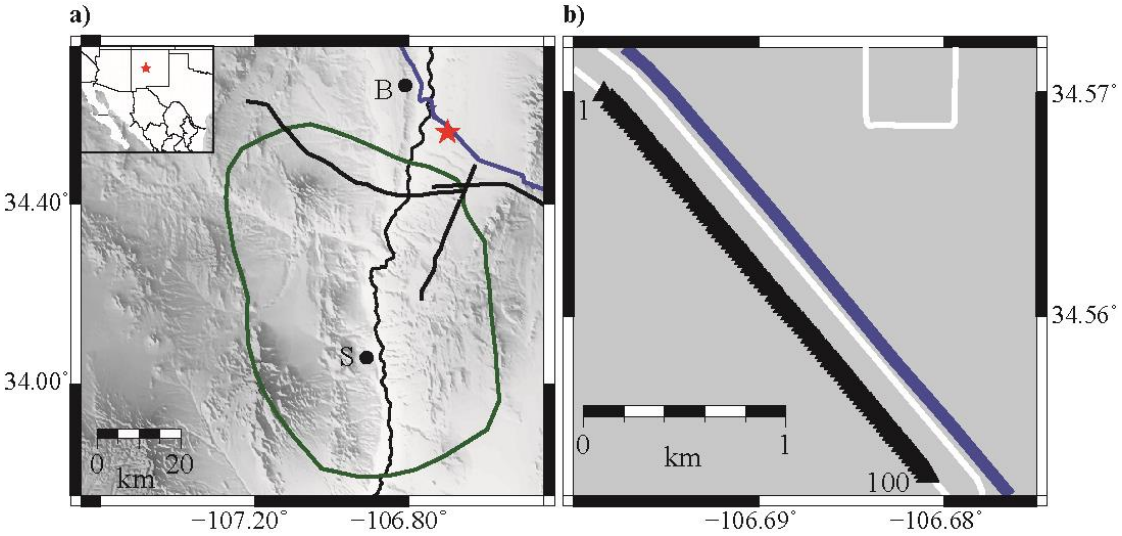

Figure 3.1: (a) Survey location (red star) relative to the towns of Belen (B) and Socorro (S). Also shown are the Rio Grande river (meandering north–south black line), the outline (green line) of the Socorro Magma Body [*Balch et al.*, 1997], and the COCORP deep seismic profiles (bold black lines) [*Brown et al.*, 1979]. Inset map shows survey location (red star) within New Mexico. (b) Distribution of seismographs (black triangles) paralleling the BNSF railway (blue line) with local gravel roads shown in white.

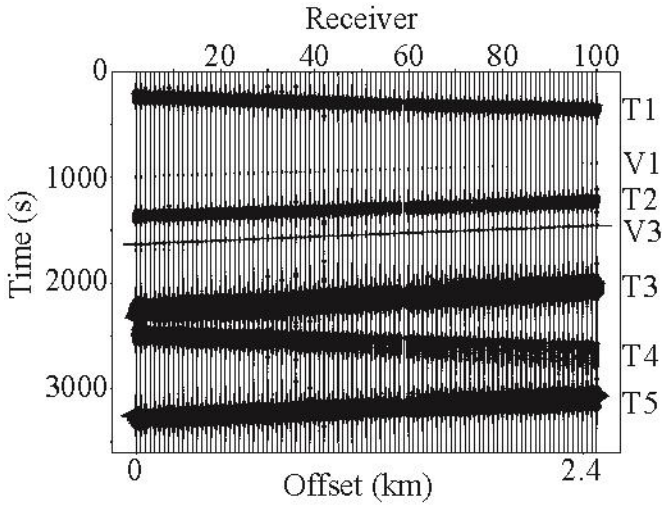

Figure 3.2: Raw seismograms of the 17th hour of recording. Trains (T) and vehicles (V) are visible on the record. Events that dip down to the right are moving towards the southeast (e.g. T1), events that dip down to the left are moving towards the northwest (e.g. T5). Vehicle 1 is moving on the gravel road closer to the railway, vehicle 2 is moving along the gravel road next to the array (see Fig. 3.1).

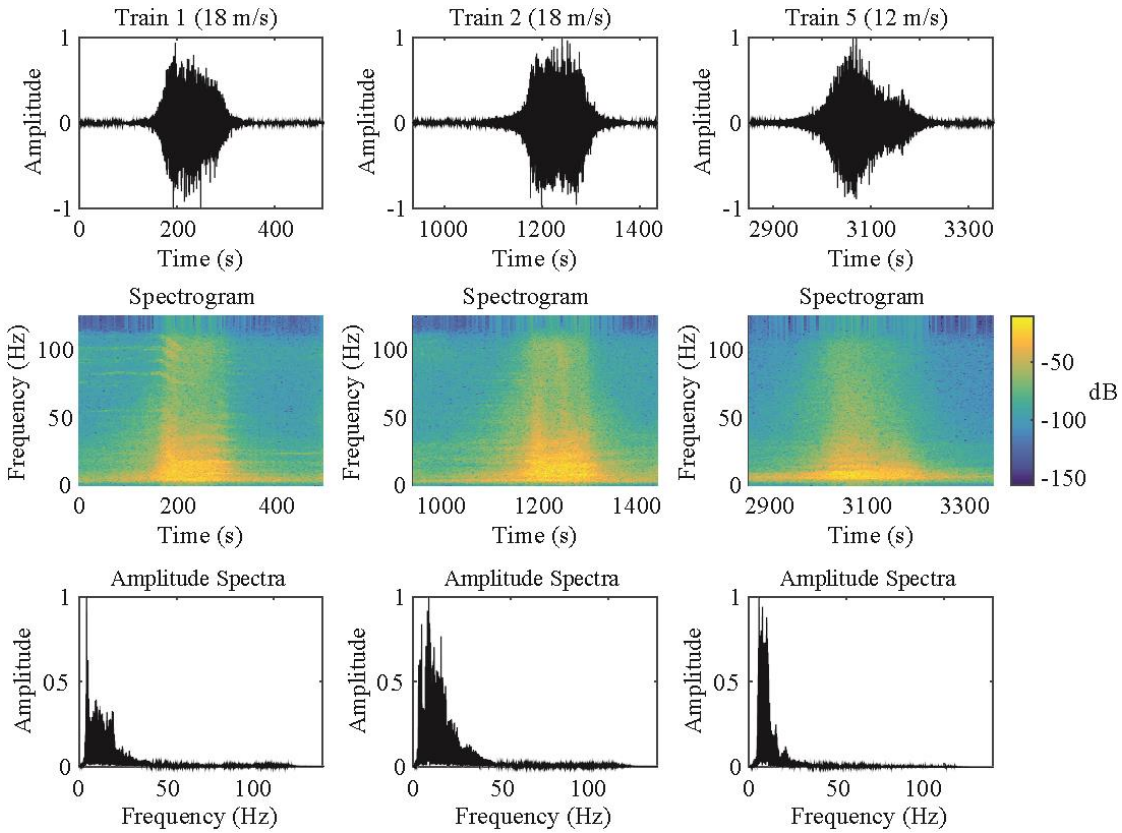

Figure 3.3: Fourier analysis of the train records shown in Fig. 3.2. Top row: master trace for train signals T1, T2 and T5, obtained by time-shifting the signals using the average velocity of the train and summing all traces. Middle row: spectrogram of master trace. Bottom row: amplitude spectra of master trace.

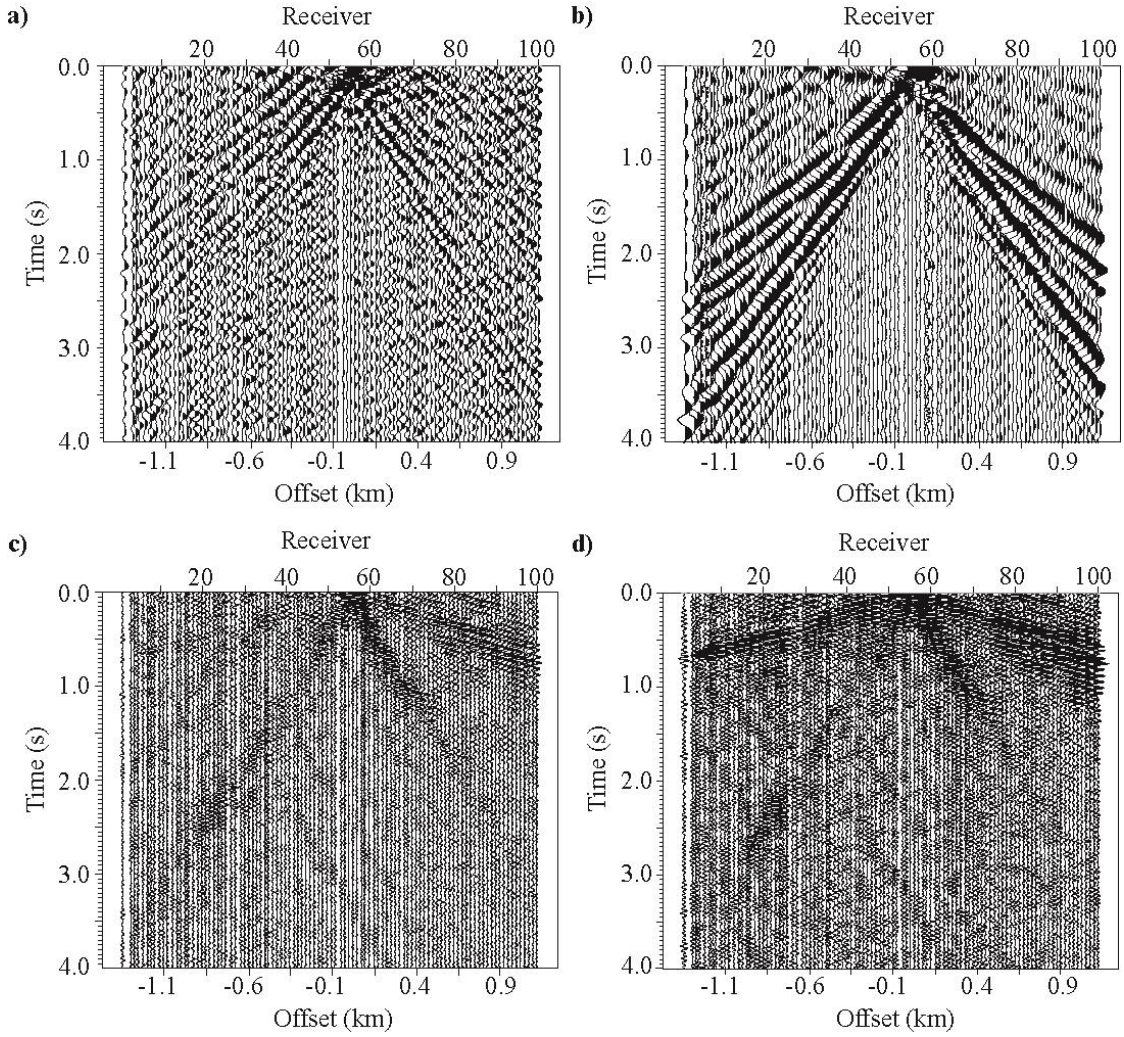

Figure 3.4: Virtual-shot gathers generated by cross-correlation, rms scaling to equalize the amplitude among all panels and stacking. Various pre-processing steps were applied. Only positive correlation lags are shown. Different panels illustrate the results of pre-processing with (a) rms amplitude scaling with a window of 1 hr, then rms panel-to-panel normalization (b) one-bit amplitude normalization, (c) rms amplitude scaling with a window of 50 s, then rms panel-to-panel normalization and bandpass filtering (16–100 Hz), (d) bandpass filtering (16–100 Hz) and one-bit amplitude normalization. The virtual source in each case is at receiver 55.

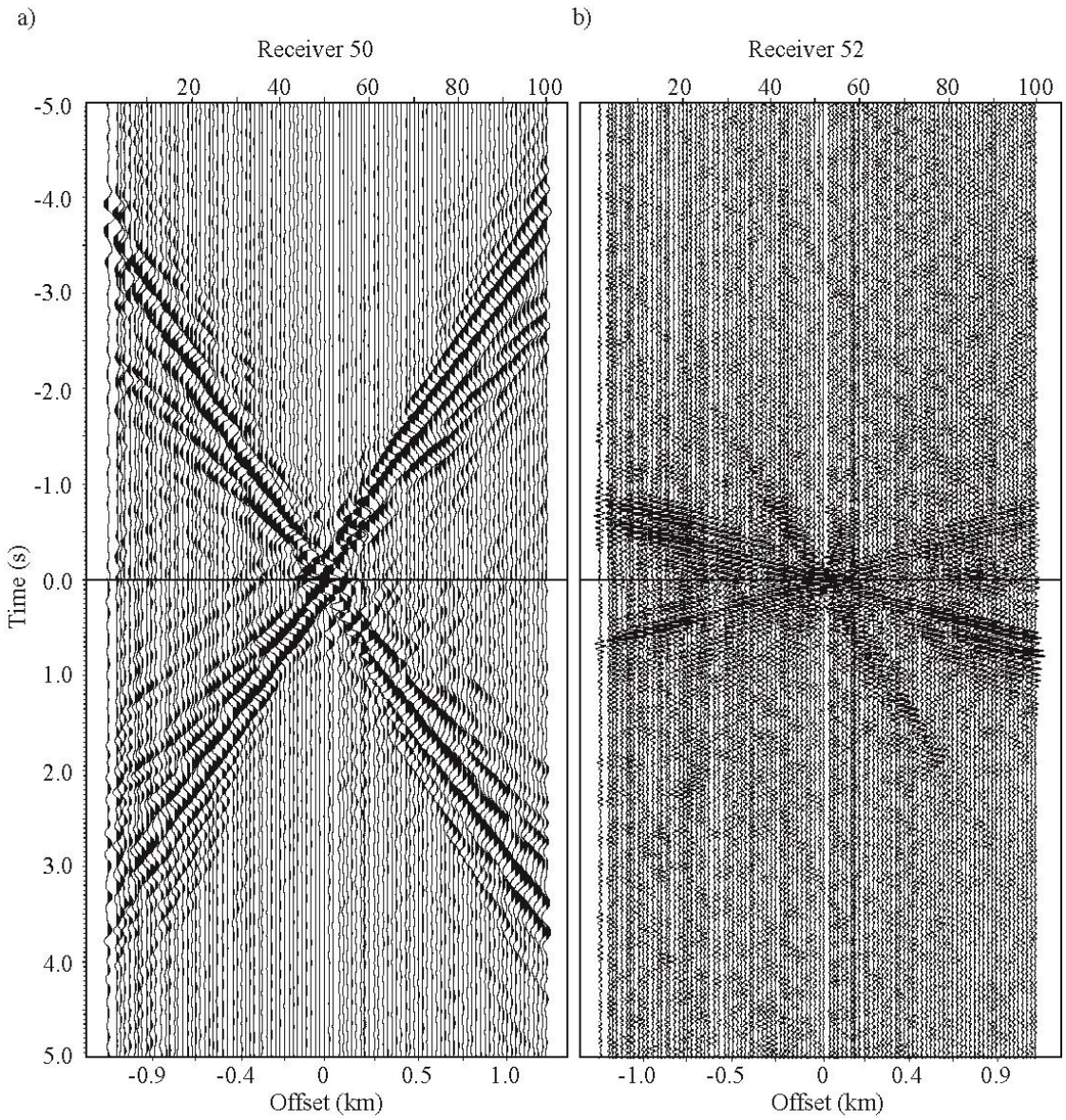

Figure 3.5: Positive and negative lags of the cross-correlation for (a) the source at station 50, with one-bit normalization pre-processing, and for (b) the source at station 52, with bandpass (16–100 Hz) and one-bit normalization pre-processing.

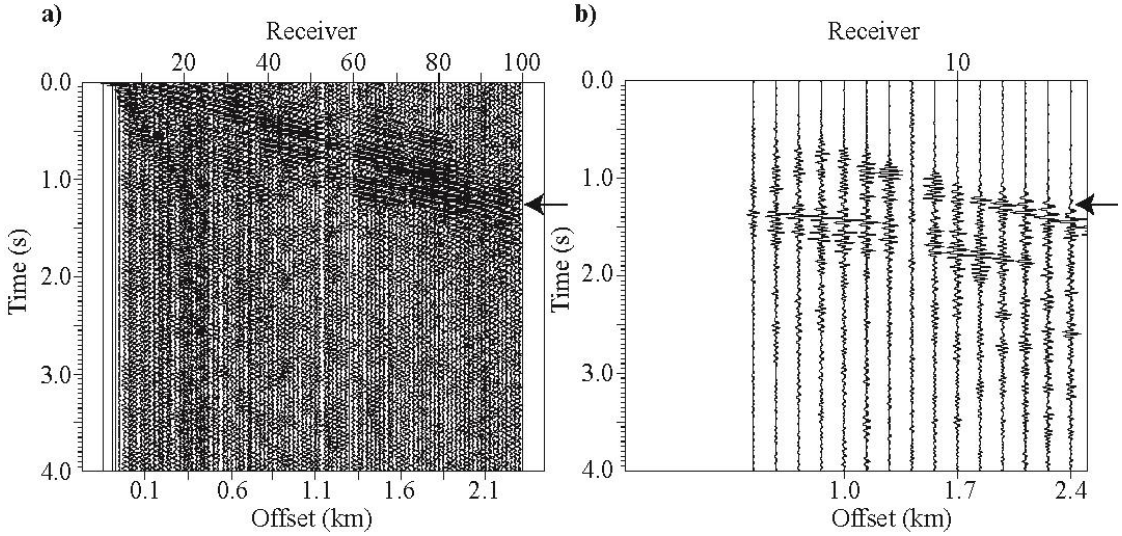

Figure 3.6: (a) Virtual-shot gather (positive lags) at receiver 5. (b) COCORP line 1-A real shot-gather (vibration point 105) presumed to sample similar geology to that beneath the Belen array. Only 15 traces of the COCORP data are shown to match the aperture of the Belen railroad array (ca. 2.4 km). The apparent velocity of the first arrivals (arrows) in both cases is ~2100 m s−1. The curved second arrival on the COCORP data is a reflection at ~1200 m depth. Hyperbolic events at large offsets on the virtual-shot gathers (e.g. Fig. 3.6a) are here interpreted as reflected P waves as well (see Fig. 3.7).

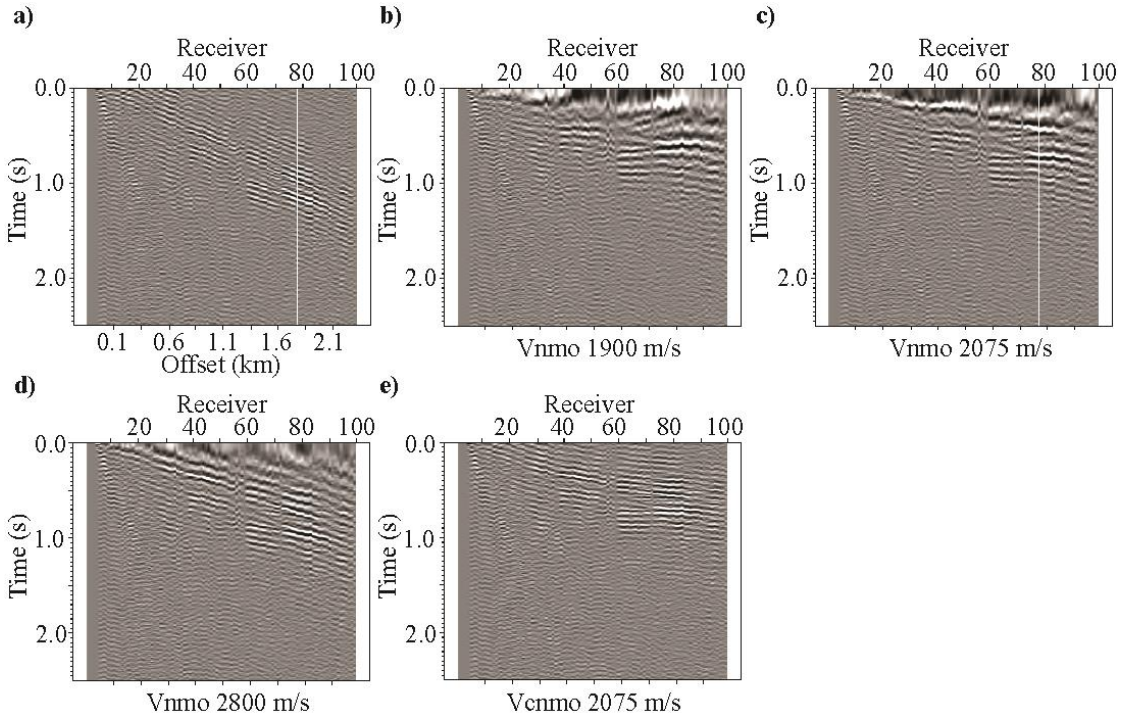

Figure 3.7: Virtual-shot gather (positive lags) for receiver 5 with (a) no NMO correction, (b) Vnmo = 1900 m s−1, (c) Vnmo = 2075 m s−1 and (d) Vnmo = 2800 m

s−1. Because of the severe NMO stretch at large offsets for shallow events we have used the constant normal moveout [*Shatilo and Aminzadeh*, 2000] correction for V = 2075 m s−1 in (e).

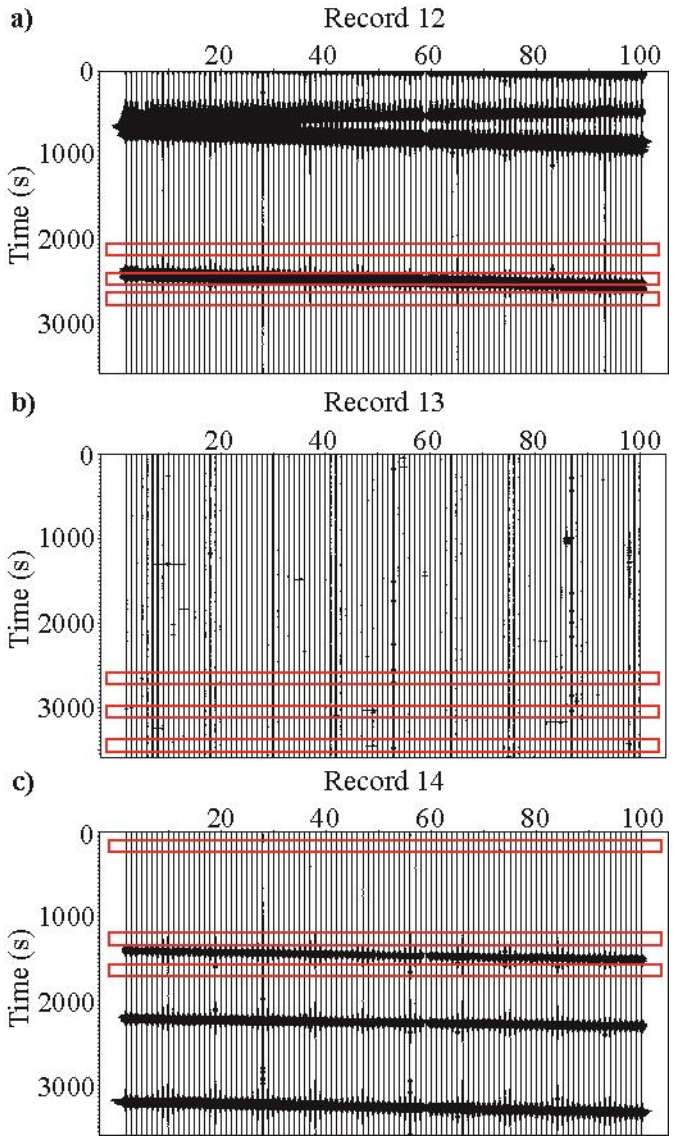

Figure 3.8: Three-hour-long records normalized by the max amplitude in record 12, each with three 100 s windows (red rectangles). The records are the (a) 12th, (b) 13th and (c) 14th hour of recording. Record 13 is the only hour in the entire data set that did not appear to contain any train or vehicle signals.

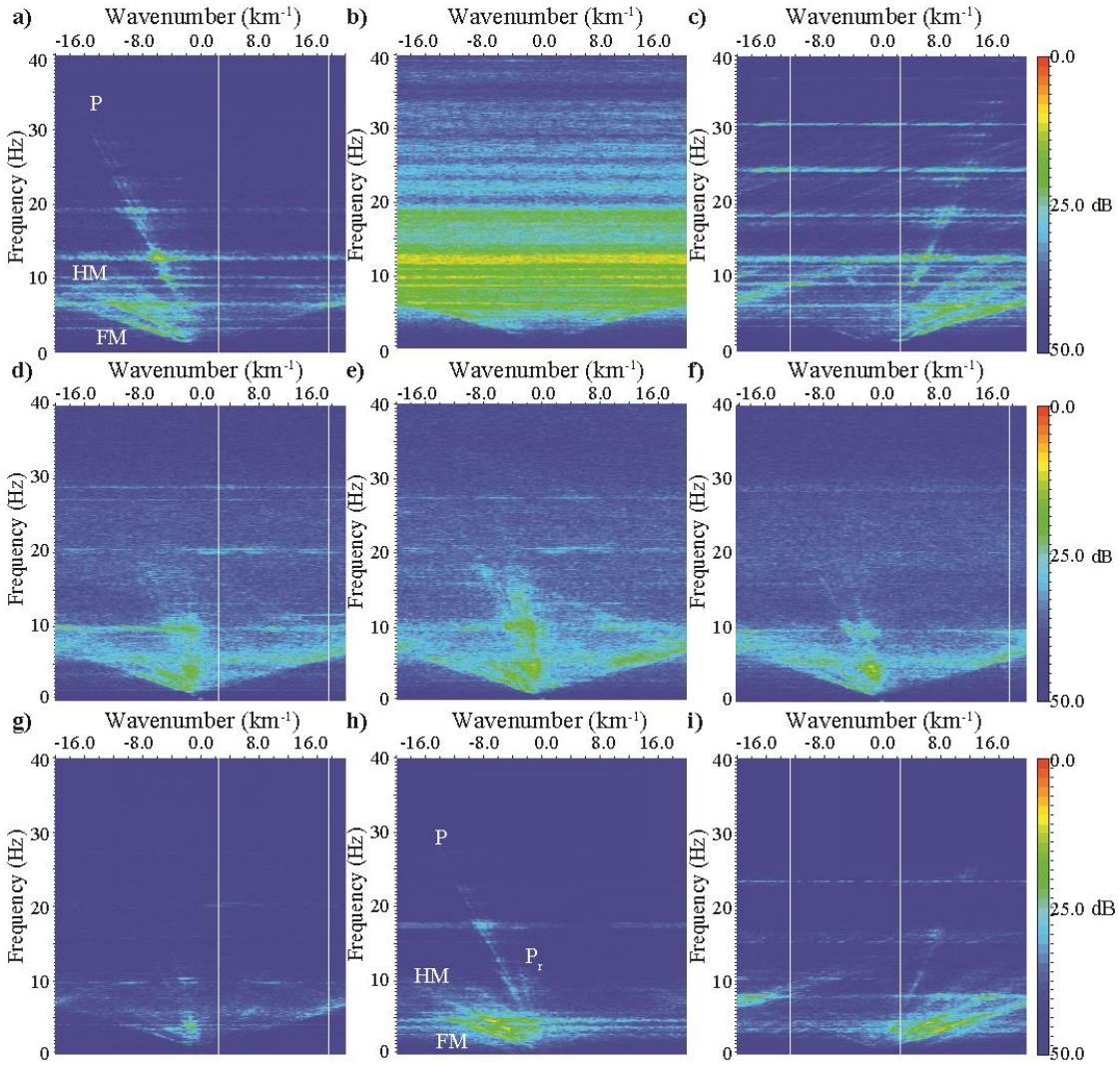

Figure 3.9: Frequency–wavenumber analysis of Fig. 3.8. f–k analysis of window (a) 2150–2250 s, (b) 2430–2530 s, (c) 2620–2720 s, in record 12. f–k analysis of window (d) 2600–2700 s, (e) 3000–3100 s, (f) 3400–3500 s, in record 13. f–k analysis of window (g) 100–200 s, (h) 1200–1300 s, (i) 1550–1650 s, in record 14. P, FM and HM mark the direct P-wave, and the fundamental and higher mode surface waves, respectively. Pr marks linear arrivals which we interpret as energy (head waves) refracted from deeper interfaces. See the text for discussion.

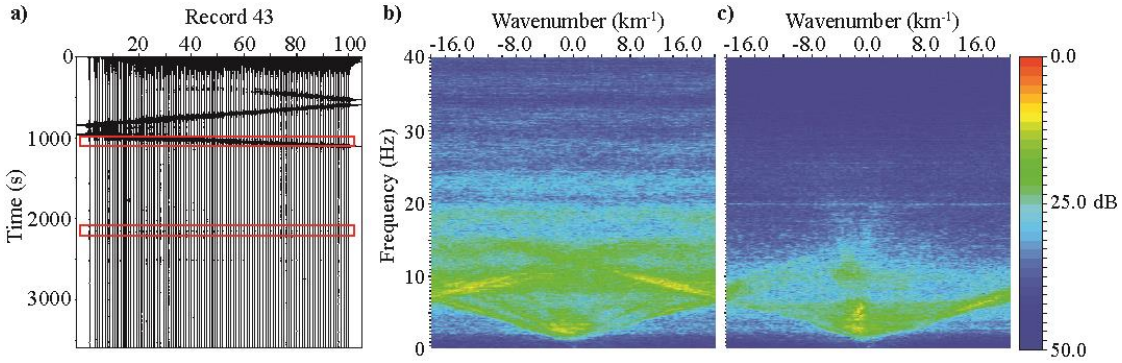

Figure 3.10: Frequency–wavenumber analysis of strong sources other than trains. (a) Seismograms of 43rd hour showing part of a train signal at the start of the record, followed by three car signals and what is interpreted as wind gusts. f–k analysis of window (b) 990–1090 s containing a car signal, and of window (c) 2100–2200 s containing a wind gust.

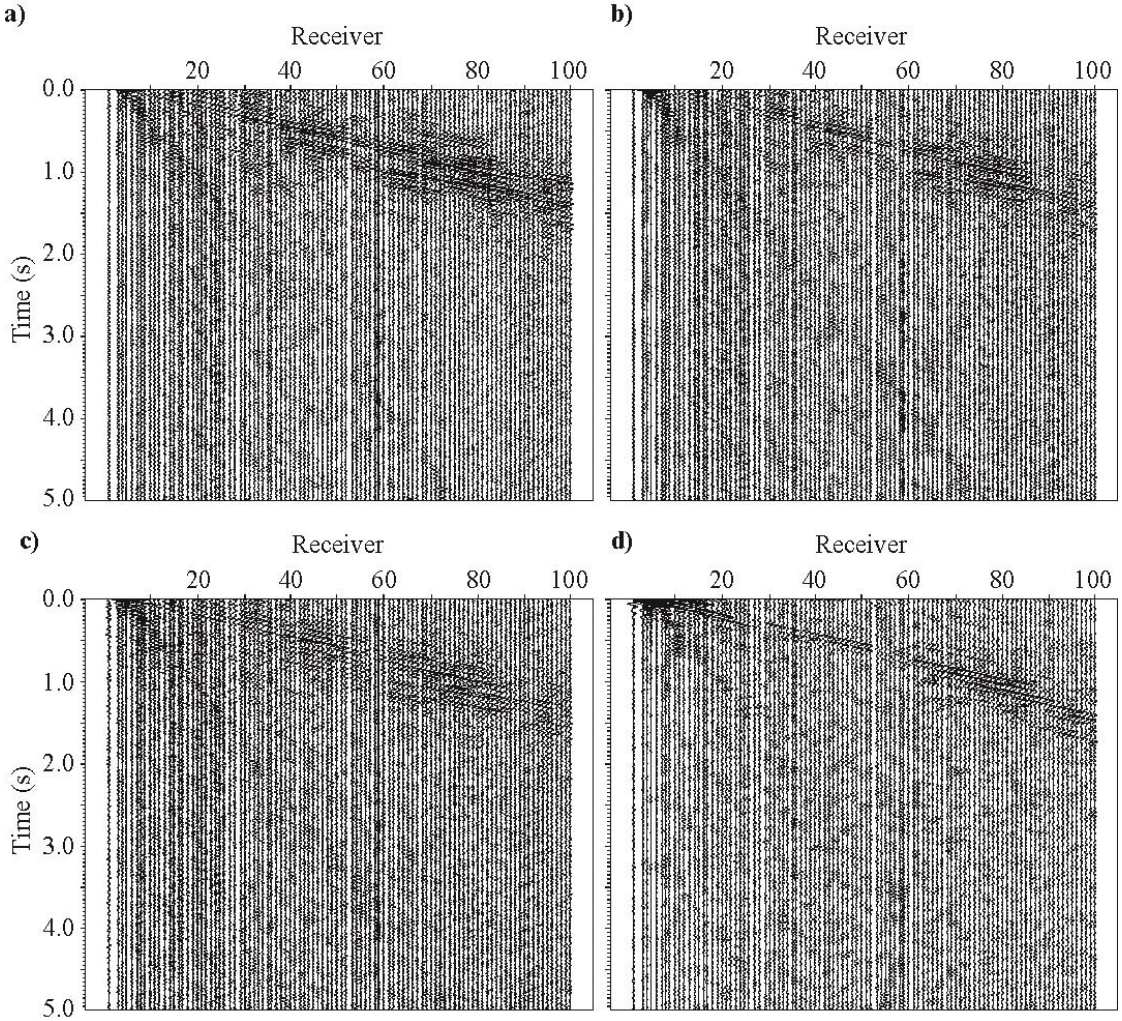

Figure 3.11: Comparison of several pre-processing routines guided by the f–k analysis. (a) Brute correlation using the same parameters as in Fig. 3.4(d). (b) rms amplitude scaling with a window of 50 s, then rms panel-to-panel normalization, followed by a

bandpass filtering (16–100 Hz) and muting of vehicles, wind gusts and broadside train energy prior to correlation. (c) Same pre-processing as in (b) with an added notch filter to remove a monotonic 20 Hz signal (see the text for discussion). (d) rms amplitude scaling with a window of 50 s, then rms panel-to-panel normalization, followed by an f–k filter to remove surface wave energy before correlation.

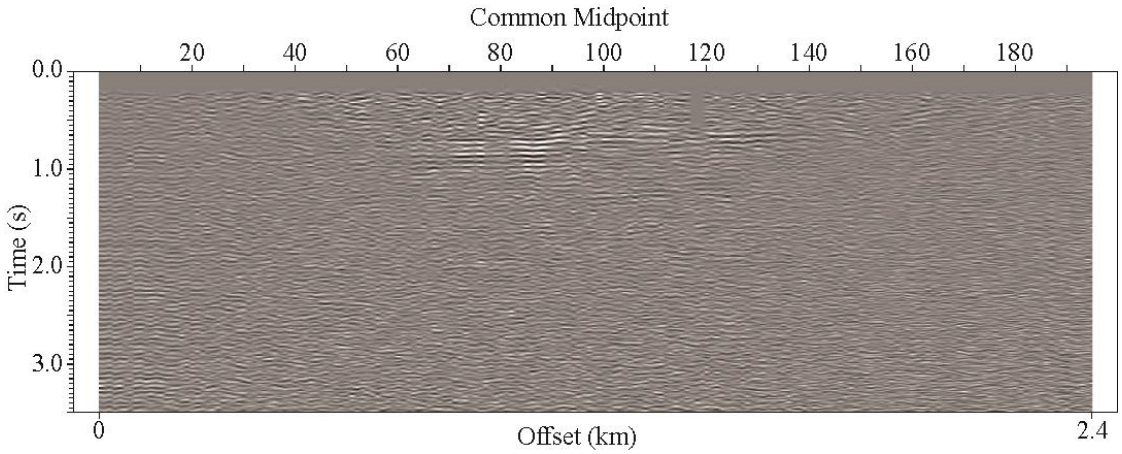

Figure 3.12: Common midpoint stack of virtual CMP gathers. The coherent event at 0.72 s twt (ca. 750 m below the surface) is interpreted as the base of the Tertiary sedimentary section.

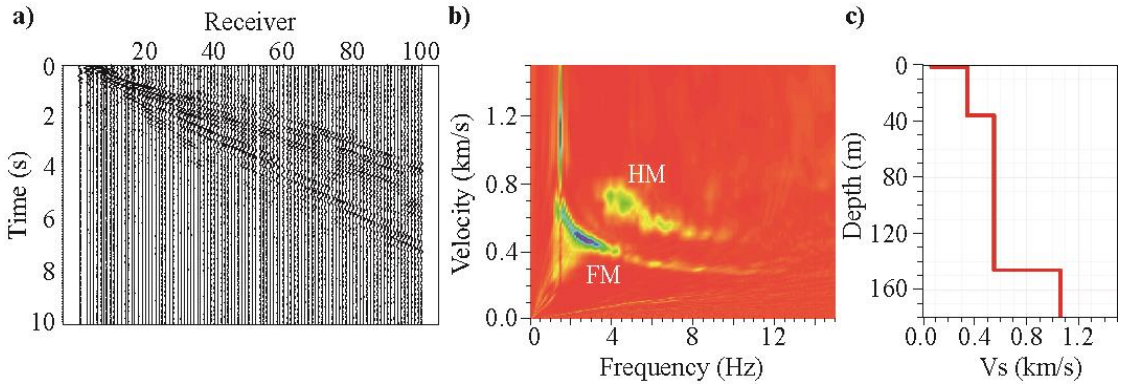

Figure 3.13: (a) Virtual-shot gather with station 5 as the source. (b) Dispersion curve for the virtual-shot gather at receiver 5, with the fundamental mode (FM) and a higher mode (HM) labeled. (c) 1-D shear wave velocity model obtained from the inversion in the frequency range 0–8 Hz of the dispersion curve from the fundamental mode.

REFERENCES

Ardhuin, F., L. Gualtieri, and E. Stutzmann (2015), How ocean waves rock the Earth: Two mechanisms explain microseisms with periods 3 to 300 s, *Geophys. Res. Lett.*, *42*(3), 2014GL062782, doi: 10.1002/2014GL062782.

Bakulin, A., and R. Calvert (2004), Virtual Source: New Method For Imaging And 4D Below Complex Overburden, Society of Exploration Geophysicists.

Balch, R. S., H. E. Hartse, A. R. Sanford, and K. Lin (1997), A new map of the geographic extent of the Socorro mid-crustal magma body, *Bull. Seismol. Soc. Am.*, *87*(1), 174–182.

Baskir, E., and C. E. Weller (1975), Sourceless reflection seismic exploration, *GEOPHYSICS*, *40*(1), 158–159.

Behm, M., and R. Snieder (2013), Love waves from local traffic noise interferometry, *Lead. Edge*, *32*(6), 628–632, doi:10.1190/tle32060628.1.

Behm, M., G. M. Leahy, and R. Snieder (2014), Retrieval of local surface wave velocities from traffic noise – an example from the La Barge basin (Wyoming), *Geophys. Prospect.*, *62*(2), 223–243, doi:10.1111/1365-2478.12080.

Bensen, G. D., M. H. Ritzwoller, M. P. Barmin, A. L. Levshin, F. Lin, M. P. Moschetti, N. M. Shapiro, and Y. Yang (2007), Processing seismic ambient noise data to obtain reliable broad-band surface wave dispersion measurements, *Geophys. J. Int.*, *169*(3), 1239–1260, doi:10.1111/j.1365-246X.2007.03374.x.

Bond, F. E., and C. R. Cahn (1958), On the sampling the zeros of bandwidth limited signals, *IRE Trans. Inf. Theory*, *4*(3), 110–113, doi:10.1109/TIT.1958.1057457.

Bonnefoy-Claudet, S., F. Cotton, and P.-Y. Bard (2006), The nature of noise wavefield and its applications for site effects studies: A literature review, *Earth-Sci. Rev.*, *79*(3–4), 205–227, doi:10.1016/j.earscirev.2006.07.004.

Brenguier, F., N. M. Shapiro, M. Campillo, A. Nercessian, and V. Ferrazzini (2007), 3-D surface wave tomography of the Piton de la Fournaise volcano using seismic noise correlations, *Geophys. Res. Lett.*, *34*(2), L02305, doi:10.1029/2006GL028586.

Brown, L. D., P. A. Krumhansl, C. E. Chapin, A. R. Sanford, F. A. Cook, S. Kaufman, J. E. Oliver, and F. S. Schilt (1979), COCORP seismic reflection studies of the Rio Grande rift, *Rio Gd. Rift Tecton. Magmat.*, 169–184.

Claerbout, J. F. (1968), Synthesis of a layered medium from its acoustic transmission response, *Geophysics*, *33*, 264.

Cole, S. (1995), Passive seismic and drill-bit experiments using 2-D arrays, PhD Thesis, Stanford University, Palo Alto, USA.

Cupillard, P., L. Stehly, and B. Romanowicz (2011), The one-bit noise correlation: a theory based on the concepts of coherent and incoherent noise, *Geophys. J. Int.*, *184*(3), 1397–1414.

Decker, E. R., and S. B. Smithson (1975), Heat flow and gravity interpretation across the Rio Grande rift in southern New Mexico and west Texas, *J. Geophys. Res.*, *80*(17), 2542–2552.

Draganov, D., K. Wapenaar, and J. Thorbecke (2006), Seismic interferometry: Reconstructing the earth's reflection response, *Geophysics*, *71*(4), SI61–SI70.

Draganov, D., K. Wapenaar, W. Mulder, J. Singer, and A. Verdel (2007), Retrieval of reflections from seismic background-noise measurements, *Geophys. Res. Lett.*, *34*(L04305).

Draganov, D., X. Campman, J. Thorbecke, A. Verdel, and K. Wapenaar (2009), Reflection images from ambient seismic noise, *Geophysics*, *74*, A63.

Duvall, T. L., S. M. Jeffferies, J. W. Harvey, and M. A. Pomerantz (1993), Time–distance helioseismology, *Nature*, *362*(6419), 430–432, doi: 10.1038/362430a0.

Ekström, G. (2001), Time domain analysis of Earth's long-period background seismic radiation, *J. Geophys. Res. Solid Earth 1978–2012*, *106*(B11), 26483–26493.

Forghani, F., and R. Snieder (2010), Underestimation of body waves and feasibility of surface-wave reconstruction by seismic interferometry, *Lead. Edge*, *29*(7), 790–794.

Frailey, F. W. (2007), Birthplace of the Transcon, *Trains Mag.*, (April).

Grant, F. S., and G. F. West (1965), *Interpretation theory in applied geophysics*, McGraw-Hill Book.

Halliday, D., and A. Curtis (2008), Seismic interferometry, surface waves and source distribution, *Geophys. J. Int.*, *175*(3), 1067–1087.

Halliday, D., A. Curtis, and E. Kragh (2008), Seismic surface waves in a suburban environment: Active and passive interferometric methods, *Lead. Edge*, *27*(2), 210–218.

Hasselmann, K. (1963), A statistical analysis of the generation of microseisms, *Rev. Geophys.*, *1*(2), 177–210.

Haubrich, R. A., W. H. Munk, and F. E. Snodgrass (1963), Comparative spectra of microseisms and swell, *Bull. Seismol. Soc. Am.*, *53*(1), 27–37.

Kang, T.-S., and J. S. Shin (2006), Surface-wave tomography from ambient seismic noise of accelerograph networks in southern Korea, *Geophys. Res. Lett.*, *33*(17), L17303, doi: 10.1029/2006GL027044.

Kimman, W. P., and J. Trampert (2010), Approximations in seismic interferometry and their effects on surface waves, *Geophys. J. Int.*, *182*(1), 461–476.

Koper, K. D., K. Seats, and H. Benz (2010), On the composition of Earth's short-period seismic noise field, *Bull. Seismol. Soc. Am.*, *100*(2), 606–617.

Lin, F.-C., V. C. Tsai, B. Schmandt, Z. Duputel, and Z. Zhan (2013a), Extracting seismic core phases with array interferometry, *Geophys. Res. Lett.*, *40*(6), 1049–1053.

Lin, F.-C., D. Li, R. W. Clayton, and D. Hollis (2013b), High-resolution 3D shallow crustal structure in Long Beach, California: Application of ambient noise tomography on a dense seismic array, *Geophysics*, *78*(4), Q45–Q56.

Lobkis, O. I., and R. L. Weaver (2001), On the emergence of the Green's function in the correlations of a diffuse field, *J. Acoust. Soc. Am.*, *110*, 3011.

Longuet-Higgins, M. S. (1950), A Theory of the Origin of Microseisms, *Philos. Trans. R. Soc. Lond. Math. Phys. Eng. Sci.*, *243*(857), 1–35, doi:10.1098/rsta.1950.0012.

Matsuoka, T., K. Shiraishi, K. Onishi, and T. Aizawa (2006), Application of seismic interferometry to subsurface imaging (1), in *Proc. of the 10th International Symp. on Recent Advanced in Exploration Geophysics (RAEG2006)*, pp. 35–38.

Mikesell, D., K. van Wijk, A. Calvert, and M. Haney (2009), The virtual refraction: Useful spurious energy in seismic interferometry, *GEOPHYSICS*, *74*(3), A13–A17, doi:10.1190/1.3095659.

Miyazawa, M., R. Snieder, and A. Venkataraman (2008), Application of seismic interferometry to extract P- and S-wave propagation and observation of shear-wave splitting from noise data at Cold Lake, Alberta, Canada, *GEOPHYSICS*, *73*(4), D35–D40, doi:10.1190/1.2937172.

Nakata, N., R. Snieder, T. Tsuji, K. Larner, and T. Matsuoka (2011), Shear wave imaging from traffic noise using seismic interferometry by cross-coherence, *Geophysics*, *76*(6), SA97–SA106.

Nishida, K., N. Kobayashi, and Y. Fukao (2000), Resonant oscillations between the solid earth and the atmosphere, *Science*, *287*(5461), 2244–2246.

Nishida, K., J.-P. Montagner, and H. Kawakatsu (2009), Global surface wave tomography using seismic hum, *Science*, *326*(5949), 112–112.

Poletto, F. B., and F. Miranda (2004), *Seismic while drilling: Fundamentals of drill-bit seismic for exploration*, Elsevier.

Poli, P., H. A. Pedersen, and M. Campillo (2011), Emergence of body waves from cross-correlation of short period seismic noise, *Geophys. J. Int.*, *188*(2), 549–558, doi:10.1111/j.1365-246X.2011.05271.x.

Ramberg, I. B., and S. B. Smithson (1975), Gridded fault patterns in a late Cenozoic and a Paleozoic continental rift, *Geology*, *3*(4), 201–205.

Rector III, J. W., and B. P. Marion (1991), The use of drill-bit energy as a downhole seismic source, *Geophysics*, *56*(5), 628–634.

Roux, P., K. G. Sabra, P. Gerstoft, W. A. Kuperman, and M. C. Fehler (2005), P-waves from cross-correlation of seismic noise, *Geophys Res Lett*, *32*, L19303.

Ruigrok, E., X. Campman, D. Draganov, and K. Wapenaar (2010), High-resolution lithospheric imaging with seismic interferometry, *Geophys. J. Int.*, *183*(1), 339–357, doi:10.1111/j.1365-246X.2010.04724.x.

Ruigrok, E., X. Campman, and K. Wapenaar (2011), Extraction of P-wave reflections from microseisms, *Comptes Rendus Geosci.*, *343*(8–9), 512–525, doi:10.1016/j.crte.2011.02.006.

Russell, L. R., and S. Snelson (1994), Structure and tectonics of the Albuquerque Basin segment of the Rio Grande rift: Insights from reflection seismic data, *Geol. Soc. Am. Spec. Pap.*, *291*, 83–112.

Ryberg, T. (2011), Body wave observations from cross-correlations of ambient seismic noise: A case study from the Karoo, RSA, *Geophys. Res. Lett.*, *38*(13), L13311.

Sanford, A. R., and L. T. Long (1965), Microearthquake crustal reflections, Socorro, New Mexico, *Bull. Seismol. Soc. Am.*, *55*(3), 579–586.

Schmucker, U. (1970), *Anomalies of geomagnetic variations in the southwestern United States*, University of California Press Berkeley.

Schuster, G. (2001), Theory of daylight/interferometric imaging: tutorial, *Ext. Abstr. 63rd Mtg Eur Assoc Geosc Eng*.

Schuster, G. T., J. Yu, J. Sheng, and J. Rickett (2004), Interferometric/daylight seismic imaging, *Geophys. J. Int.*, *157*(2), 838–852, doi:10.1111/j.1365-246X.2004.02251.x.

Shapiro, N. M., M. Campillo, L. Stehly, and M. H. Ritzwoller (2005), High-resolution surface-wave tomography from ambient seismic noise, *Science*, *307*(5715), 1615.

Shatilo, A., and F. Aminzadeh (2000), Constant normal-moveout (CNMO) correction: a technique and test results, *Geophys. Prospect.*, *48*(3), 473–488.

Shiraishi, K., M. Tanaka, K. Onishi, T. Matsuoka, and S. Yamaguchi (2006), Application of seismic interferometry to subsurface imaging (2), in *The 10th International Symposium on Recent Advances in Exploration Geophysics (RAEG 2006)*.

Snieder, R. (2004), Extracting the Green's function from the correlation of coda waves: A derivation based on stationary phase, *Phys. Rev. E*, *69*(4), 46610.

Snieder, R., A. Grêt, H. Douma, and J. Scales (2002), Coda wave interferometry for estimating nonlinear behavior in seismic velocity, *Science*, *295*(5563), 2253–2255.

Tanimoto, T. (2001), Continuous free oscillations: atmosphere-solid earth coupling, *Annu. Rev. Earth Planet. Sci.*, *29*(1), 563–584.

Toksöz, M. N., and R. T. Lacoss (1968), Microseisms: Mode Structure and Sources, *Science*, *159*(3817), 872–873.

Traer, J., and P. Gerstoft (2014), A unified theory of microseisms and hum, *J. Geophys. Res. Solid Earth*, *119*(4), 3317–3339, doi:10.1002/2013JB010504.

Wapenaar, K. (2003), Synthesis of an inhomogeneous medium from its acoustic transmission response, *GEOPHYSICS*, *68*(5), 1756–1759, doi:10.1190/1.1620649.

Wapenaar, K. (2004), Retrieving the elastodynamic Green's function of an arbitrary inhomogeneous medium by cross correlation, *Phys. Rev. Lett.*, *93*(25), 254301.

Wapenaar, K., and J. Fokkema (2006), Green's function representations for seismic interferometry, *GEOPHYSICS*, *71*(4), SI33-SI46, doi:10.1190/1.2213955.

Wathelet, M. (2008), An improved neighborhood algorithm: parameter conditions and dynamic scaling, *Geophys. Res. Lett.*, *35*(9), L09301.

Wathelet, M., D. Jongmans, and M. Ohrnberger (2004), Surface wave inversion using a direct search algorithm and its application to ambient vibration measurements, *Surf. Geophys.*, *2*(4), 211–221.

Weaver, R. L., and O. I. Lobkis (2001), Ultrasonics without a source: Thermal fluctuation correlations at MHz frequencies, *Phys. Rev. Lett.*, *87*(13), 134301.

Webb, S. C. (2007), The Earth's "hum" is driven by ocean waves over the continental shelves, *Nature*, *445*(7129), 754–756.

Webb, S. C. (2008), The Earth's hum: the excitation of Earth normal modes by ocean waves, *Geophys. J. Int.*, *174*(2), 542–566.

Yang, Y., M. H. Ritzwoller, A. L. Levshin, and N. M. Shapiro (2007), Ambient noise Rayleigh wave tomography across Europe, *Geophys. J. Int.*, *168*(1), 259–274.

Yao, H., R. D. van Der Hilst, and V. Maarten (2006), Surface-wave array tomography in SE Tibet from ambient seismic noise and two-station analysis—I. Phase velocity maps, *Geophys. J. Int.*, *166*(2), 732–744.

Yilmaz, Ö. (2001), *Seismic data analysis*, Society of Exploration Geophysicists Tulsa.

Zhan, Z., S. Ni, D. V. Helmberger, and R. W. Clayton (2010), Retrieval of Moho-reflected shear wave arrivals from ambient seismic noise, *Geophys. J. Int.*, *182*(1), 408–420, doi:10.1111/j.1365-246X.2010.04625.x.

CHAPTER 4

AFTERSHOCK IMAGING WITH DENSE ARRAYS (AIDA) FOLLOWING THE Mw 4.0 WATERBORO EARTHQUAKE OF OCTOBER 16, 2012 MAINE U.S.A.

4.1 Abstract

Arrays of highly portable, exploration style seismographs were deployed following the MW 4.0 Waterboro, Maine earthquake of October 16, 2012 with the goal of improving hypocenter locations and source mechanisms of aftershocks, lowering the detection threshold for such aftershocks, and using the aftershocks as sources to image subsurface structure in the hypocentral volume. Informed by the AIDA experience following the Mineral, Virginia earthquake of August 2011, the Maine deployment consisted of three complementary arrays totaling 110 stations: one for event detection and location, another for structural imaging and a third for measuring regional attenuation. Although the arrays operated from day 3 through day 10 following the mainshock, only one aftershock was detected by the 43 stations that had been deployed at the time of the event. This aftershock was located at a focal depth of 6.9 ± 0.15 km, with a horizontal uncertainty of ~ 0.15 km. Although the strike-slip focal mechanism for this aftershock differs from the thrust mechanism of the mainshock, both share an EW maximum stress direction. Recordings of the aftershock from the high-density portion of the deployment show possible upper and lower crustal reflections that we attempt to image using Vertical Seismic Profiling (VSP) methods. However the lack of redundant sources and the limited areal extend of the imaging arrays hinders any useful interpretation of the nature of the crustal reflections. Based

The material in Chapter 4 has been published under Quiros et al., Aftershock Imaging with Dense Arrays (AIDA) Following the Mw 4.0 Waterboro Earthquake of 16 October 2012 Maine, U.S.A., *Seismo. Res. Let.* **86**, 3 May/June 2015

on comparison with the Virginia experiment, where numerous aftershocks were recorded, and from examining the signal-to-noise ratio of the single aftershock recorded, we believe the AIDA Maine deployment should have detected any aftershocks greater than magnitude mb ~ -2.5. That only one aftershock was detected supports the observation that earthquakes in some intraplate areas are notable for their lack of aftershock activity down to this level.

4.2 Introduction

On October 16, 2012 at approximately 7:12 p.m. (EST) a magnitude MW 4.0 earthquake struck near Waterboro, Maine [*USGS*, 2012]. Following this event a suite of local arrays were deployed around the epicentral region (Fig. 4.1). These arrays differ from conventional aftershock arrays in that large numbers of highly portable seismographs (Ref Tek RT 125A Texans coupled with 4.5 Hz geophones), originally designed for controlled source seismic reflection and refraction experiments, were deployed at relatively close spacing (i.e., ca 200 m) as part of the aftershock monitoring effort. This deployment was designed based on experience with a similarly dense deployment (labeled as AIDA for Aftershock Imaging with Dense Arrays) following the MW 5.8, 2011 Mineral, Virginia earthquake [*Brown et al.*, 2011; *Davenport et al.*, 2014].

4.3 Deployment

The Maine AIDA deployment (Fig. 4.1a) consisted of three complementary arrays totaling 110 seismic stations. The first array deployed was designed to encompass the potential aftershock zone, thus providing adequate azimuthal coverage for accurate event location. It consisted of 20 stations spaced approximately 5 km

apart in a grid (Fig. 4.1a), a layout similar to a conventional, relatively well-instrumented aftershock array [e.g. *Bounif et al.*, 2004; *Kim and Chapman*, 2005; *Huang et al.*, 2008]. The second array, a High Density Array (HDA) consisted of a box grid of 60 stations spaced very close together (i.e., ca 200 m) whose purpose was to record aftershock signals in relatively unaliased form for structural imaging (Fig. 4.1a). These two arrays used vertical component, 4.5 Hz geophones (Geospace GS-11D) and a single recorder (Ref Tek RT 125A Texan) sampling at 100 samples/sec. The third array was a profile through the area with 28 three-component (3C) recording stations (4.5 Hz Sercel L-28-3D geophone coupled with 3 Texans programmed to each record at a rate of 100 Hz) spaced at 1 km to allow measurement of the regional attenuation of seismic energy (Fig. 4.1a). In many respects the Maine AIDA deployment, like the Virginia antecedent, was a small scale warm up for the much more ambitious requirements of a dense 2D grid needed for true 3D aftershock imaging.

The Maine AIDA experiment recorded continuously for seven days (October 19-October 25, 2012), with the deployment for all three arrays finalized on October 21st. Although the arrays operated from day 3 through day 10 following the mainshock, only one aftershock was detected, occurring on October 20 at 07:46:35.06 ± 0.02 s UTC. At the time of the aftershock 43 AIDA stations had been deployed (Fig. 4.1b).

In addition to the AIDA experiment, Weston Observatory of Boston College deployed three seismic stations for aftershock monitoring (Fig. 4.1b). Each of the Weston Observatory portable seismic stations consisted of a Guralp CMG-40T

seismometer and a Ref Tek 130 digitizer, with a sampling rate of 40 samples/sec. These local Weston Observatory stations were run from October 17 until November 12, but only detected one aftershock, that on October 20.

Fig. 4.2 shows the AIDA vertical component seismograms of the only aftershock recorded, with P and S phases marked. Since the 3C array and the HDA 2 were not in place at the time of the event, those recordings are not relevant to the analysis reported in this paper.

4.4 Mainshock and aftershock parameters

The MW 4.0 Waterboro, ME earthquake's epicenter was reported by the Weston Observatory to be at 43.60 ± 0.007 º N, 70.65 ± 0.007 º W. This location used 221 stations of which only one was within 100 km of the epicenter (i.e., Franklin Falls dam station FFD, 82.4 km from epicenter). The preferred focal depth for this event is 7.0 km, obtained from a regional moment tensor inversion [*USGS*, 2012]. The focal mechanism determined by the *USGS*, [2012] was that of a reverse-faulting event striking NNW-SSE with a minor strike-slip component, consistent with the region's EW oriented maximum horizontal stress direction [*Ebel and Kafka*, 1991; *Zoback*, 1992]. Unfortunately, the aftershock that is the focus of this paper was not recorded by the New England Seismic Network (NESM) operated by Weston Observatory, ruling out the application of relative location techniques that would allow us to improve the mainshock location. Although the epicenter of the mainshock lies near the surface trace of a thrust fault mapped by *Osberg et al.*, [1985], a direct relationship of the earthquake to the fault is problematic given the depth of the event and the dip of the focal mechanism.

One of the objectives of this AIDA experiment was to assess the improvement in hypocenter location that can be attained from dense recording compared with more traditional aftershock studies. Here we located the aftershock using various subsets of the AIDA Maine deployment: (1) all 43 AIDA stations that recorded the event (Fig. 4.1b), (2) the AIDA sparse (location) array only (diamonds in Fig. 4.1b), (3) a subset of AIDA location stations (circled diamonds in Fig. 4.1b), and (4) all 43 AIDA stations and the three Weston stations (Fig. 4.1b). Variations 2 and 3 are analogous to traditional aftershock deployments, whereas variations 1 and 4 include the high-density array (i.e., HDA 1).

All inversions for the hypocenter were done using the HYPOSAT earthquake location program [*Schweitzer*, 2001] and the regional P-wave velocity model of [*Luetgert et al.*, 1987]. A VP/VS ratio of 1.73 [*Luetgert et al.*, 1987] was used to provide the S-wave velocity model for our locations.

Fig. 4.3 presents the results for the hypocenter inversion using all four subsets of stations. As expected, the formal location errors shrink as more stations are used in the analysis. The largest errors for the inversion come from using variation 3, a subset of 11 AIDA location stations (Fig. 4.1b). A dramatic improvement occurs from variation 2 in which all 20 AIDA location stations were used. Further reduction in the uncertainty of the focal depth is observed when the high-density array (HDA 1) is included (variation 1) in the inversion, which not surprisingly corresponds to the smallest location ellipsoid. The best hypocenter estimate is therefore at latitude 43.627 ± 0.001º N, longitude 70.684 ± 0.0014º W with a depth of 6.9 ± 0.15 km.

A very tangible benefit of dense arrays (e.g., HDA 1) is that it facilitates the estimation of a focal mechanism solution when using high frequency sensors (i.e., geophones) in noisy environments (e.g., when deploying next to roads as done in this study). The procedure to estimate the polarity of P-wave arrivals for the location array is illustrated in Fig. 4.4. First, a band pass filter (6-18 Hz) is applied to the HDA 1 seismograms (Fig. 4.4a), followed by a moveout correction to align the waveforms (Fig. 4.4b). Then all the seismograms are added (stacked) to form a composite single trace (Fig. 4.4c). This master trace is then compared (i.e., visually and by cross-correlation) to all location array stations to determine their polarity relative to the master trace derived from the dense array (Fig 4d). The last step in determining the focal mechanism solution is to identify location array stations with sufficiently high signal-to-noise ratios (SNR) to allow robust P-wave first-motion determinations (e.g., Fig. 4.5). The resulting upper hemisphere focal mechanism indicates that the aftershock was primarily a strike-slip event with nodal planes striking 37º and 300º, and dipping 78º and 63º, respectively. In Fig. 4.6 this focal mechanism is mapped onto a lower hemisphere projection to facilitate comparison with the mainshock focal mechanism obtained by the *USGS*, [2012]. Both focal mechanisms agree with the EW direction of maximum of horizontal stress for New England observed by *Gephart and Forsyth*, [1985], *Ebel and Kafka*, [1991], and *Zoback*, [1992].

The coda length magnitude MC of the aftershock recorded by the AIDA array is estimated from the Weston recordings to be MC = 0.6 based on the formula of *Rosario*, [1979]. Data presented by *Ebel*, [1982] suggests that for New England MC values equate to that of the *Nuttli*, [1973] magnitude scale mg(Lg) in the range 1.5 ≤

MC ≤ 5. Furthermore, it appears from the work of *Street et al.*, [1975] that mg(Lg) magnitudes are consistent with the standard body-wave magnitude mb for values in the eastern U.S. for earthquakes in the range $0.5 \leq mb \leq 3$. These relationships would suggest that the body wave magnitude of the AIDA recorded aftershock is about mb ~ 0.6.

One of the advantages of dense array recording is that spatial coherence (i.e., visual trace-to-trace correlation) can result in the detection of smaller events than those generally identified from amplitude bursts within sparser arrays [*Davenport et al.*, 2014]. If we conservatively assume that our AIDA array should be able to detect a coherent event down to an amplitude with SNR of ~ 1, we can estimate our event magnitude detection threshold by comparing the amplitude of the aftershock (i.e., magnitude mb ~ 0.6) to the amplitude of the ambient background noise. Fig. 4.7 shows amplitude vs. time for the average seismic trace recorded with the HDA 1. This plot indicates a difference of ~ 60 dB (i.e., amplitude ratio of 0.001) between the body waves (i.e., P and S waves) and the background noise. In Fig. 4.8 we illustrate how a synthetic seismogram for the aftershock would appear on the dense array assuming various levels of signal to noise. The added synthetic noise is Gaussian with a spectrum that is flat up to 50 Hz. The geometry of these gathers is the same geometry as that used in the deployment of HDA1. Fig. 4.8 suggest that events with SNR ~ 1 are still clearly detectable by simple visual inspection, and much lower can be picked out if digital event detection (e.g., cross-correlation) were applied. Extrapolating this result to the measured mb ~ 0.6 aftershock amplitude with SNR = 60 dB, we calculate that a mb = -2.5 event would still have been obvious on the HDA 1 array recording.

4.5 Imaging with earthquake sources

Given the depth of this event, correlating it to known faults at the surface is speculative at best. However, *Quiros et al.*, [2012] demonstrate how AIDA arrays can potentially provide detailed reflection information on subsurface structure by using the aftershocks as imaging sources. Fig. 4.9 explicitly illustrates how aftershocks recorded by surface arrays can be treated as Reverse Vertical Seismic Profiles (RVSP). In this treatment the earthquake serves as an illumination source for subsurface structure beneath the hypocenter. Although the true power of such an analysis is based on having multiple sources recorded by a dense 2D surface grid, even a single event recorded by a single dense surface profile can be used to generate a reflection profile in which geologic structures can be identified.

To calibrate our analysis a synthetic vertical component reverse VSP (RVSP) record was created with the exact geometry of the HDA 1 array and a simple explosive source at the aftershock hypocenter (Fig. 4.1b). Random noise with an RMS amplitude equal to 2% of that of the artificial signal was added to the synthetic source trace. The synthetic record section was calculated using a simplified velocity model derived from controlled source, wide-angle data from central Maine [*Luetgert et al.*, 1987]. The velocity model has two major assumed discontinuities beneath the hypocenter: a lower crustal reflector at 25 km and the Mohorovičić (Moho) discontinuity at 35 km. A VSP to Common Depth Point (VSP-CDP) transformation [*Hardage,* 2000] is applied to the synthetic to obtain a single fold reflection image beneath the source (Fig. 4.10a). This transformation consists of 3D point-to-point ray tracing for each source-receiver pair that correctly maps the lower crustal and Moho reflections into the horizontal

distance-depth domain. Before applying the VSP-CDP transformation to the aftershock, the data went through a number of processing stages which are essentially identical to steps done in seismic reflection processing. These include first break picking, geometrical binning, static elevation correction, direct S-wave mutes (i.e., zeroed to avoid mapping it into the P-wave spatial domain), velocity model improvement by least-squares inversion of travel times, and bandpass filtering (6-40 Hz).

Although the reflection image obtained by applying the VSP-CDP transformation to the processed aftershock (Fig. 4.10b) does not contain any particularly prominent reflections that could be interpreted as specific structures (e.g., faults or Moho), it does suggest a highly reflective lower crust in a manner similar to that observed on conventional deep seismic reflection images in the northern Appalachians [e.g. *Spencer et al.*, 1989].

4.6 Concluding remarks

As expected, the availability of a large number of stations favorably distributed around an aftershock zone greatly improves hypocentral locations, especially if those stations are positioned at very close spacing, as well as providing sufficient data for source function (i.e., focal mechanism) recovery while using instrumentation designed for reflection seismology and deployed in noisy environments (i.e., next to roads). These benefits of this kind of deployment are expected for several reasons: the favorable azimuthal coverage, the large redundancy of the recordings and perhaps not least to the fact that if enough stations are present, some are likely to be directly above the hypocenter and thus improve depth control immensely. Perhaps the most powerful

aspect of this approach is that it can be applied to very small events that are well beyond the threshold of detection for conventional arrays. In this case we believe the AIDA Maine deployment should have detected events as small as mb ~ -2.4. The lack of such events underscores the small number of aftershocks previously noted for some earthquakes in New England [*Ebel*, 1984].

A novel aspect of dense arrays is that reflection imaging of subsurface structures can be achieved by treating earthquakes as sources in a reverse VSP geometry. Applying the VSP methodology [*Hardage*, 2000] to the only recorded aftershock in this experiment results in an unmigrated reflection image showing hints of lower crustal reflectivity reminiscent of continental reflection surveys throughout the Appalachians. Had more aftershocks been available and recorded by a true dense 2D surface array (i.e., grid of stations), a more useful image of the hypocentral volume would have been recovered.

Both the AIDA Virginia and AIDA Maine deployments were pilot studies using instrumentation that was available but designed for another purpose. However, state-of-the-art industry instrumentation is now available that would facilitate continuous recording for long intervals of time (i.e., 2-4 weeks) with 1000-10000 highly portable 3-component instruments. The Maine experiment makes clear that such recording should revolutionize our ability to characterize aftershocks distributions and image their related structures.

4.6 Figures

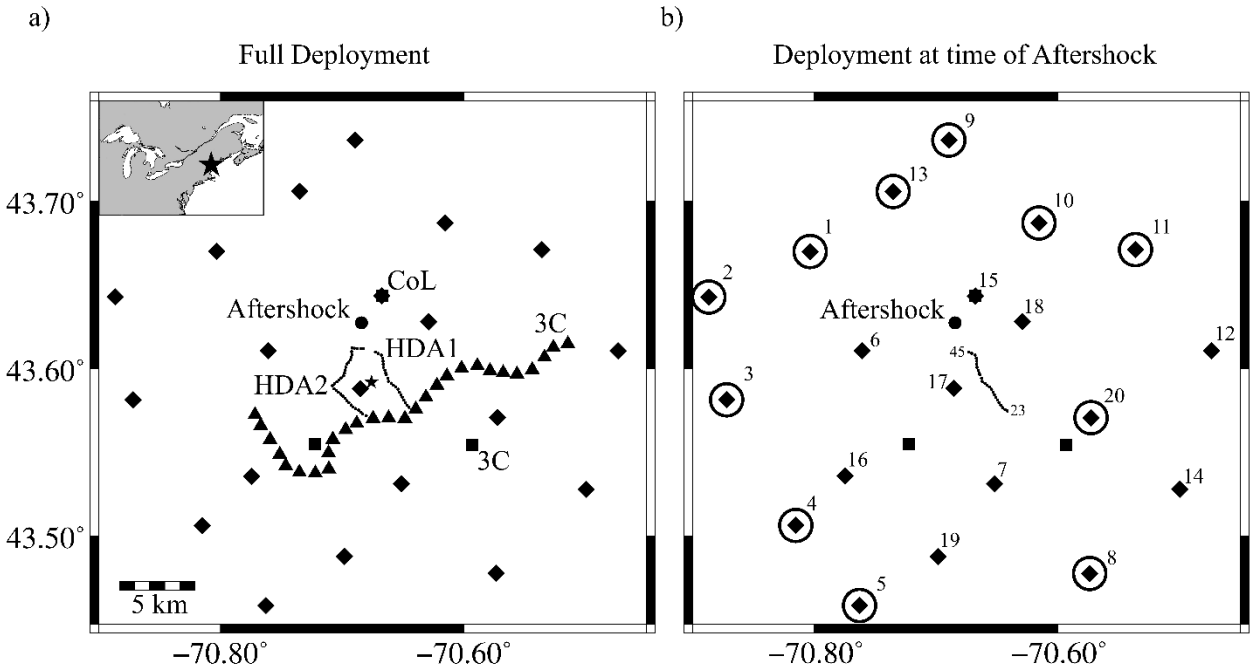

Figure 4.1: Distribution of seismographs near the epicenter of the Mw 4.0 Waterboro, Maine, earthquake. Inset map shows a star centered on the mainshock epicenter. (a) Full deployment of stations around the mainshock epicenter (star), enclosed by the high-density arrays (HDA) (dotted lines), and the three-component (3C) array (triangles). The location array (diamonds) and the three Weston Observatory 3C stations (squares) are shown. (b) Deployment of stations at the time of the aftershock (solid circle). AIDA stations are numbered 1–20 for the location array and 23–45 for the HDA 1 stations (stations 21 and 22 were removed for quality control and did not record the aftershock). The circled diamonds are the subset of the location array stations referred to in the location analysis.

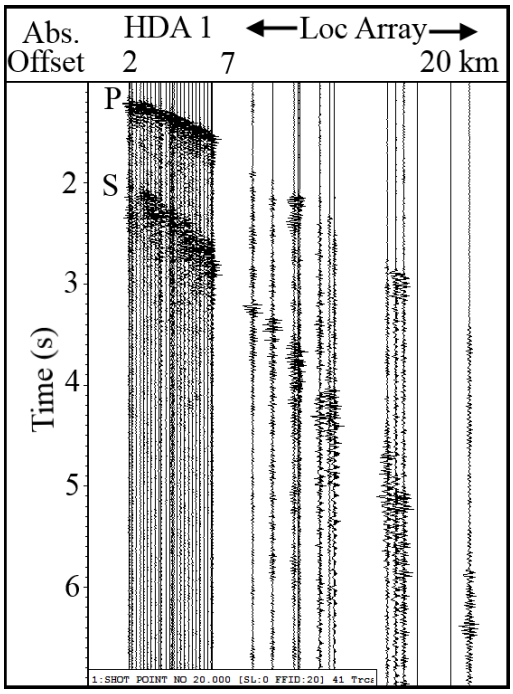

Figure 4.2: Vertical-component seismograms of the 20 October aftershock, recorded by the 43 AIDA stations that were deployed at the time of the event. The horizontal axis is absolute offset from the epicenter. P- and S-arrivals are indicated in the figure. Event origin time has been time shifted to zero (zero time is off scale on the vertical axis) to replicate a controlled source record.

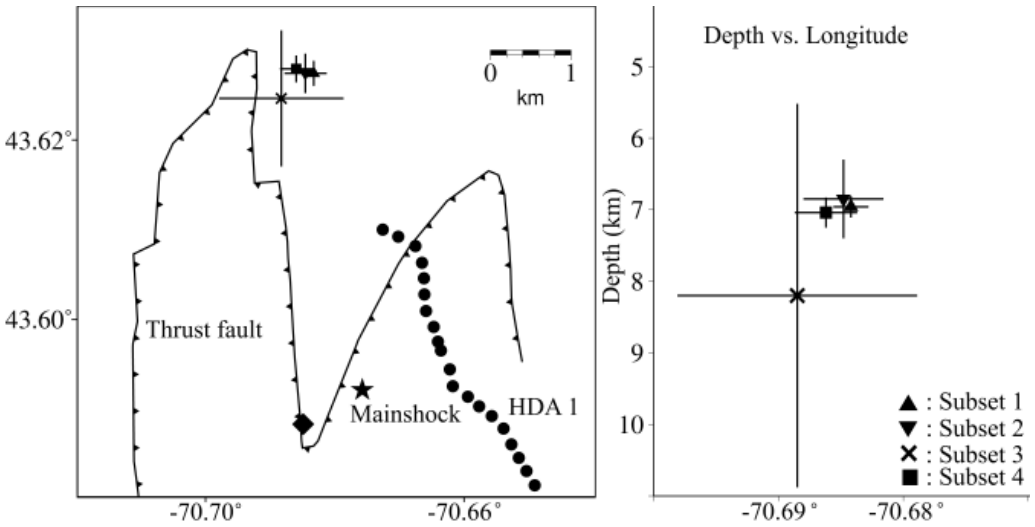

Figure 4.3: Results for the aftershock hypocenter for the four subsets of stations with their corresponding error bars for the (left) epicenter and (right) depth. Subset 1 refers to all 43 AIDA stations that recorded the aftershock, subset 2 refers to all location stations, subset 3 refers to 11 AIDA location stations, and subset 4 refers to all 43 AIDA stations plus the three Weston stations (see Fig. 4.1b). The diamond in (a) corresponds to the only location array station falling within the map region. The thrust fault trace is shown [*Osberg et al.*, 1985].

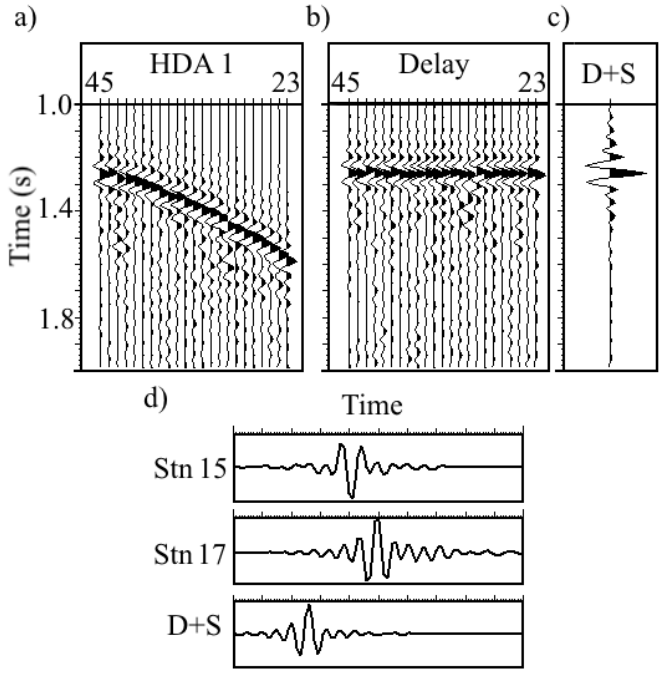

Figure 4.4: (a) HDA 1 seismograms filtered (6–18 Hz) with clear moveout of P-wave arrivals. (b) HDA 1 seismograms P-wave arrivals corrected for the P-wave moveout. (c) Result of adding all seismograms in (b). (d) Polarity comparison between delay and sum trace (D + S) of HDA 1 and location array stations. Station 15 has opposite polarity to D S, whereas station 17 has the same polarity as D + S.

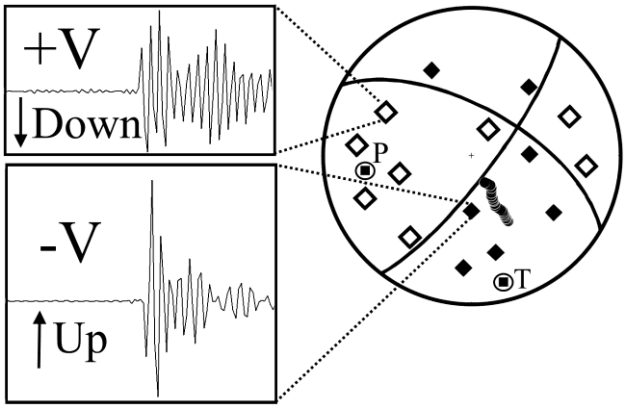

Figure 4.5: Upper hemisphere focal mechanism for the Waterboro, Maine, aftershock. The circled squares indicate P- and Taxes. Diamonds and points indicate projections on the stereonet of stations used for focal mechanism solution (see Fig. 4.1). Filtered seismograms (12–40 Hz) of location array stations 1 and 17 are shown. Compression or upward ground motion (i.e., negative voltage, −V) is designated by filled symbols and downward motion by unfilled symbols.

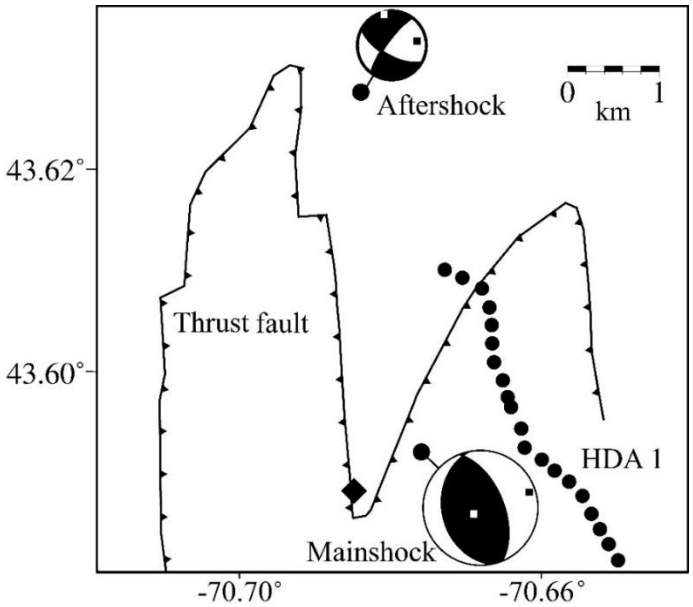

Figure 4.6: Focal mechanisms on lower hemisphere projections for the 16 October mainshock and the 20 October aftershock. P and T axes are shown on each focal mechanism as black and white squares, respectively. The diamond corresponds to the only location array station falling within the map region. The thrust fault trace is shown [*Osberg et al.*, 1985].

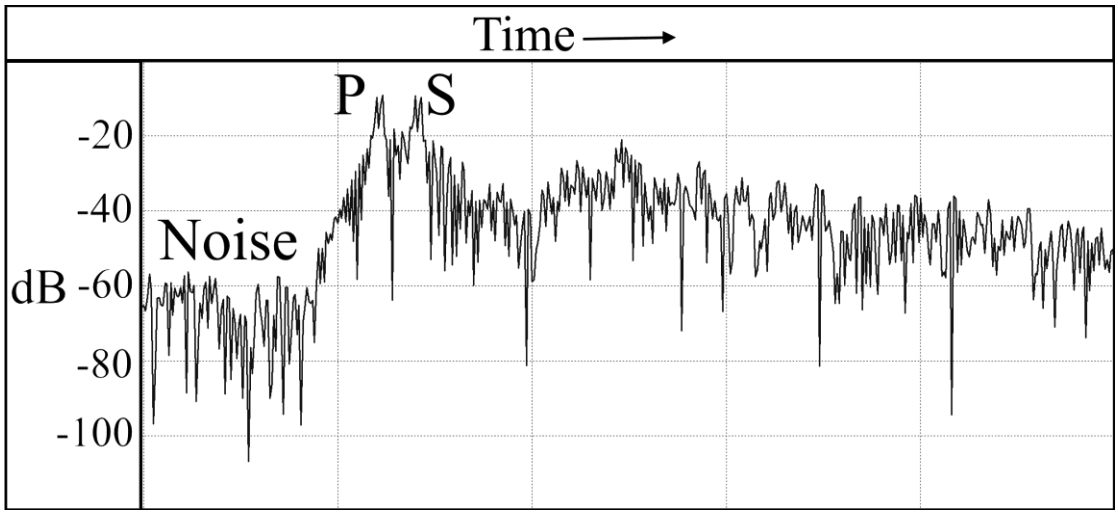

Figure 4.7: Amplitude versus time plot of average seismogram recorded by HDA 1. Background noise, P- and S-arrivals are labeled.

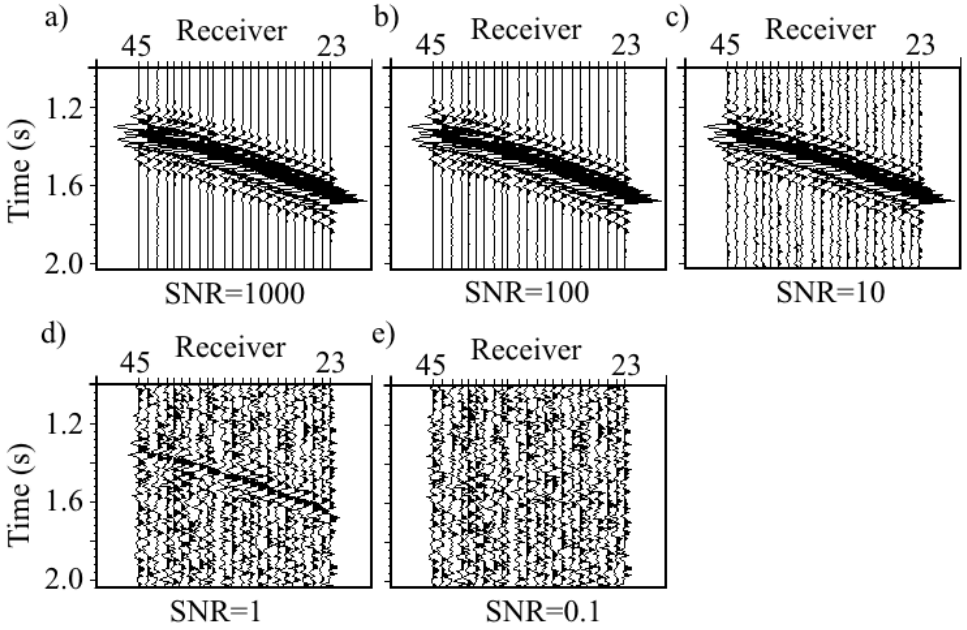

Figure 4.8: Visual threshold estimation of HDA using the waveform from Fig. 4.4c with a moveout derived from the aftershock P arrivals. Panels with different amounts of signal-to-noise ratio (SNR) of (a) 1000, (b) 100, (c) 10, (d) 1, and (e) 0.1. The horizontal axis displays offset identical to the geometry of the HDA 1 (i.e., ~200 m).

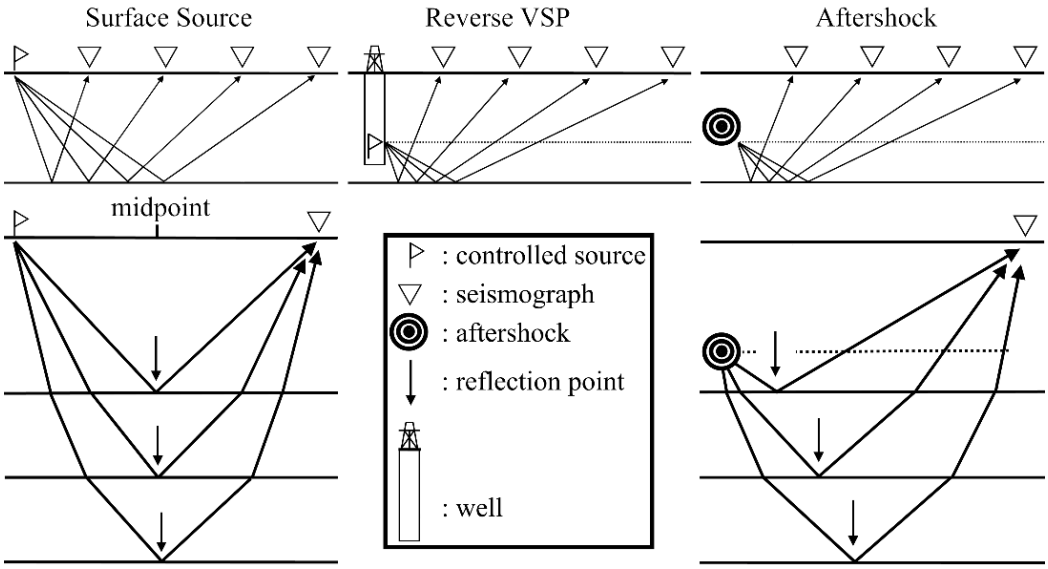

Figure 4.9: (Top) Geometric difference between reflection ray paths for a surface source, for a subsurface artificial source in a conventional reverse vertical seismic profile (RVSP) survey, and for treating an aftershock as a reflection source. The differences of reflection point locations for a surface source–receiver pair (bottom left) and for an aftershock–receiver pair (bottom right). For a subsurface source (e.g., an aftershock), the reflection points move away from the source as a function of source hypocenter and receiver offset, resulting in curved seismograms in the space–travel time domain.

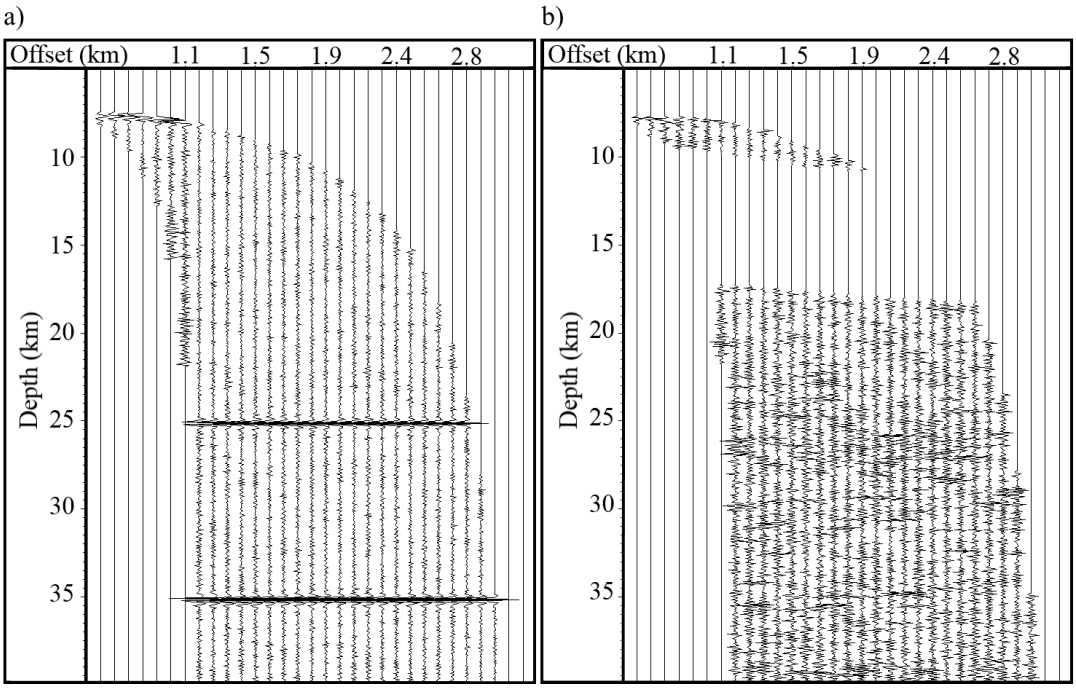

Figure 4.10: Unmigrated 2D reflection image extracted from a 3D volume after the vertical seismic profiling–common depth point (VSP–CDP) transformation of (a) a vertical-component synthetic record with identical geometry to the Maine aftershock modeled with a 25 km deep reflector and a 35 km deep Moho discontinuity (2% noise added), and (b) the Maine aftershock vertical- component record with muted S-wave arrivals and exponential gain to equalized amplitudes.

REFERENCES

Bounif, A. et al. (2004), The 21 May 2003 Zemmouri (Algeria) earthquake Mw 6.8: Relocation and aftershock sequence analysis, *Geophys. Res. Lett.*, *31*(19), L19606, doi:10.1029/2004GL020586.

Brown, L. D. et al. (2011), Aftershock Imaging with Dense Arrays (AIDA) following the August 23, 2011, Mw 5.8, Virginia Earthquake: Feasibility Demonstration and Preliminary Results, *AGU Fall Meet. Abstr.*, *1*, 6.

Davenport, K., J. Hole, D. A. Quiros, L. D. Brown, M. C. Chapman, L. Han, and W. Mooney (2014), Aftershock imaging using a dense seismometer array (AIDA) after the 2011 central Virginia earthquake, edited by J. W. Horton Jr., M. C. Chapman, and R. A. Green, *Geol. Soc. Am. Spec. Pap.*, *The 2011 Mineral, Virginia Earthquake and its Significance for Seismic Hazards in Eastern North America*(509).

Ebel, J. E. (1982), ML measurements for northeastern United States earthquakes, *Bull. Seismol. Soc. Am.*, *72*(4), 1367–1378.

Ebel, J. E. (1984), Statistical aspects of New England seismicity from 1975 to 1982 and implications for past and future earthquake activity, *Bull. Seismol. Soc. Am.*, *74*(4), 1311–1329.

Ebel, J. E., and A. L. Kafka (1991), Earthquake activity in the northeastern United States, in *Neotectonics of North America*, vol. 1, pp. 277–290.

Gephart, J. W., and D. D. Forsyth (1985), On the state of stress in New England as determined from earthquake focal mechanisms, *Geology*, *13*(1), 70–72, doi:10.1130/0091-7613(1985)13<70:OTSOSI>2.0.CO;2.

Hardage, B. A. (2000), *Vertical seismic profiling: Principles*, Handbook of Geophysical Exploration: Seismic Exploration, 3rd ed., edited by K. Helbig and S. Treitel, Elsevier Science, Oxford, UK.

Huang, Y., J. Wu, T. Zhang, and D. Zhang (2008), Relocation of the M8.0 Wenchuan earthquake and its aftershock sequence, *Sci. China Ser. Earth Sci.*, *51*(12), 1703–1711, doi:10.1007/s11430-008-0135-z.

Kim, W.-Y., and M. Chapman (2005), The 9 December 2003 Central Virginia Earthquake Sequence: A Compound Earthquake in the Central Virginia Seismic Zone, *Bull. Seismol. Soc. Am.*, *95*(6), 2428–2445, doi:10.1785/0120040207.

Luetgert, J. H., C. E. Mann, and S. L. Klemperer (1987), Wide-angle deep crustal reflections in the northern Appalachians, *Geophys. J. Int.*, *89*(1), 183–188, doi:10.1111/j.1365-246X.1987.tb04406.x.

Nuttli, O. W. (1973), Seismic wave attenuation and magnitude relations for eastern North America, *J. Geophys. Res.*, *78*(5), 876–885.

Osberg, P. H., A. M. Hussey, and G. M. Boone (1985), Bedrock geologic map of Maine, *Maine Geol. Surv. Scale*, *1*(500,000).

Quiros, D. A., L. D. Brown, K. Davenport, L. Han, J. A. Hole, M. C. Chapman, W. D. Mooney, and A. Cabolova (2012), Reflection imaging using RVSP processing of aftershock recordings from the August 23, 2011 central Virginia earthquake, *AGU Fall Meet. Abstr.*, *1*, 2461.

Rosario, M. A. (1979), A coda duration magnitude scale for the New England Seismic Network, Boston College.

Schweitzer, J. (2001), HYPOSAT — An Enhanced Routine to Locate Seismic Events, in *Monitoring the Comprehensive Nuclear-Test-Ban Treaty: Sourse Location*, edited by F. Ringdal and B. L. N. Kennett, pp. 277–289, Birkhäuser Basel.

Spencer, C., A. Green, P. Morel-à-l'Huissier, B. Milkereit, J. Luetgert, D. Stewart, J. Unger, and J. Phillips (1989), The extension of Grenville Basement beneath the northern Appalachians: Results from the Quebec-Maine seismic reflection and refraction surveys, *Tectonics*, *8*(4), 677–696, doi:10.1029/TC008i004p00677.

Street, R. L., R. B. Herrmann, and O. W. Nuttli (1975), Spectral characteristics of the Lg wave generated by central United States earthquakes, *Geophys. J. Int.*, *41*(1), 51–63.

USGS (2012), M4.0 Waterboro, Maine Earthquake of 16 October 2012, Available from: http://earthquake.usgs.gov/earthquakes/eqarchives/poster/2012/20121016.php

Zoback, M. L. (1992), First- and second-order patterns of stress in the lithosphere: The World Stress Map Project, *J. Geophys. Res. Solid Earth*, *97*(B8), 11703–11728, doi:10.1029/92JB00132.

CHAPTER 5

REFLECTION IMAGING WITH EARTHQUAKE SOURCES AND DENSE ARRAYS: AN APPLICATION OF REVERSE VERTICAL SEISMIC PROFILING (RVSP)

5.1 Abstract

The Mw 5.8 earthquake that occurred in Louisa County, Virginia, on 23 August 2011 (17:51 UTC) resulted not only in the rapid deployment of traditional temporary seismic networks to monitor aftershocks, but also provided an opportunity to record with several "high" density seismic arrays. Traditional aftershock networks consist of a few dozen stations that are spread over tens of kilometers. As a result, the recorded seismic waveforms suffer from spatial aliasing that is so severe that many types of waveform processing are not applicable. Here, we report the results of recording with a large number of oil industry-type instruments that were deployed at a spacing that is an order of magnitude closer than standard deployments. The objective of the deployment was to record seismic wavefields at sufficiently dense spacing to allow the use of array methods to image geologic structure using aftershocks as sources. The receiver array recorded continuously for 12 days and consisted of 172 vertical component seismometers that were placed at 200 – 400 m and a 60 km long 3-component regional profile. Here we demonstrate how processing techniques borrowed from Vertical Seismic Profiling, a common genre of seismic surveys in the oil and gas industry, can be used to produce high resolution 3D reflection images of structure near the aftershock region. These 3D images display reflectivity that

A portion of the material in Chapter 5 has been published under Quiros et al., Reflection imaging using earthquake sources: A novel application of reverse vertical seismic profiling (RVSP), *Society of Exploration Geophysicists New Orleans Annual Meeting 2015, http://dx.doi.org/10.1190/segam2015-5931898.1*

correlates with that observed on a nearby deep seismic reflection survey collected in 1981 by the USGS. Of particular interest is a strong reflector imaged across multiple profiles. This reflector almost certainly represents a thrust sheet like those imaged on the I-64 USGS deep seismic survey. The structure generating this reflector lies between the Elliston Pluton thrust and the Chopawamsic Fault and dips between 15 – 30º southeast. Its listric character is similar to that of the thrusts previously identified in the I-64 profile. Our analysis of this pilot experiment demonstrates how a densely spaced, 2D surface array of seismometers can provide full 3D imaging of crustal structure using microearthquake sources at a fraction of the cost of a conventional 3D controlled source survey.

5.2 Introduction

On 23 August 2011 (17:51 UTC) a magnitude M_w 5.8 earthquake occurred in Louisa County, Virginia (37.905º N, 77.975º W), approximately 135 km southwest of Washington, D.C. (Fig. 5.1). This event was one of the most widely felt earthquakes in United States history with shaking felt from South Carolina to Maine and parts of Canada [*Wald et al.*, 2012]. It occurred within the northern portion of the previously recognized Central Virginia Seismic Zone (CVSZ), a region with a history of small-to-moderate size earthquakes [*Taber*, 1913].

The central Virginia earthquake occurred as the result of a reverse motion along a pre-existing zone of crustal weakness within the CVSZ. The event's hypocenter was located at a depth of 8 km [*Chapman*, 2013] within the crystalline Piedmont Province of the Appalachian orogeny. In this region, the major structural fabric in the upper crust is the result of low-angle thin-skinned thrusting during the

late Paleozoic with high-angle faults present throughout the area as the result of extension in the early Mesozoic [*Chapman*, 2013]. Much of the subsurface structure has been interpreted from a seismic reflection profile collected by the U.S. Geological Survey [*Harris et al.*, 1986; *Çoruh et al.*, 1988; *Pratt et al.*, 2014]. The earthquake and its main aftershock sequence were located within a gently southeast dipping reflector package interpreted to represent thrust sheets of metavolcanic and metavolcaniclastic rocks of the Chopawamsic terrane that lie right above a large basal décollement [*Hatcher Jr*, 1987]. This detachment was imaged by the I-64 USGS deep reflection profile [*Harris et al.*, 1986], recently reprocessed by *Pratt et al.* [2014].

As moderate to large earthquakes in the eastern United States are rare and their origins poorly understood [*Sbar and Sykes*, 1973; *Zoback and Zoback*, 1981], a large cooperative effort was put in place by a group of U.S. institutions to instrument the epicentral area of this event (Fig. 5.1). The overall goal was to gain a better understanding of seismicity in the eastern U.S. and to study the event's relation to pre-existing geological structures [*McNamara et al.*, 2014; *Horton et al.*, 2015]. On the order of 50 three-component (broadband and short period) seismographs were deployed to characterize the aftershock sequence of the Mineral, Virginia earthquake. Prior investigations of the CVSZ have been unable to tie earthquakes to a particular fault conclusively, but the aftershocks for this event clearly delineate a ~10 km long, southeast dipping zone [*Horton Jr and Williams*, 2012; *Davenport et al.*, 2014; *McNamara et al.*, 2014] located on a gentle bend in the regional strike of local geologic units [*Horton et al.*, 2015]. Thorough analysis of the events in this tabular cluster show that their focal mechanisms have a wide range of orientations, implying

they occurred in a zone of positive Coulomb stress transfer [*Wu et al.*, 2015]. Using waveform modeling, *Chapman* [2013] showed that the main shock consisted of three subevents having successive focal depths of 8.0, 7.3, and 7.0 kilometers with estimated uncertainties of ± 1.0 km.

In addition to the broadband and short period seismographs deployed around the epicentral region, a group of researchers from Cornell University, the Virginia Polytechnic Institute and State University, and the U.S. Geological Survey installed a novel, short-term seismic array (Fig. 5.1) in order to evaluate the feasibility and value of using large numbers of seismometers spaced closely together to record aftershock sequences.

5.3 AIDA Deployment

Aftershock Imaging with Dense Arrays (AIDA) was a pilot study intended to assess the value of deploying a large number of seismometers in closely spaced receiver arrays to a) more precisely determine hypocentral locations and source properties at ultra-low magnitudes, b) more accurately define velocity structure within the aftershock zone, c) image geologic structures in the hypocentral volume using reflection techniques with the aftershocks serving as illumination sources, d) characterize regional propagation characteristics, and e) evaluate the potential of seismic interferometry for subsurface imaging using both body and surface waves from aftershocks and ambient "noise" [*Brown et al.*, 2011].

The AIDA experiment (Fig. 5.2) used 4.5 Hz geophones and Ref Tek 125A "Texan" data loggers from the EarthScope Flexible Array pool maintained by the Incorporated Research Institutions for Seismology (IRIS) Program for Array Seismic

Studies of the Continental Lithosphere (PASSCAL). These instruments, originally designed for controlled-source experiments, are highly portable and easy to deploy, facilitating the installation of large numbers in short periods of time. The Texans were programmed to record continuously at a rate of 100 samples per second, resulting in a Nyquist frequency of 50 Hz. This sample rate was selected as the best tradeoff between recording bandwidth and memory limitations.

The first phase of the AIDA deployment (Fig. 5.2a) began on 27 August, 4 days after the main shock. Two teams of 2 people deployed 103 vertical component seismographs (a 4.5 Hz geophone and a Texan recorder) at 200 m spacing in a pair of linear profiles (lines L1 and L2 in Fig. 5.2a). The profiles were installed along local roads for rapid accessibility and based on early estimates of the main shock epicenter.

The second AIDA phase occurred between 1 – 3 September. It extended the vertical component array west of the aftershocks as they were becoming better defined. In addition to the vertical component seismographs, a linear profile of 3-component seismographs (i.e. 3-component geophones simultaneously recorded by 3 individual Texans) was installed radially outward from the main shock in a northeast direction (Fig. 5.2b) to provide better constraints on regional seismic attenuation. The new vertical component array consisted of 115 stations. The array reoccupied line L2 (see Fig. 5.2a) and a segment of line L1, but with a coarser spacing of 400 m. The 3-component array consisted of 29 stations (blue circles in Fig. 5.2b) spaced 2 km apart. The AIDA deployment recorded continuously for 12 days after which the instruments were removed from the epicentral area.

A key objective of the AIDA experiment was to use the recorded aftershocks as illumination sources for reflection imaging. This type of imaging requires that the station spacing must be as small as possible in order to minimize spatial aliasing. It is well known that spatial aliasing occurs when a wavefield's wavelength (λ) is less than the Nyquist wavelength (λ_{Nyq}) [*Yilmaz*, 2001]. For the AIDA experiment, the nominal station spacing of 200 m was selected as a tradeoff between cost and deployment resources, guided by experience with more conventional reflection surveys of basement (e.g. *Brown et al.* [1986]). However, 200 m corresponds to a Nyquist wavelength of approximately 400 m.

The smallest spatial wavelength (λ_{min}) that we would expect to record faithfully depends on the slowest seismic speed (v_{min}) and the highest temporal frequency (f_{max}) (i.e. $\lambda_{min} = v_{min}\, f_{max}^{-1}$). However, here we are primarily interested in P waves. Thus we will focus on the seismic velocity of 6.2 km s^{-1} which is estimated to be characteristic of the epicentral area [*Davenport et al.* 2014]. The maximum frequency observed in the amplitude spectra of aftershocks recorded by the AIDA experiment is approximately 40 Hz (Fig. 5.3a) and the dominant frequency of the P wave reflected energy used in our analysis is about 25 Hz (Fig. 5.3b). These values correspond to minimum wavelengths of 155 m (for highest recorded frequency) and 248 m (for the dominant frequency of reflections). For horizontally traveling P-waves (6.2 km s^{-1}) a maximum station spacing of 77.5 m would be needed to faithfully record the highest possible frequencies. However, as we are interested in upward propagating body waves (i.e. reflections), the appropriate seismic velocity to consider is the apparent velocity given by $v_a = v / \sin \theta_i$, where θ_i is the incidence angle. For vertically

propagating rays ($\theta_i = 0$), the apparent velocity and apparent wavelength are infinite so aliasing is never an issue. Using the velocity of a compressional wave (6.2 km s^{-1}), a wavelength of 400 m, and a frequency of 25 Hz, we can compute the maximum angle of incidence for rays to be accurately recorded from $\theta_i = \sin^{-1} (v / \lambda f)$. Solving for the incidence angle, we can conclude that P-waves that propagate with an incidence angle of less than ~38º should not be spatially aliased. Even at the highest frequencies (40 Hz) P-waves should be not be aliased for angles of incidence less than ~23º. These simple calculations should make clear what a "dense" array means in the context of this study. "Dense arrays" are those in which the station spacing is small enough that the waveforms of interest are not spatially aliased.

5.4 AIDA Aftershocks

In addition to minimizing aliasing, dense deployments have a number of important benefits for recording aftershock sequences. A major one is the lowering of the detection threshold for small magnitude events. An example of such an event is shown in Fig. 5.4. The magnitude of this event is estimated to be between M -2 and M -3, and the seismograms correspond to lines L1 and L2 from the first phase of the experiment (Fig. 5.2a). Fig. 5.4(a) shows recordings at stations spaced approximately 4 km apart to mimic what a conventional deployment would record; no event can be recognized. However, this same recording displayed with a station spacing of 200 m clearly exhibits coherent energy that can be interpreted as both a P and an S waves on stations from line L2. Small magnitude events like the one in Fig. 5.4 are generally not documented in conventional aftershock catalogs. Their detection with standard aftershock networks would be difficult as their signal-to-noise ratio is low and the

station spacing is on the order of kilometers. The close station spacing of dense arrays allows for detection of very small magnitude events by simple visual trace-to-trace correlation.

Another advantage of dense arrays is that the close station spacing permits the identification of more seismic phases than would be possible with a conventional aftershock network. Fig. 5.5 shows another aftershock recorded during AIDA. The seismograms correspond to the stations from line L1 (see Fig. 5.2a). In Fig. 5.5(a) it is only possible to identify clearly P and S arrivals. Fig. 5.5(b) shows all the recorded seismograms along L1. From the denser spacing, not only can we see the P and S phases observed previously, but we can also observe coherent arrivals that were virtually impossible to identify on the four traces in Fig. 5.5(a).

Arrivals such as the one shown in Fig. 5.5(b) that do not correspond to neither direct P and S propagation are abundant in the aftershocks recordings collected during AIDA. Using simple travel-time modeling of an aftershock (Fig. 5.6), we argue that these arrivals most likely correspond to reflections from subsurface interfaces. Fig. 5.6(c) shows synthetic seismograms that result from using the hypocenter of an event recorded during AIDA and a simple earth model. The earth model consists of a single layer over a half space. The seismograms show clear P and S arrivals in addition to a reflection (PxP) whose travel time behavior is very similar to arrivals observed on the AIDA seismograms.

The AIDA experiment successfully recorded on the order of 2600 earthquakes during the 12 days that the deployment lasted. Many of these events show coherent phases at travel times that follow the direct P-wave and are prior to the direct S-wave

(Fig. 5.7). As will be argued later, we interpret these phases as reflections from the southeast dipping, complex imbricate thrust sequence imaged by *Pratt et al.* [2014] on the deep seismic reflection line collected by the USGS along interstate I-64 [*Harris et al.*, 1986]. These reflected arrivals are the basis of our reflection imaging with the aftershocks as the illumination sources.

5.5 Reflection Imaging with Earthquake Sources

Imaging geological structure with reflected phases from earthquake sources has been a mainstay of global seismology since its inception [*Gutenberg*, 1951]. However imaging crustal structure from local microearthquake sources has been much less common. An early, and one of the most prominent examples is perhaps the mapping of a mid-crustal discontinuity with reflected phases from local events near Socorro, NM [*Sanford and Long*, 1965]. This feature was later interpreted to be a magma body [*Sanford et al.*, 1973] as was imaged in detail by the COCORP deep seismic reflection surveys of 1976 and 1977 [*Brown et al.*, 1979]. Similar examples have been subsequently reported in the literature, especially from Japan [*Mizoue et al.*, 1982; *Horiuchi et al.*, 1988; *Iidaka et al.*, 1993; *Matsumoto and Hasegawa*, 1996; *Nishigami*, 1997; *Umino et al.*, 2002; *Doi and Nishigami*, 2007].

A few studies have attempted to use the tools of common midpoint (CMP) processing to image reflectors illuminated by local seismicity. *James et al.* [1987] and *Meyer and James* [1987] obtained near-vertical reflection profiles from upper crustal seismicity north of the Snake River Plain Yellowstone volcanic belt. *Byerly et al.* [2010] used a dense line of receivers and shallow seismicity on the volcanic island of Montserrat, BWI, to image sub-horizontal sill-like features by CMP stacking. *Chávez-*

Pérez and Louie [1995, 1998] imaged a lower crustal bright spot that extends from the San Gabriel Mountains into the Mojave using wide-angle reflection and pre-stack depth migration. However, to the authors' knowledge, *Inamori et al.* [1992] were the first to recognize that to accurately image reflections from microearthquakes sources one must account for the different ray path geometry generated by sources at depth. *Inamori et al.* [1992] used a normal-moveout correction adapted for sources at depth to image a reflector beneath western Nagano Prefecture in Japan. Their approach was to time shift the seismograms with the NMO correction and to convert them to depth using a constant velocity. Their results show receiver gathers (i.e. single station and multiple earthquakes) with clear reflection phases that are attributed to magma. Using the reflection travel times they estimate reflection point locations and show these on map and cross-sectional views, but no attempt was made to map the waveforms directly into 3D space. As we will discuss in the next section, the NMO correction used by *Inamori et al.* [1992] is part of a set of reflection processing techniques used in the oil and gas industry known as Vertical Seismic Profiling (VSP). *Quiros et al.* [2015a, 2015b] applied these VSP processing techniques to create reflection images by mapping the actual waveforms in 3D space from a single microearthquake. In this chapter I attempt to extend the work of *Quiros et al.* [2015a, 2015b] to using multiple earthquakes for 3D imaging via VSP techniques.

5.6 Vertical Seismic Profiling

The rudiments of VSP can be traced back to *Fessenden* [1917]'s patent on a method for ore body prospecting [*Hardage* 2000]. Nowadays, vertical seismic profiling is generally used to correlate (i.e. tie) surface seismic data with the

underlying geology. With the advent of hydraulic fracturing, monitoring has also become a common application of VSP surveys [e.g. *Jupe et al.* 2003]. VSP surveys used to record natural events are scarce, mostly because of the excessive cost involved in drilling. A few important examples are that of *Malin et al.* [1988] and *Chavarria et al.* [2003], both of which used several receivers down boreholes to record upper crustal seismicity, with the former looking at site distortion of P- and S-wave spectra at Oroville, California, and the latter applying Kirchhoff migration to scattered P- and S-waves to image their causative structure at the San Andreas Fault Observatory at Depth.

A VSP survey is one in which either the source, or the sensors, or sometimes both, are deployed down a borehole [*Hardage*, 2000]. There are several types of VSP surveys, with zero-offset VSP surveys having the simplest geometry (i.e. surface source next to wellbore directly above receivers).

As shown in Fig. 5.8, the conventional surface source reflection survey and a microearthquake source reflection survey differ in ray path geometry due to the depth of the earthquake (Figs 5.8a and 5.8b). A single microearthquake occurring several kilometers beneath the surface and recorded by a surface receiver array is directly analogous to a reverse vertical seismic profiling survey (Figs 5.8b and 5.8c) [*Quiros et al.*, 2015a].

Most importantly, unlike for surface surveys where the reflection points lie beneath the common midpoint (i.e. CMP) for a horizontally stratified medium, in microearthquake source surveys the reflection points follow a curved path in 3D space (Figs 5.8d and 5.8e). It is for this reason that approaching microearthquake reflection

imaging through standard methods such as CMP stacking is not appropriate and VSP methods are needed to correctly reproduce the geology of the volume being imaged.

5.6.1 VSP Common Reflection Point (CRP) mapping

Clearly a geometrical mapping is needed that takes into account the depth of the source, the source-receiver offset, and the velocity of the subsurface. Fig. 5.9 illustrates the geometrical mapping that a seismic trace corresponding to a single source-receiver pair must undergo for a constant velocity medium with horizontal interfaces [*Dillon and Thomson*, 1984]. This transformation simply converts a time sample t_i on a seismic trace to its location (x_i, z_i) in the subsurface. The process acts on individual traces, that is, an event (e.g. reflected arrival) on a trace will be mapped without regard to its relation to events on adjacent traces [*Dillon and Thomson*, 1984]. Fig. 5.9(a) shows the energy as recorded by the receiver (e.g. Fig. 5.8e) and Fig. 5.9(b) shows the seismic trace after the application of VSP-CRP mapping. Note that the VSP-CRP mapping has distorted the trace waveform in both dimensions, offset and depth. Moreover, the transformation is non-linear, with the shallower parts of the trace more distorted (stretched) than those at later times. The point in (x_i, z_i) space where different seismic traces intersect constitute Common Reflection Points (CRPs) but not Common Mid-Points (CMPs).

5.6.1.1 VSP-CRP mapping of a single source

Applying this transformation on a trace-by-trace basis will result in the reconstruction of a depth image (i.e. reflection profile) of reflectors in the subsurface. The VSP-CRP transformation defined in Fig. 5.9 can be easily extended to three dimensions. In the 3D case the location of each receiver with respect to the source

defines an azimuth along which the seismic trace is projected (e.g. Fig. 5.9b). To illustrate the procedure we apply the transformation to the synthetic record shown previously in Fig. 5.6. In Fig. 5.10 we have muted the direct S-wave to avoid spatially mapping this energy as if it were a P-wave a reflection. The reflected arrival (PxP) has a clear hyperbolic moveout in a shot-gather (Fig. 5.10c) as expected of a reflection. The result of mapping the reflected arrival in the synthetic record into the depth-offset domain is shown in Figs 5.10d and 5.10e. For simplicity, we have plotted the results for lines L1 (Fig. 5.10d) and L2 (Fig. 5.10e) separately. The reflected arrival (PxP) which results from a horizontal layer is mapped to a flat interface at 6 km in agreement with the structural model used to generate the synthetic record. The 'bumpy' appearance of the reflector in Fig. 5.10(d) is a visual artifact of the viewing angle and the three-dimensionality (i.e. meandering) resulting from the use of the AIDA receiver locations relative to the hypothetical event's epicenter (Fig. 5.10a).

We applied the VSP-CRP transformation to an actual AIDA aftershock record in Fig. 5.11. For this mapping we used the constant P-wave velocity of 6.2 km s^{-1} as reported by *Davenport et al.* [2014]. The event's epicenter is shown in Fig. 5.11(a) relative to the recording arrays. It occurred at a depth of 3380.2 m. The recorded seismograms are displayed in Fig. 5.11(b). The S-wave has been muted as it was done in Fig. 5.10(c). Two distinct reflected arrivals (PxP) are evident on the seismograms for line L1, while only one reflected arrival is clear on the seismograms for line L2 (Fig. 5.11b). Applying the VSP-CRP mapping to these traces results in the corresponding depth images shown in Figs 5.11c and 5.11d. The direct P-wave has been mute following the mapping to minimize the use of amplitude gain functions.

Again, we have plotted the depth image for line L1 (Fig. 5.11c) separately from the depth image for line L2 (Fig. 5.11d). These images not only clearly map the 3D geometry of the dominant reflection (PxP 1), but also image a number of weaker subparallel events of varying continuity beneath these two lines.

Although the VSP-CRP transformation illustrated in Fig. 5.10 is strictly applicable to simple geologic settings (i.e. constant seismic velocity and horizontal layers), it demonstrates the basics of the spatial mapping that a single source record experiences and yields credible results even for shallowly dipping events (Fig. 5.10).

More robust VSP-CRP transformation in which 3D ray tracing is done through a complex velocity model are available to produce more accurate representations of the subsurface. Here we use an industry software package called Vista 2013 3D (Schlumberger ®) for pre-processing and VSP mapping. For Fig. 5.12 we applied the VISTA VSP-CRP mapping algorithm to earthquake 156, which was previously displayed in Fig. 5.7. This earthquake has a strong reflection arrival in the P-wave coda (Fig. 5.7). The pre-processing applied to the record is a bit more extensive than in Figs 5.10 and 5.11; in addition to mutes for the S-wave, the S-wave coda, and the first arrival, we included a spherical divergence correction to the amplitudes. The velocity model used is defined by layers of distinct P-wave velocity. The results from the VSP-CRP mapping are shown in Figs 5.12 and 5.13 as images along inline and crossline geometries (see discussion below). The traces in Fig. 5.12(a) correspond to the 3D mapping of the seismograms in line L1 on the original earthquake gather (see Fig. 5.7). Similarly, the traces on Fig. 5.13(a) correspond to the 3D mapping of the seismograms in line L2 on the original earthquake gather. The reflector (PxP) appears

to dip southeast in Fig. 5.12(a), and to be subhorizontal in Fig. 5.13(a), thus defining a southeast dipping geological interface. In the next section we will discuss in more detail the VSP-CRP processing applied in Figs 5.12 and 5.13 while expanding the analysis to use multiple earthquakes in an attempt to increase signal-to-noise via stacking while fleshing out the image in 3D space.

5.6.2 VSP-CRP mapping with multiple sources

As shown in the previous section, the recordings for a single event will map the position of the corresponding reflections in 3D with respect to the surface array location. Other events will map the same or similar reflections in other portions of the subsurface volume. Where these mappings overlap, the result can be stacked to provide increased signal to noise. In this section we will produce such a stacked volume image using multiple earthquakes, and describe some of the factors which limit the effectiveness of such data integration.

For this imaging we used events contained in the double-difference catalog of *Wu et al.* [2015]. This catalog contains 200 events that were recorded during the AIDA deployment, each with magnitude and a focal mechanism estimate. As with standard CMP reflection processing, a degree of pre-processing was needed before the application of the mapping and stacking algorithm. As for Figs 5.12 and 5.13, we make extensive use of the seismic processing package Vista 2013 3D for pre-processing and for VSP mapping and stacking.

The AIDA instruments were deployed along local roads for rapid accessibility, resulting in ‘contamination’ of some earthquake records with vehicle signals and other man-made ‘noise’. These unwanted signals were zeroed to avoid mapping them into

the depth-offset domain. Another source of 'noise' is the S-wave and its coda, which persists throughout all earthquake gathers. These signals were muted in the same way as shown in Figs 5.10c and 5.11b. The point to stress here is that since we are creating a P-wave reflection image we want to remove any S-wave energy (i.e. reflections and direct arrival) present that can be obscuring P-wave reflections. By not removing this S-wave energy we also run the risk of mapping them into the P-wave reflection image and interpreting them as structure. The best approach to deal with the S-wave energy would be to do a wavefield separation via a three-dimensional rotation (i.e. ZNE to LQT) but this requires 3-component data for each station. Another aspect that needs addressing is that earthquakes have different magnitudes resulting in large amplitude variations throughout the catalog. To scale the different size earthquakes we calculate the amplitude of an earthquake relative to magnitude zero (i.e. $\frac{10^m}{10^{0.0}}$) and use the resulting number as the scaling factor. Band-pass filtering is then applied to all the records in the range 8 – 44 Hz. In addition to magnitude scaling, a correction is applied to the earthquake gathers to compensate for amplitude decreases due to spherical expansion of the wavefronts.

All 200 events in the catalog (Fig. 5.16) are of the reverse type, although with different orientations. Thus a methodology is needed to equalize the events with different rupture kinematics. Even if the focal mechanisms were not a problem, the source time functions could be different. For every event, we attempted to correct for the variations in source time function by applying spiking deconvolution. The procedure derives the spiking deconvolution operator (e.g. standard Wierner Levinson algorithm) of the first arrival at each seismogram in each microearthquake. The

operator is then convolved with the data. By converting every trace into a spike (e.g. delta function) we attempt to remove differences in the wavelet's shape that result from different source time functions. Keep in mind that although this procedure reshapes the wavelet it does not change its polarity which results from the radiation pattern of the earthquake and the station distribution. Visual inspection of several records appears to show the same polarity for the first arrivals, even for different earthquakes, suggesting that the stations used here lie dominantly in similar places of the focal sphere. However, inspecting every earthquake record becomes impractical for a large number of events. For this reason an automatic polarity detection and correction is used to modify any polarity differences after the application of deconvolution.

Next, the direct P-wave (i.e. first breaks) was manually picked after noise editing. A "top mute" was applied to remove the first arrival and any energy arriving before the first arrival, as this energy could not have been generated by the event under analysis and is considered noise. In addition, we define a 3D velocity model that will be used for the mapping and stacking process. The model is defined by layers with distinct P-wave velocities. We use a surface velocity of 5.6 km s^{-1}, increasing to 5.9 km s^{-1} at 3 km to match those found by *Pratt et al.* [2014]. The velocity model increases gradually from 5.95 km s^{-1} at 4 km to 6.45 km s^{-1} at 9 km. The last step is the VSP-CRP mapping and stacking. This process occurs within a 3D grid in which the velocity model is imbedded. The Vista software uses a 3D point-to-point anisotropic ray tracer, in which rays are calculated for each reflecting horizon in the 3D velocity model using the locations of each source-receiver pair.

A key element of the VSP-CRP mapping and stacking process is the definition of the 3D grid. The grid is made of hexahedral cells (e.g. rectangular cuboids) with their dimension and orientation (azimuth) controlled by the user. The vertical dimension of the grid cells is important as it controls the depth sample interval of the image. To determine an appropriate depth sample interval we approximate the distance a ray travels during one time sample. This distance is given by the average interval velocity in the model multiplied by half the temporal sample interval of the data. Using a velocity of 6.2 km s^{-1} and a sample interval of 0.01 s we obtain a depth sample interval of approximately 30 m. The horizontal dimensions of the grid are chosen depending on the grid's orientation and source receiver ray paths available to sample a particular portion of the grid.

By applying the processing just described to all 200 events in the *Wu et al.* [2015] catalog we can produce a stacked depth image underneath the array. As mentioned earlier the grid orientation and the horizontal grid cell size are important parameters, especially when only a small portion of the grid is actually sampled at the surface. For the following depth images we have chosen a grid orientation of 40º with respect to North. The grid is made of cross-lines with a 40º azimuth and in-lines which are orthogonal (azimuth 130º) to the cross-lines. This orientation was chosen to include as many traces per in-line as possible while maintaining an orientation that is similar to the section of USGS I-64 reflection profile (azimuth ~ 133º). The dimensions of each grid cell are 30 x 460 x 30 m, where these values correspond to cross-line, in-line, and depth spacing, respectively. The grid is shown in Fig. 5.14, with 3 in-lines (IL 7, 8, and 9) and the bounding cross-lines indicated (XL 100 and

320). The shot locations (black circles) for the USGS I-64 reflection profile [*Pratt et al.*, 2014] are marked as well. In addition, the epicenters (red dots) of the 200 events in the *Wu et al.* [2015] catalog and the location of the main shock (red star) are shown.

Three reflection profiles obtained from the VSP-CRP transformation that used all 200 events are shown in Fig. 5.15. The full grid is relatively sparsely populated due to the aftershock and receiver distribution. For this reason the majority of the non-zero amplitudes for these in-lines are found between cross-lines 100 and 320 (Fig. 5.15). In other words, the depth profiles in Fig. 5.15 are oriented along in-lines 7, 8, and 9 because this is where the densest subsurface coverage is obtained. The procedure applied to the aftershock catalog to produce Fig. 5.15 is essentially similar to that applied in Fig. 5.12, with the added steps of magnitude equalization, spiking deconvolution, polarity correction and stacking. Under ideal conditions for imaging (i.e. known velocity model, no uncertainty in the hypocenters, and equal focal mechanisms and source time functions) one would expect that the reflection volume would show the southeast dipping structures observed in the USGS I-64 profile [*Pratt et al.*, 2014] and in Fig. 5.12. While southeast dipping energy is present in Fig. 5.15, it is difficult to isolate specific interfaces. To examine how various factors may have compromised the final stacked reflection volume, we have chosen to focus on a subset of events from the *Wu et al.* [2015] catalog that exhibit clear reflected phases on their corresponding shot gathers, and have sources which are clustered within a 1.5 km radius.

The subset consisted of 13 aftershocks (Fig. 5.16) that exhibit clear reflected arrivals and low noise levels. Fig. 5.16 shows a map of the epicenters of these events

and the receivers that were ‘live’ at the time these events occurred. The focal mechanisms of these events indicate reverse motion with a large assortment of fault plane orientations (Fig. 5.16). In Fig. 5.17 we show the example seismograms of 4 of these events with their corresponding depth, magnitude and most prominent reflector specified. As all 13 events are located within a 1.5 km radius, their records look quite similar (Fig. 5.17). The pre-processing steps applied to the 13 events are essentially the same as in Fig. 5.15 (trace editing, magnitude scaling, band-pass filtering, spherical divergence correction, muting, and spiking deconvolution) with the exception of the polarity correction. These steps are followed by application of the VSP-CRP mapping and stacking algorithm resulting in Figs 5.18 and 5.19. Fig. 5.18(a) shows an in-line stacked reflection profile (orientation in Fig. 5.18b), while Fig. 5.19(a) displays a cross-line profile (orientation in Fig. 5.19b). These two reflection profiles show a much enhanced image of the PxP reflector (compare with Figs 5.12 and 5.13) as well as numerous, less prominent reflectivity. Stacking fold values, indicating the number of events that contributed to each grid cell, for the traces in Figs 5.18 and 5.19 range from 1 to 9.

Visual inspection of this subset of events suggested a common polarity for all events, this is reflected in the effective stacking of the PxP reflector without the use of the polarity correction, previously applied to the 200 event catalog (Fig 15). Furthermore the first arrival for all events (e.g. Fig. 5.17) resembles a zero-phase wavelet, suggesting that the deconvolution applied may have provided modest improvement at best. In Fig. 5.20 we show the subset stack with and without

deconvolution, with the results showing incremental improvement of the coherence of the reflector.

5.7 Complications

While applying the VSP-CRP transformation to a single microearthquake source (e.g. Figs 5.12 and 5.13) is a practical approach to map geologic structure, the true power of using microearthquakes for reflection imaging lies in the prospect of using the redundancy generated from having multiple sources. Nonetheless, using multiple microearthquake sources for reflection imaging poses several challenges not present in controlled source reflection imaging. We have already mentioned that a large variety of focal mechanisms and source functions might be involved. However, perhaps the most obvious challenge in working with earthquakes is the uncertainty in the hypocenter location and the origin time of the events. Another important difficulty that falls out from using natural events for reflection imaging is the sparse illumination that results from the irregular distribution of microearthquake sources. Earthquakes tend to occur along pre-determined zones of weakness (i.e. faults), so that earthquake distributions tend to be spatially inhomogeneous (i.e. aftershock clusters). A consequence of these earthquake distributions is the lack of illumination of certain areas within the volume of interest.

In this section we will discuss these difficulties further and explore how they affect the results presented in this manuscript, along with suggestions as to how they can be minimized in future experiments.

5.7.1 Hypocenter and origin time uncertainty

Inaccuracies in the hypocenters and/or origin times can clearly be an issue when one is applying a stacking algorithm. The process of stacking relies on mapping an amplitude sample into its correct spatial location in 3D space. The mapping is carried inside a 3D grid made of hexahedral cells, and stacking (i.e. summing) occurs when multiple samples fall within the same 3D cell. However, if a sample is spatially misplaced due to errors in the hypocenter and/or origin time, then it will result in improper stacking. Improper stacking can produce degradation of the depth image by obscuring actual reflectors or generate features in the depth image that do not correspond to the geology underneath the array. Obviously minimizing the uncertainty in the hypocenters and origin times is crucial to obtain a robust reflection image from the methodology discussed here. In this study we use the double-difference catalog of *Wu et al.* [2015] in an attempt to minimize the uncertainty in the aftershock locations. However the difference in the quality of the images in Fig. 5.18 versus Fig. 5.15, with the former using a subset of sources close together, indicates that more accurate locations are needed across the aftershock catalog. A possible approach to reduce the effect of the uncertainty in the earthquake locations on the reflection image would be to treat the errors as a statics problem [*Cox* 1999] in which source corrections are computed from time shifts measured by correlation of the data within each 3D grid.

5.7.2 Source time function and focal mechanism variation

We have already discussed how variations in source time function and focal mechanism can alter the shape and polarity of the wavelet. If the focal mechanisms are not consistent, phase mismatch will cause destructive rather than constructive interference during the stacking process [*James et al.*, 1987]. In the example with 13

events (Figs 5.18 and 5.19) phase mismatch did not appear to be a serious issue as visual inspection of the 13 records revealed no notable differences among the first arrivals for the different events. The most likely reason is that most of our stations where located in roughly the same focal mechanism quadrant for all events in this subset. However as we go to larger number of events distributed over a larger area, the variation in the phase of the direct and reflected arrivals due to focal mechanisms is likely to be much more serious. Even if two events have the same focal mechanism at the same depth, their source functions could differ significantly (e.g. different rise time). Our first order attempt to deal with phase mismatch due variations in focal mechanism and source time functions was to apply spiking deconvolution to force equalization of the imaging wavelet, although the impact of this step seems to have been modest at best for a subset of events (Fig. 5.20). A more robust treatment of the variation in focal mechanism might be based on rotation of the seismograms to a common source mechanism at a common depth.

5.7.3 Illumination

The map in Fig. 5.14 shows how the aftershocks are preferentially distributed in specific regions (i.e. clusters) within the area of interest. This inhomogeneous source distribution in combination with the AIDA receiver array will result in spotty illumination throughout the 3D volume. To identify the illumination characteristics of the aftershock distribution we created a 3D structural model based on the interpreted seismic reflection profile along interstate I-64 (Fig. 5.21) [*Harris et al.*, 1986; *Çoruh et al.*, 1988, p.64; *Pratt et al.*, 2014]. The model (Fig. 5.21c) will serve as our reference to study the illumination of geologic structures with synthetic seismograms.

The interstate I-64 deep seismic survey collected by the USGS [*Harris et al.*, 1986] resulted in a reflection profile that extends from the Appalachian Valley and Ridge Province to the coast [*Pratt et al.*, 2014]. The reflection image shown in Fig. 5.21(a) corresponds to the segment of the I-64 profile closest to the epicentral region (see Fig. 5.1b for reference). Although a large number of reflectors with varying dips are evident in the depth section, we focus on two of these structures as traced on Fig. 5.21(b). The Chopawamsic fault (CF), interpreted in the original depth section by *Harris et al.* [1986] to be of Cambrian origin, sits below the SW projection of the aftershock cloud [*Pratt et al.*, 2014]. The CF, which follows the general southeast-dipping trend of many structures in the area, is well defined on the I-64 seismic profile by southeast-dipping reflectors [*Pratt et al.*, 2014]. The latest significant motion on the CF near the survey area predates the crosscutting Ellisville pluton (EP) and is constrained to an ~10 million-year (Ma) interval in the Late Ordovician between 453 and 444 Ma [*Hughes et al.*, 2013]. The second structure chosen to be included in our model, is an antiformal feature (Fig. 5.21b) with opposite curvature (i.e. concave down) to that of most reflectors in the I-64 profile. This structure, originally not interpreted by *Harris et al.* [1986], was selected to explore the de-focusing associated with buried antiformal geometries and its effect on illumination or lack there off. The strike of these two surfaces was chosen to reflect the surface geologic strike (~45º) [*Pratt et al.*, 2014] resulting in the 3D structural model shown in Fig. 5.21(c).

To study the illumination of these structures we used a velocity model of 2 layers whose interfaces are defined by the structures in the 3D model (Fig. 5.21c). The velocity is kept constant within each layer with the rms velocity of the model being

6.2 km s^{-1}. The illumination analysis is done with the OMNI 3D modeling software package (Schlumberger ®). OMNI uses a 3D ray tracing method that accounts for the depth of the aftershocks and elevation of the receivers. The illumination is calculated by defining a 3D cubical grid. The grid has surface nodes of 100 x 100 m, and the number of bouncing points that fall within a node along the surface of each interface constitutes the illumination value. The illumination value is equivalent to stacking fold.

We start by examining the illumination achieved by the aftershock cloud and a relatively uniform 2D surface receiver array. Fig. 5.22 shows the illumination analyses of the structures defined in the 3D model of Fig. 5.21. The 2D surface consists of 60 stations spaced at 200 m intervals along the E-W direction (i.e. in-line direction) and 31 stations spaced at 400 m intervals along the N-S direction (i.e. cross-line direction) for a total of 1860 stations. These type of surveys are commonplace in the oil and gas exploration industry, with current technology capable of autonomous and continuous recording for weeks or months, and the capability of deploying receivers numbering well into the thousands [*Lin et al.* 2013]. Fig. 5.22(a) shows the effective illumination on the antiformal structure with the color scale displaying the fold. The sections of the antiformal surface that are not illuminated are colored in gray. The combination of this receiver array with the aftershock distribution results in continuous illumination of the antiformal structure along strike, while perpendicular to the strike the illumination occurs in patches. Fig. 5.21(b) shows the illumination of the Chopawamsic Fault, again with the color scale displaying the fold. For this reflector the illumination is

more or less continuous along and perpendicular to strike, with some patches still present.

In contrast, carrying out the same illumination analyses with the AIDA receiver array distribution (Fig. 5.22), which has a limited azimuthal coverage and an order of magnitude fewer stations when compared to the 2D surface array in Fig. 5.21, results in much lower fold values and more patchy coverage in both directions. Fig. 5.22(a) shows the reduced illumination of the antiformal structure by the combination of the AIDA array and the hypocenter cloud. The reduction is not only in the area of coverage where the illumination along strike is diminished, but also in the fold value, which is a consequence of having fewer rays falling within a bin as a result of a reduced number of stations. Similarly, the illumination analysis of the CF reflector (Fig. 5.18b) shows a similar drop in stacking fold value and a drastic reduction in the illuminated area compared with a full surface 2D receiver array.

To further investigate how these two receiver geometries and the aftershock distribution affect the overall VSP-CRP depth images we generated synthetic seismograms (Fig. 5.24) that were then processed via the same steps used in section 4.4. The seismograms are the result of ray-tracing through the 3D structural model (Fig. 5.21c) using the actual aftershock distribution and both receiver geometries: the 2D surface array (Fig. 5.22) and the AIDA receiver array (Fig. 5.23). The synthetics display three arrivals, the direct arrival (P_D), the reflection off the antiformal structure (P_AP), and the reflection off the CF structure ($P_{CF}P$). Fig. 5.24(a) shows an example of some of the synthetic seismograms that result from recording with the 2D surface array, while Fig. 5.24(b) shows the synthetic seismograms that result from recording

with the AIDA array. In total 200 hypocenters [*Wu et al.*, 2015] were used to generate these synthetic seismograms. A 30 Hz zero-phase Ricker wavelet was used as the source function in all seismograms.

Fig. 5.25 shows the result of applying the VSP-CRP mapping and stacking to the synthetic seismograms. A simplified pre-processing sequence (trace editing, band-pass filtering, and muting) was used as there is no variation in focal mechanism and magnitude on the synthetic seismograms. The 3D depth image generated using the 2D surface array (Fig. 5.25a) recovers the dipping CF structure as well as the antiformal horizon over a substantial part of the subsurface. In contrast, and as expected, the 3D reflection image generated using the AIDA array (Fig. 5.25b) recovers much smaller sections of both structures with much reduced amplitudes. Both 3D images are displayed as viewed from the southeast. Another important aspect of generating this VSP depth images is that we obtain a reflection angle value for each sample in each trace in the profile. This allows us to gain some insight into how much is spatial aliasing an issue. Inspection of images containing reflection-angle information for the AIDA array shows that most of the energy arrives at angles smaller than 40º. As discussed in section 2 of this manuscript, upward propagating arrivals with angles larger than ~38º will suffer spatial aliasing with the spacing of the AIDA array. This implies that spatial aliasing is not a major problem for the AIDA receiver array.

The quality of our reflection images clearly depends upon illumination which is a strong function of the source and receiver distributions, as well as the geometry of the geologic structures being imaged. Of these parameters we have control only over the receiver geometry. The illumination analyses above (Figs 5.22 and 5.25)

emphasize the importance of recording with true 2D surface arrays rather than simple linear profiles, not only in terms of avoid aliasing the seismic wavefield, but to avoid aliasing the imaged structure.

5.8 Discussion

In this manuscript we have shown how microearthquake recordings when treated as VSP surveys can be used as illumination sources for 3D reflection imaging. The work presented here expands on the work of *Inamori et al.* [1992], and *Quiros et al.* [2015a, 2015b]. In the previous sections we showed how to obtain 3D reflection images that result from mapping and stacking the earthquake waveforms into 3D space. The 3D depth profiles obtained from a single aftershock and 13 events show very clear reflectors underneath the receiver array. However, when a larger number of aftershocks (i.e. 200 events) are used, we observe a deterioration of the reflector coherence in the 3D profiles. The most likely causes of the drop in image coherence are the uncertainty in the hypocenters and origin times, and variations in focal mechanisms and source-time function among these events.

From a geological perspective the key result in this manuscript is the imaging of prominent reflectors that represent structure beneath the array. The most important reflector imaged in the depth sections dips between 15 – 30º in a southeast direction (dip azimuth 108 - 155º). This structure shows a clear listric character with a dip of about 30º in its steepest section and about 15º in its more gently dipping section (Fig. 26a). The migrated (blue line) and unmigrated (green line) average positions of the main cluster of seismicity are shown in Fig. 26(a). As the depth image is unmigrated the green dashed line identifies the average location of the unmigrated cluster of

seismicity. After migration, energy along the green dashed line is projected to its true location, the blue dashed line. The main cluster of seismicity is constrained to be a ~1 km thick zone [*Davenport et al.*, 2014; *McNamara et al.*, 2014; *Horton et al.*, 2015; *Wu et al.*, 2015] indicated by the 1 km wide pointers (black lines) shown in Fig. 26a. The black arrow in Fig. 26a shows a section of the main reflector where coherence is degraded, perhaps a result of unmigrated energy.

The imaged reflector almost certainly represents a thrust sheet like those imaged on the I-64 reflection profile [*Harris et al.* 1986; *Pratt et al.* 2014]. Fig 27 shows the depth section obtained by our analysis and the reprocessed migrated I-64 profile of *Pratt et al*. [2014]. Black arrows indicate the locations of prominent reflectors on the I-64 profile. The EP and CF reflectors identified on the I-64 profile (Fig. 5.27b) correspond to the previously interpreted Ellisville Pluton thrust and the Chopawamsic Fault, respectively. While the PxP reflector marks the projected location of the reflector imaged by our analysis on the I-64 profile. As the PxP reflector lies between the interpreted Ellisville Pluton (EP) thrust and the Chopawamsic Fault (CF) (Fig. 5.27b) we interpret it as defining a previously unidentified thrust sheet. Other reflectors such as the Chopawamsic Fault (Fig. 5.27b) is unfortunately not clearly imaged in our depth sections. A weak reflector at ~ 8.5 km depth (black arrow) in Fig. 5.27(a) is possibly the only hint of the Chopawamsic fault that we imaged as most of it lies in the mute region that corresponds to the removal of the S-wave and its coda. Similarly, the Ellisville Pluton thrust is poorly illuminated as not a lot of data is available in our profile in the depth range 2.5 – 4.5 km. The "shadow zone" where P-wave reflections are masked and which affects the retrieval of

the CF reflector could be avoided if three-component data was available. This of course is a limitation of the AIDA geometry and emphasizes the need for full 2D three-component recording arrays that fully span the subsurface of interest.

We have concentrated in the upper crustal reflections as the reprocessed profile by *Pratt et al.* [2014] shows little indication of deep reflectivity, another reason to concentrate in the upper reflections, is the presence of S-wave energy still present in the records even after muting the S-wave and its coda (i.e. S-wave multiples) that could be spatially mapped into the depth images.

An important point to make is that analysis of the reflection angles in the depth images suggests that most upward propagating energy arrives at angles smaller than 40^{o}, implying that spatial aliasing is not a major issue for the AIDA receiver array and the hypocenter distribution.

We have shown here that dense surface arrays can produce reflection images from records of microearthquakes comparable to those obtained by surface, controlled-source reflection techniques using similar station spacing. Although reflection imaging with microseismicity is limited by both the source spectrum and the distribution of microearthquakes, it benefits from imaging along reflection ray paths that experience less attenuation as they travel shorter distances as opposed to ray paths from surface sources. Moreover AIDA involves none of the environmental disturbance and costs associated with controlled sources. We see AIDA as an important adjunct, but not a replacement for surface, controlled source 3D reflection imaging. To properly image the subsurface using AIDA RVSP techniques requires the use of 2D surface arrays with close stations spacing in orthogonal directions with adequate aperture. For

example, a survey that would cover the main aftershock cloud (10 km x 10 km) and that would attempt to minimize spatial aliasing (e.g. $\Delta x = \Delta y = 100$ m) would use approximately 10^4 stations. Although such a survey may appear prohibitive for the sheer number of stations, it is dwarfed by the largest surveys now in use in the oil and gas industry (i.e. 200,000 channels) [*Al-Deen et al.* 2014].

5.9 Conclusions

The Mw 5.8 2011 Virginia earthquake provided a unique opportunity to record an aftershock sequence with high density receiver arrays. The AIDA arrays recorded on the order of 2600 aftershocks during a 12 day period. Many of these events showed coherent phases between the direct P and S arrivals. Based on simple travel-time modeling we interpreted these phases as reflections from an imbricate thrust sequence beneath the array. These reflected arrivals served as the basis for reflection imaging, with the aftershocks as the illumination sources. We have applied VSP processing techniques to the aftershock sources to properly image the volume of interest. The results show a coherent reflector with very clear listric character that dips southeast. This reflector almost certainly corresponds to one of the thrust sheets imaged by previous deep seismic reflection profiles. Other reflectors are outside the area of illumination due to our receiver array geometry and the fact that the direct S-wave and its coda have a "shadow zone" effect on P-wave reflections.

The AIDA experiment has showed how dense arrays are an important alternative to doing reflection imaging with controlled-source surveys, especially in situations where conventional surveys are logistically or economically impractical. However to take full advantage of the VSP approach to earthquake reflection imaging

denser 2D surface arrays are needed. These arrays will play a critical role in minimizing some of the issues discussed in this manuscript such as hypocenter uncertainty and illumination. More importantly, the technology to do these surveys is currently available.

5.10 Figures

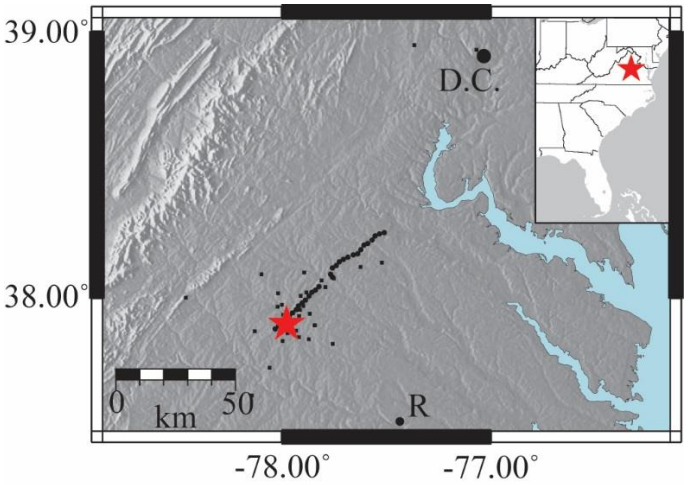

Figure 5.1: Epicenter (red star) of M_w 5.8 Mineral, Virginia earthquake relative to the city of Richmond (R) and the District of Columbia (D.C.). Also shown are all the stations deployed during the post-seismic deployment, including those deployed by other groups. Inset map shows the epicenter of the main shock.

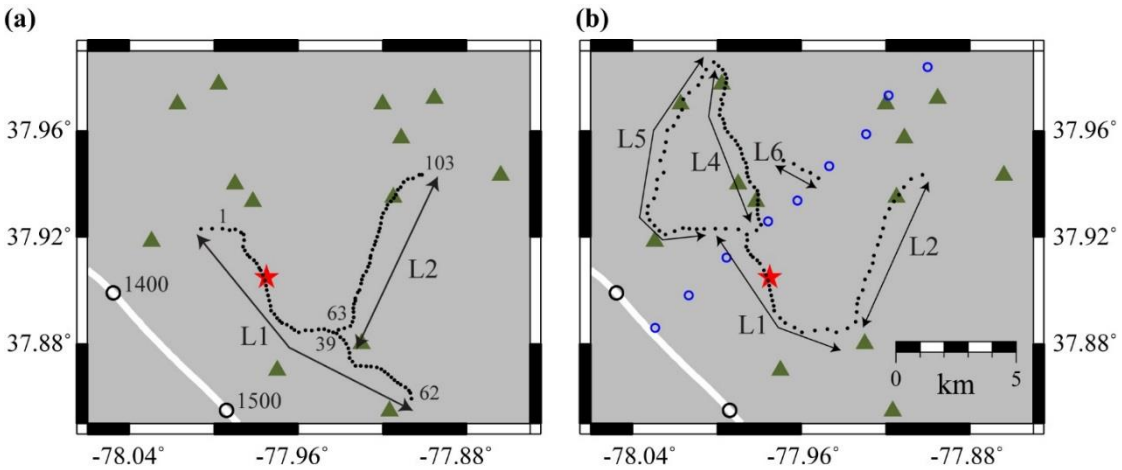

Figure 5.2: (a) Phase 1 of the AIDA deployment showing the mainshock (red star), vertical component seismographs (black dots) deployed on 27 August, 2011. Stations 2 and 3 are to the left of station 1. Profile L1 and L2 were installed along local roads. Also shown is the interstate I-64 along which the USGS collected a deep seismic reflection survey. The black circles indicate the location of source locations of the I-64

USGS profile [*Harris et al.*, 1986]. Green triangles correspond to broadband and short period seismographs deployed by other groups. (b) Phase 2 of the AIDA deployment. This figure shows the vertical component seismographs (black dots) and the 3-component linear seismometer array (blue circles) installed between 1 – 3 September.

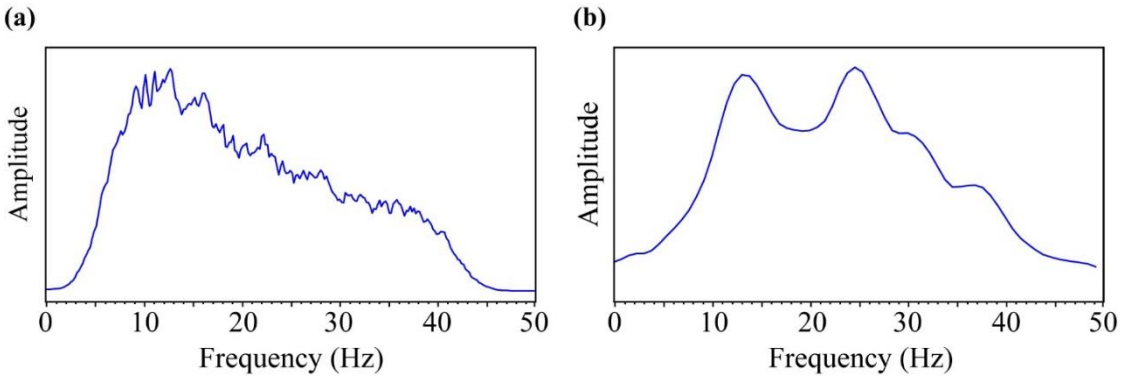

Figure 5.3: (a) Amplitude spectra of a 3.5 s long AIDA record similar to that shown in Fig. 5(b). (b) Amplitude spectra of a 0.2 s long window containing a reflected phase between the direct P and S arrivals similar to those shown in Fig. 7.

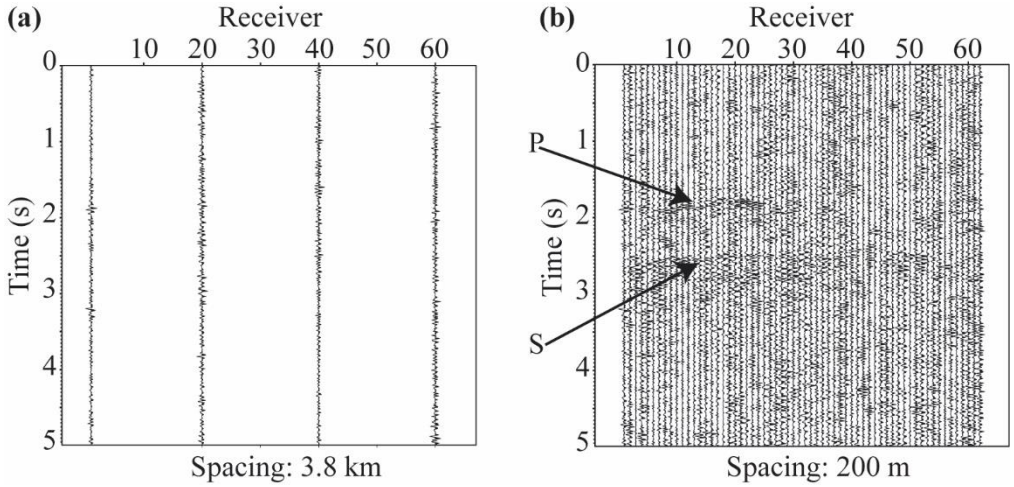

Figure 5.4: (a) Seismograms of 4 stations along line L1 (see Fig. 1b) that mimic what a standard aftershock deployment would record. (b) Seismograms of all 62 stations along line L1 showing the weak but perceptible direct P and S arrivals.

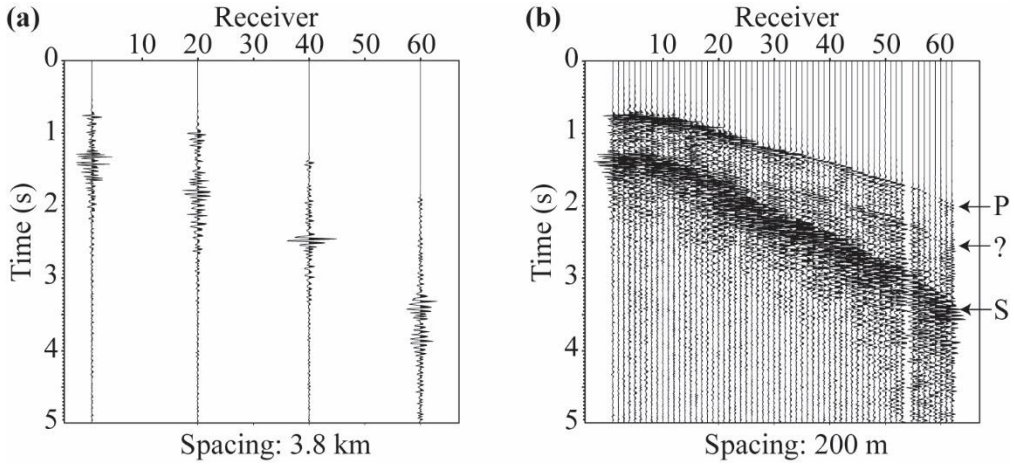

Figure 5.5: (a) Seismograms of 4 stations along line L1 (see Fig. 1b) that mimic what a standard aftershock deployment would record. (b) Seismograms of all 62 stations along line L1 showing an unidentified arrival in addition to the direct P and S arrivals.

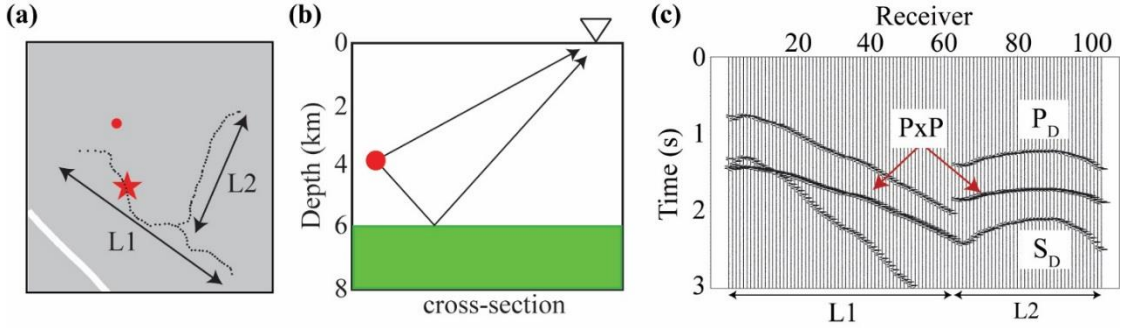

Figure 5.6: (a) Aftershock's epicenter relative to receivers (black dots) and epicenter of mainshock (red star), (b) cartoon of a flat single-layer model used to create a synthetic aftershock record, (c) synthetic aftershock record showing the direct P and S arrivals, and a reflected (PxP) phase from the top of the layer shown in (b), as it would have been recorded by a surface array with the AIDA geometry. Pseudo random noise has been added at a level of 2% from the maximum amplitude in each trace. A 30 Hz zero-phase source wavelet was used for the creation of the synthetics.

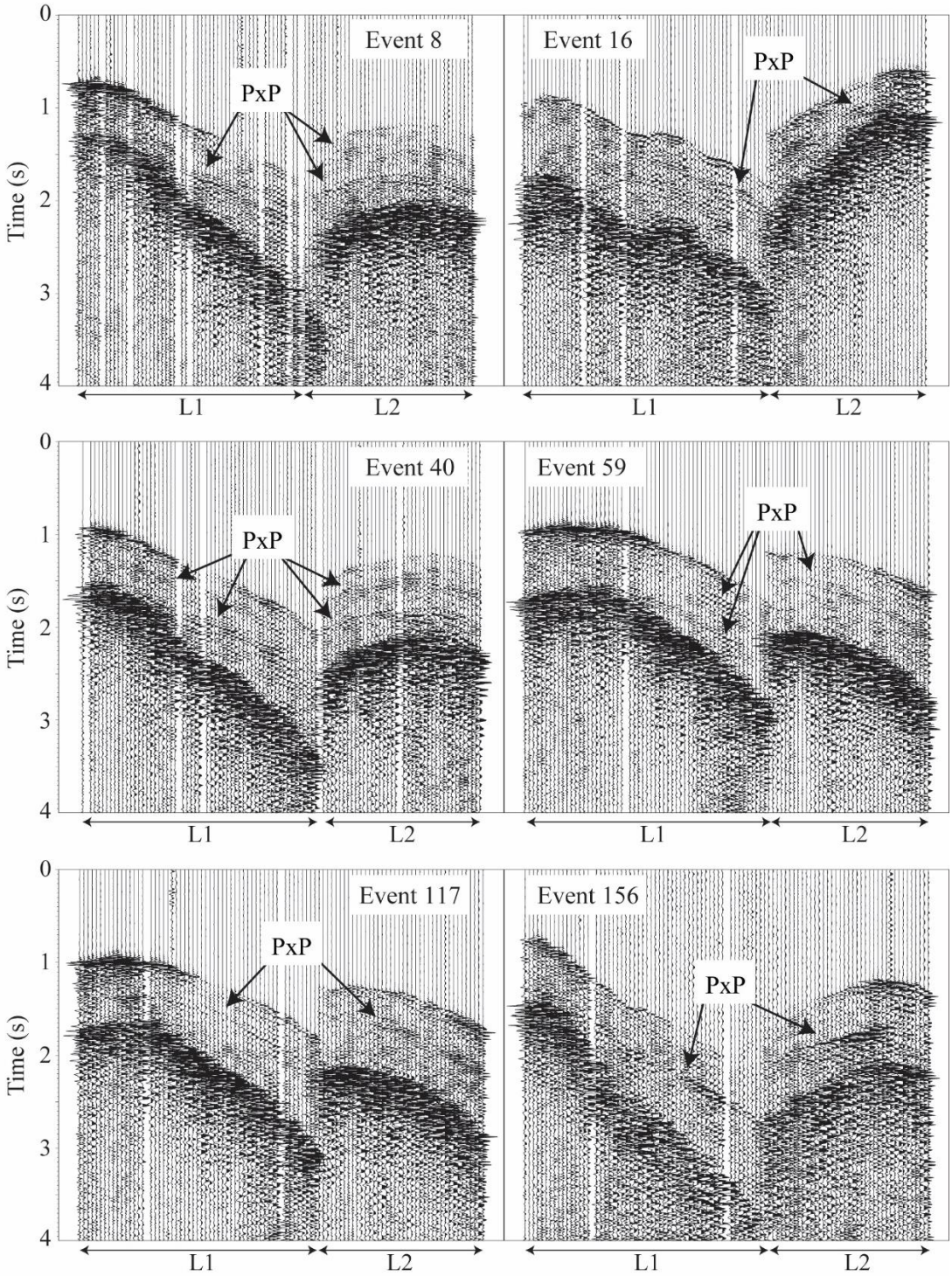

Figure 5.7: Examples of reflections shown in 6 different aftershock records. Each record shows only seismograms for lines L1 and L2 (see Fig. 2a). Reflected arrivals (PxP) are shown in each record.

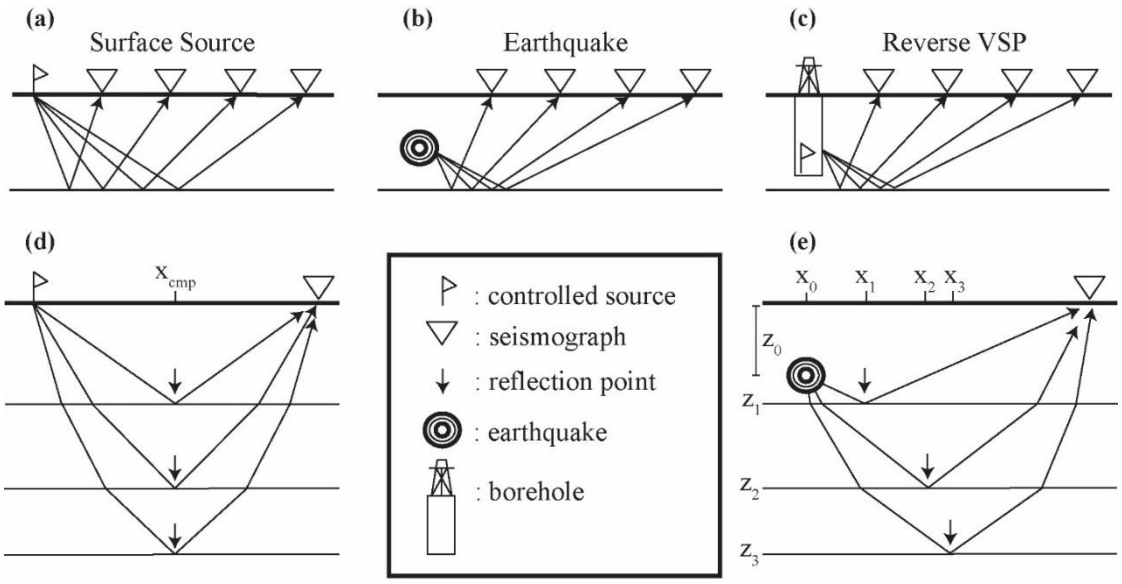

Figure 5.8: Reflection geometry for (a) surface source, (b) a microearthquake and, (c) a reverse VSP survey. (d) Reflection point location for a surface source and horizontal layers. (e) Reflection point location for a source at depth and horizontal layers.

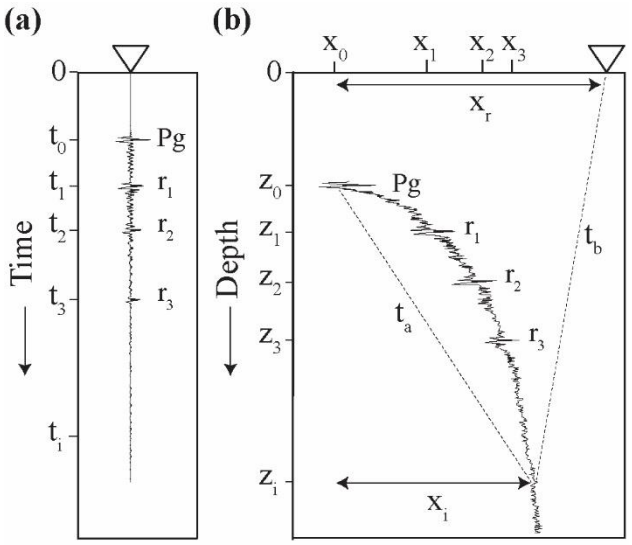

$$v = \sqrt{x_r^2 + z_0^2} / t_0 \ , \quad t_i = t_a + t_b \ , \ \text{let } A_i = \sqrt{(t_i\, v)^2 - z_0^2}$$

$$z_i = \tfrac{1}{2} (A_i + z_0) \qquad x_i = x_r (A_i - z_0) / 2A_i$$

Figure 5.9: (a) Seismic trace as recorded by the receiver in Fig. (5.4e). (b) Seismic trace when mapped into the depth-offset domain by the constant velocity VSP transformation of *Dillon and Thomson* [1984].

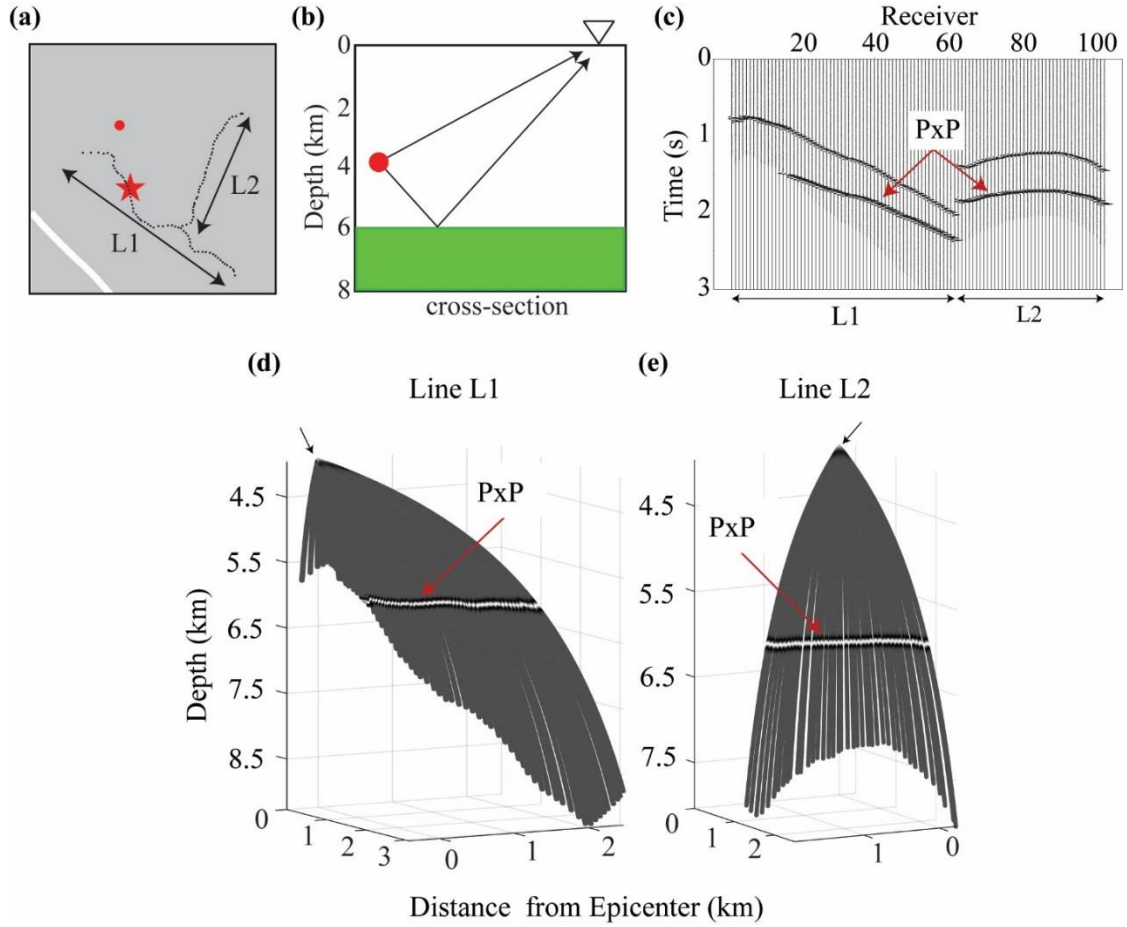

Figure 5.10: (a) Aftershock's epicenter relative to receivers (black dots) and epicenter of mainshock (red star), (b) cartoon of a flat single-layer model used to create a synthetic aftershock record, (c) synthetic aftershock record showing the direct P arrival and the reflected PxP phase. The direct S-wave has been zeroed from the record to avoid mapping it into the reflection image. Pseudo random noise has been added at a level of 2% from the maximum amplitude in each trace. (d) VSP-CDP mapping of line L1 viewed from a 208º azimuth and a 10º elevation. (e) VSP-CDP mapping of line L2 viewed from 118º azimuth and a 10º elevation.

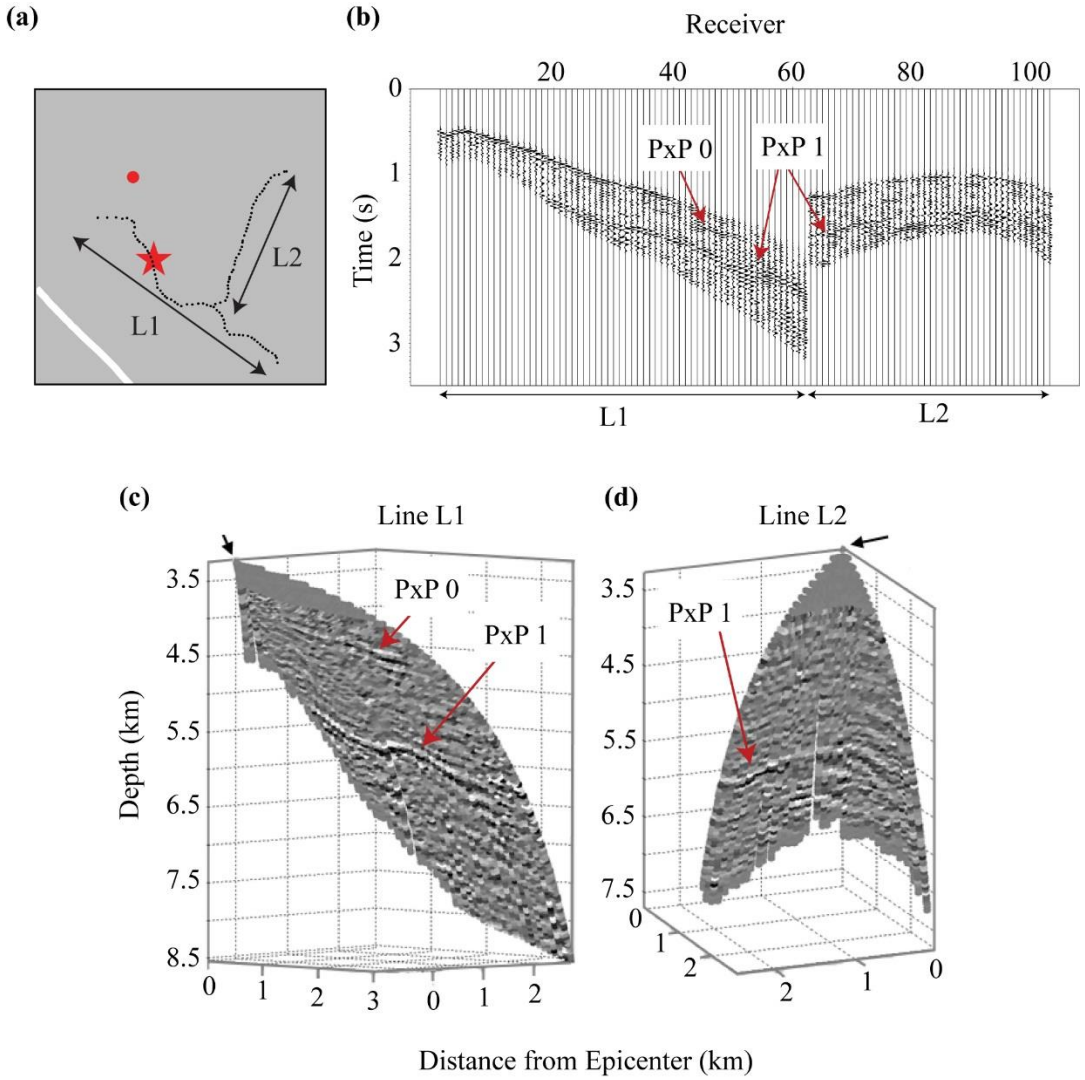

Figure 5.11: (a) Aftershock's epicenter relative to receivers (black dots) and epicenter of mainshock (red star). (b) Aftershock record showing the direct P arrival and reflected PxP phases. The direct S-wave has been zeroed from the record to avoid mapping it into the reflection image. Amplitudes arriving before the direct P-wave have been zeroed. (c)VSP-CDP mapping of line L1 viewed from a 208º azimuth and a 10º elevation, with first arrivals muted to bring out deeper reflections (PxP). Two reflected arrivals (PxP) are shown. (d) VSP-CDP mapping of line L2 viewed from 118º azimuth and a 10º elevation, with first arrivals muted to bring out deeper reflections (PxP).

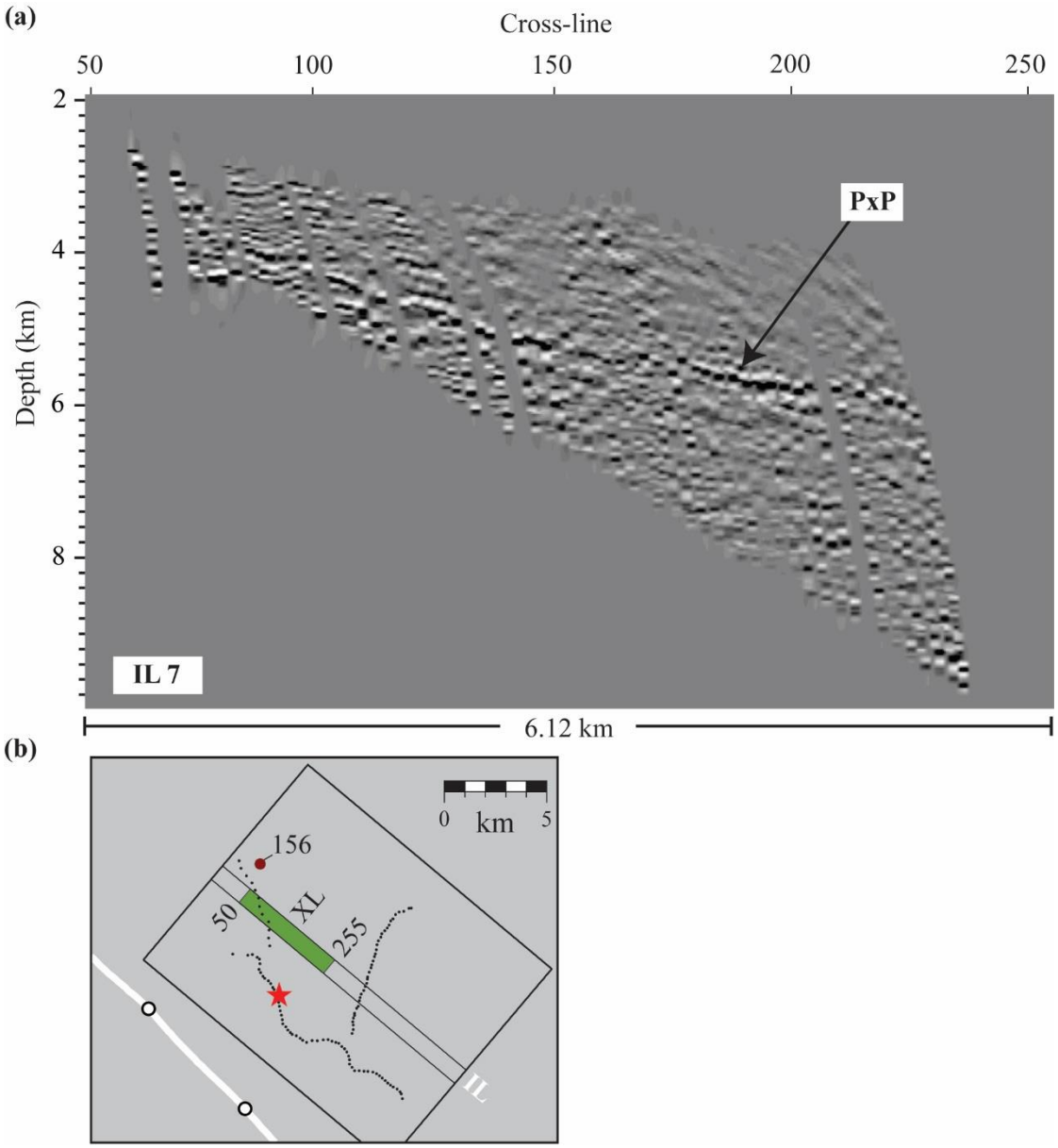

Figure 5.12: (a) VSP-CRP in-line mapping of a single aftershock. A clear reflector (PxP) is indicated in the figure. (b) Orientation of the profile in (a) with the aftershock epicenter (red dot) and mainshock (red star) shown.

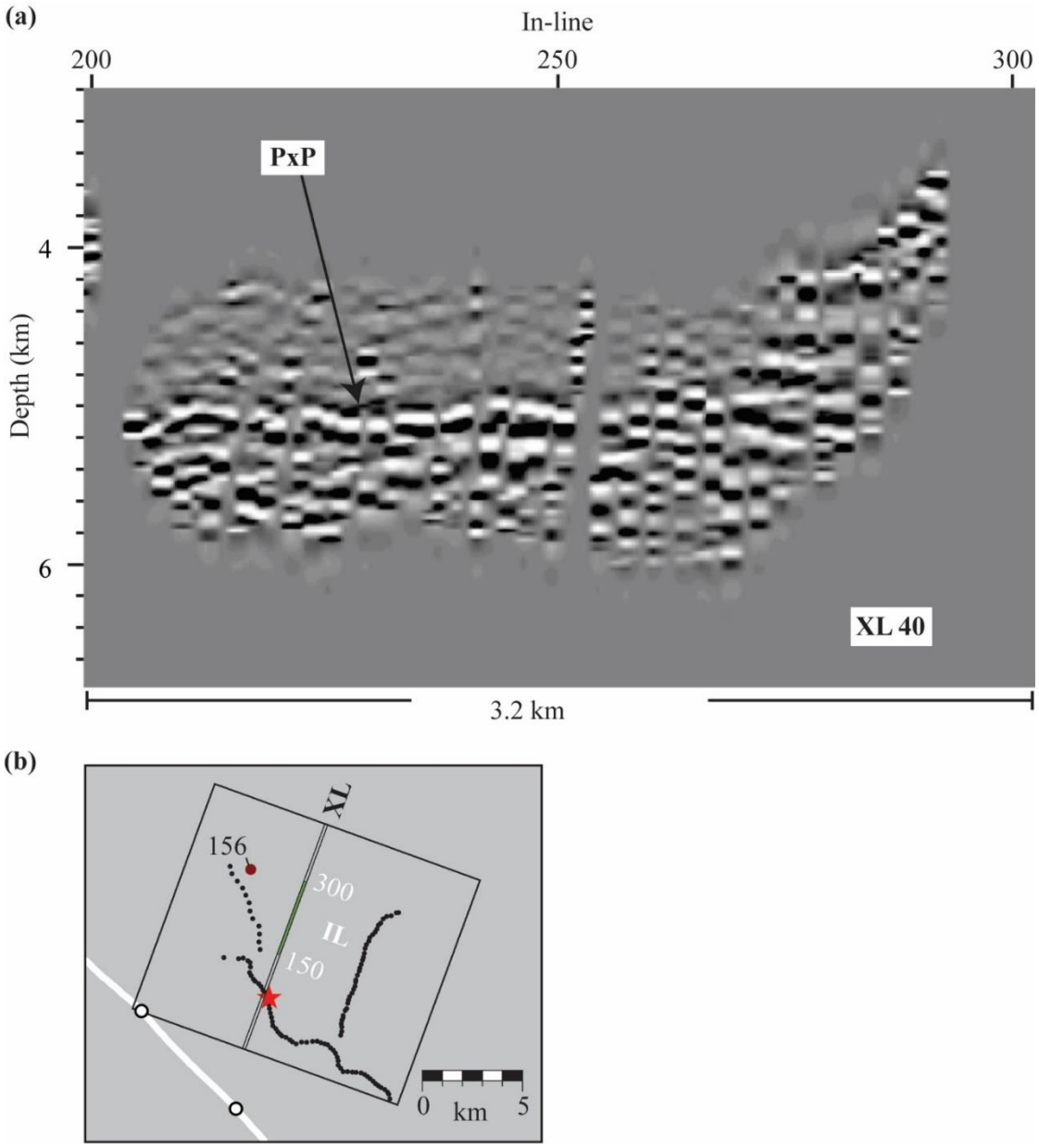

Figure 5.13: (a) VSP-CRP cross-line mapping of a single aftershock. A clear reflector (PxP) is indicated in the figure. (b) Orientation of the profile in (a) with the aftershock epicenter (red dot) and mainshock (red star) shown.

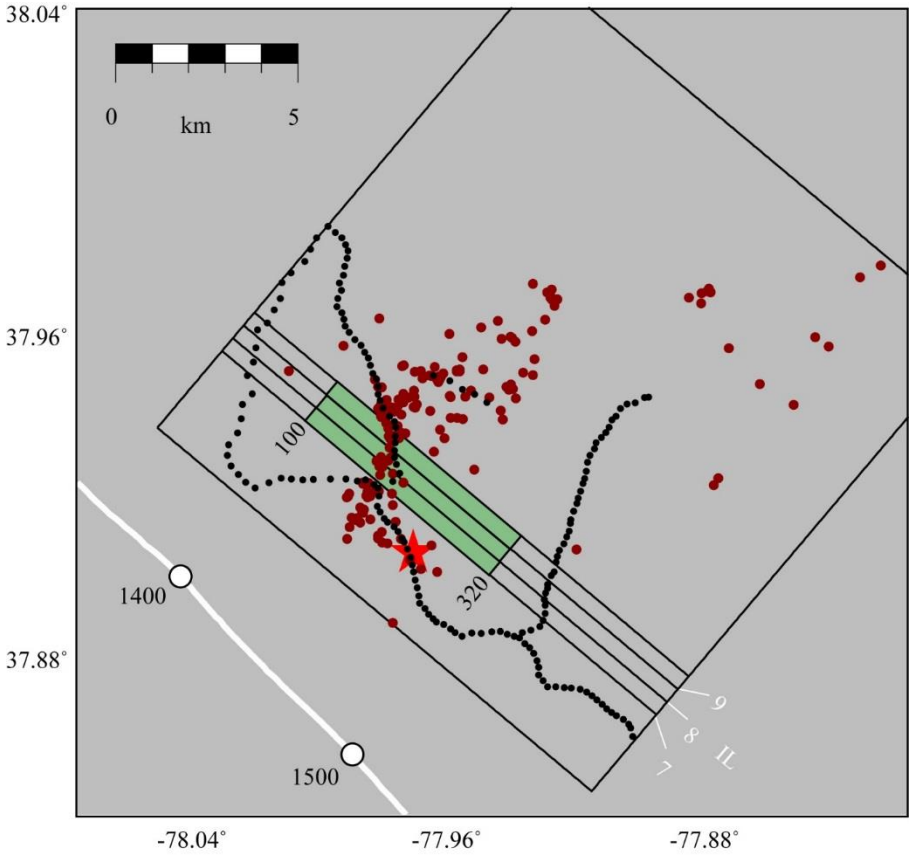

Figure 5.14: Grid orientation used in Fig. 15 showing epicenters of 200 events (red dots) in the *Wu et al.*, [2015] catalog and the mainshock epicenter (red star). The cross-lines (XL) have a 40º azimuth and the in-lines (IL) are orthogonal to the cross-lines. In-lines 7, 8, and 9 and cross-lines 100 and 320 are shown in the map. The grid cell dimensions are 30 m for cross-lines 460 m for in-lines, and 30 m for the vertical size of the grid cells.

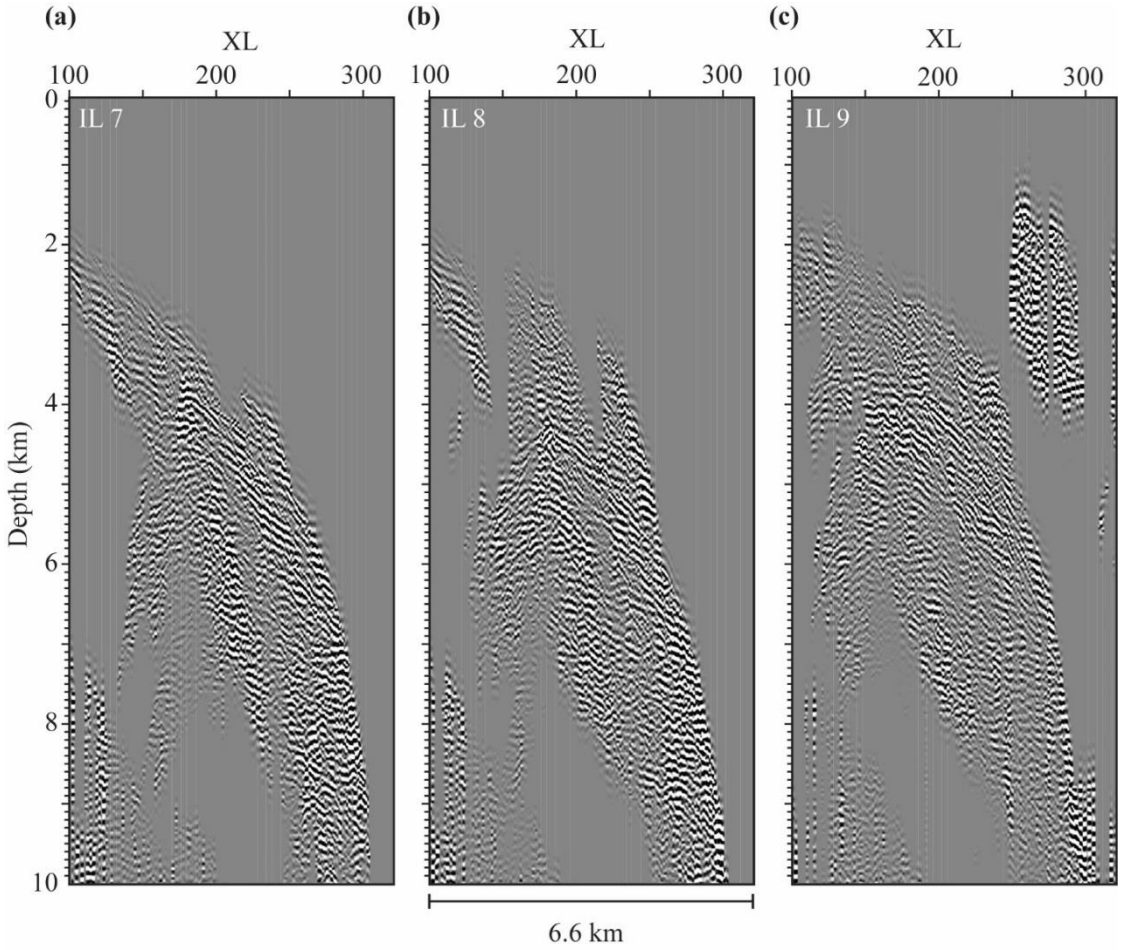

Figure 5.15: Unmigrated VSP-CRP mapping and stacking result for (a) in-line 7, (b) in-line 8, and (c) in-line 9 (see Fig. 14).

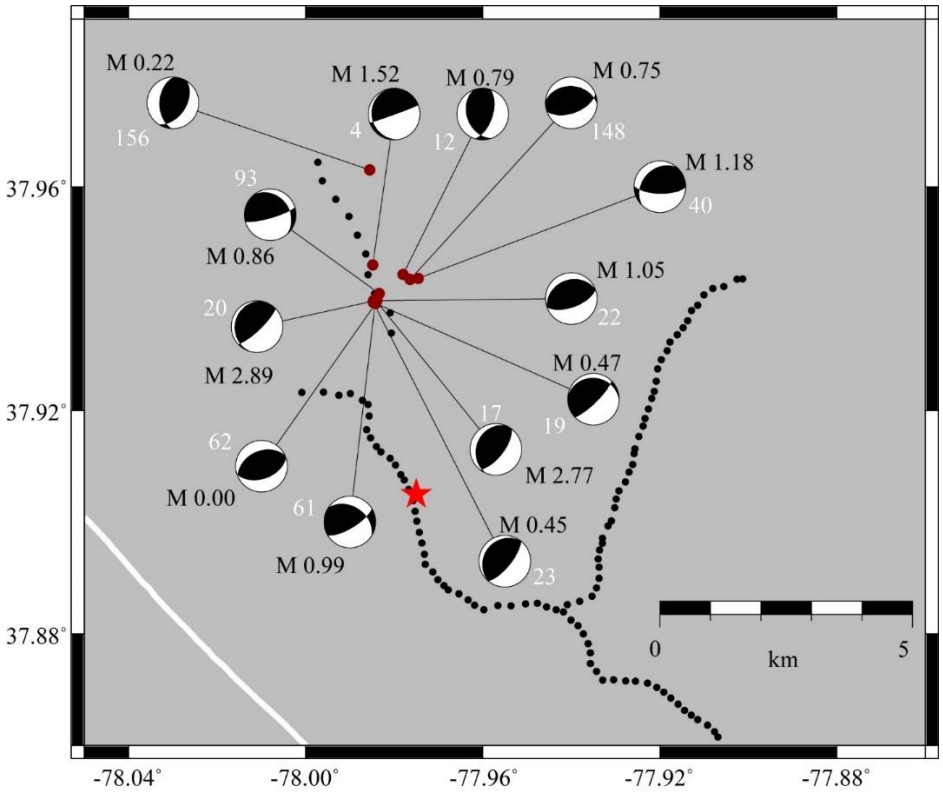

Figure 5.16: Map showing the magnitude, focal mechanisms, and epicenters (*Wu et al.* 2015) of 13 aftershocks recorded with the AIDA stations (black dots) relative to the mainshock epicenter (red star). The event identifier is displayed in white font next to its corresponding focal mechanism. The magnitude is displayed in black font. The depth for the aftershocks are as follows: 2560 m (event 4), 4350 m (event 12), 4380 m (event 17), 4370 m (event 19), 4320 m (event 20), 4230 m (event 22), 4310 m (event 23), 4580 m (event 40), 4250 m (event 61), 4430 m (event 62), 4100 m (event 93), 4540 m (event 148), and 1560 m (event 156).

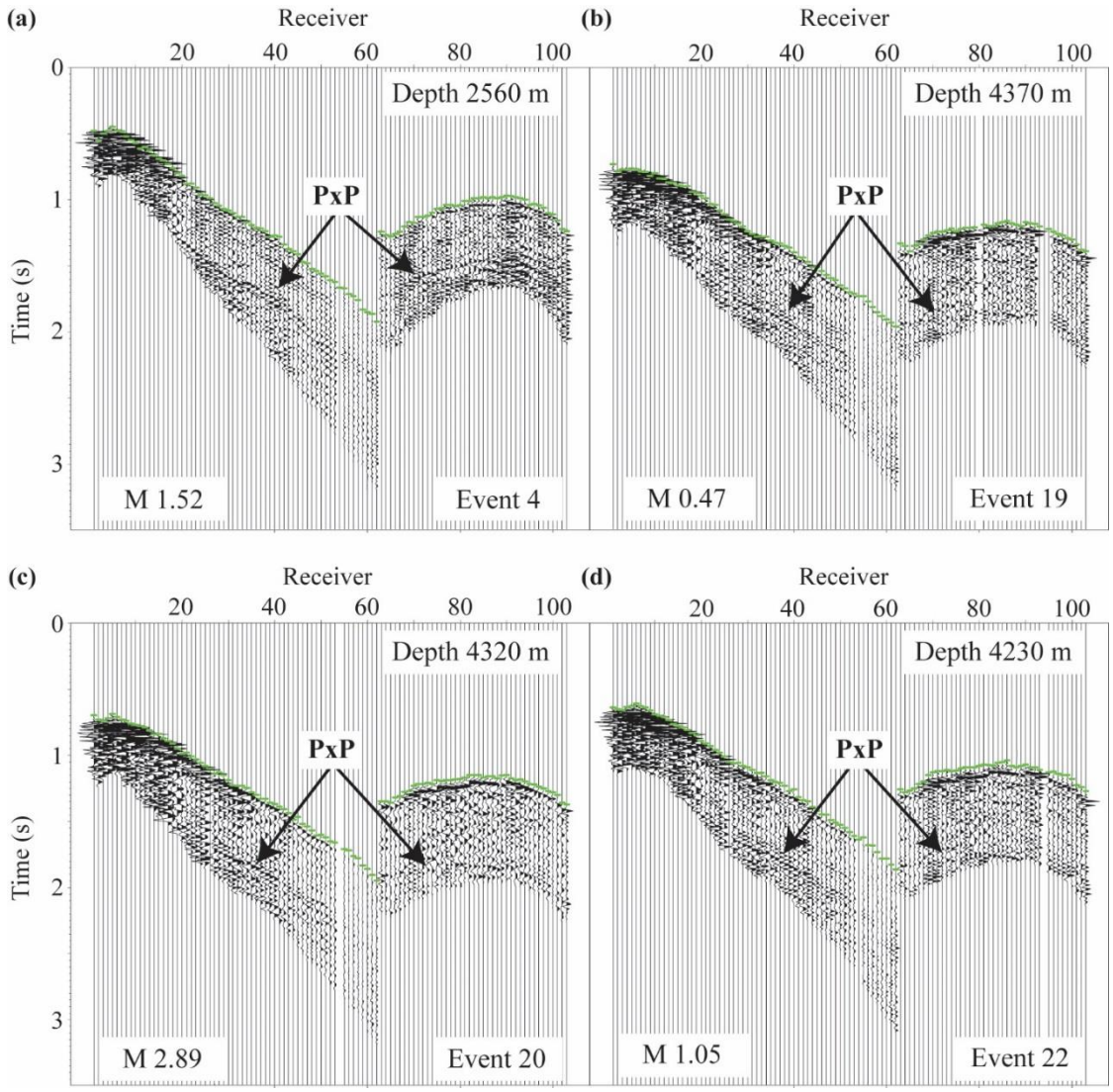

Figure 5.17: Seismograms of 4 aftershocks listed in Fig. 16 showing records for lines L1 and L2. Each figure shows the depth, magnitude, event number, first break picks (dashed green lines), and the most prominent reflector (PxP) in each record.

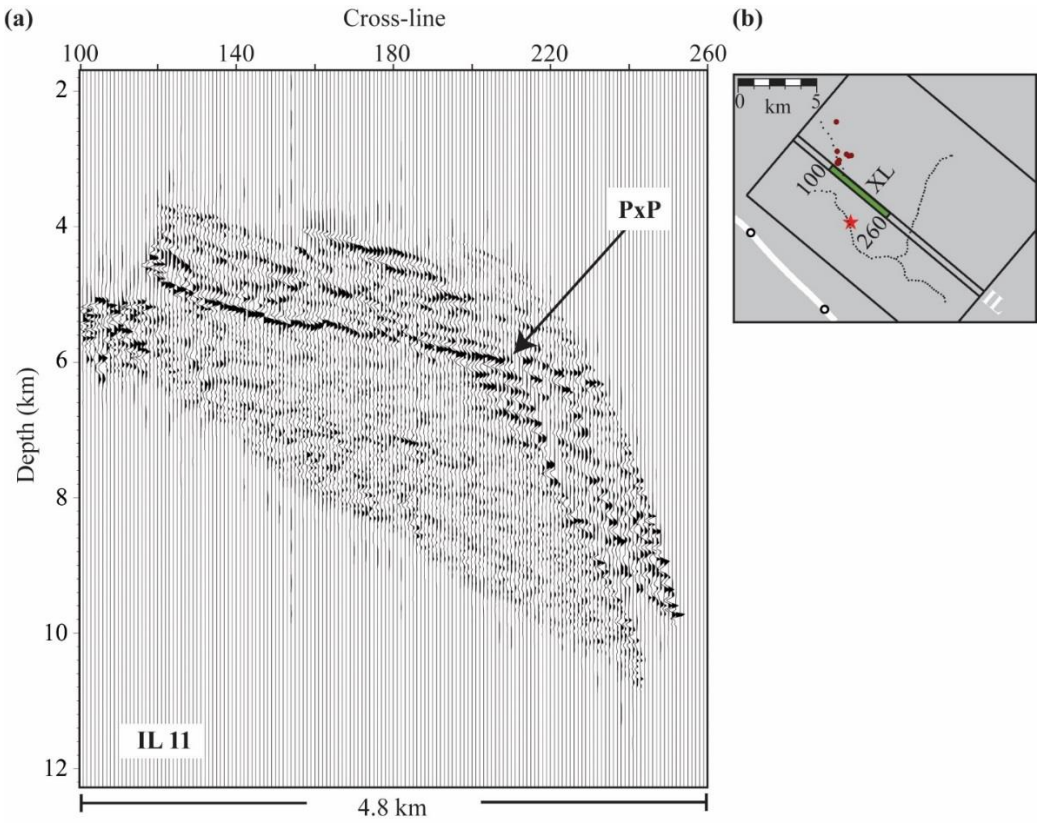

Figure 5.18: (a) VSP-CRP mapping and stacking result for the subset of 13 events shown in Fig. 16. The figure has a horizontal exaggeration of 2.2x. Also shown are the most prominent reflector (PxP) in the profile. (b) Orientation of the profile in (a).

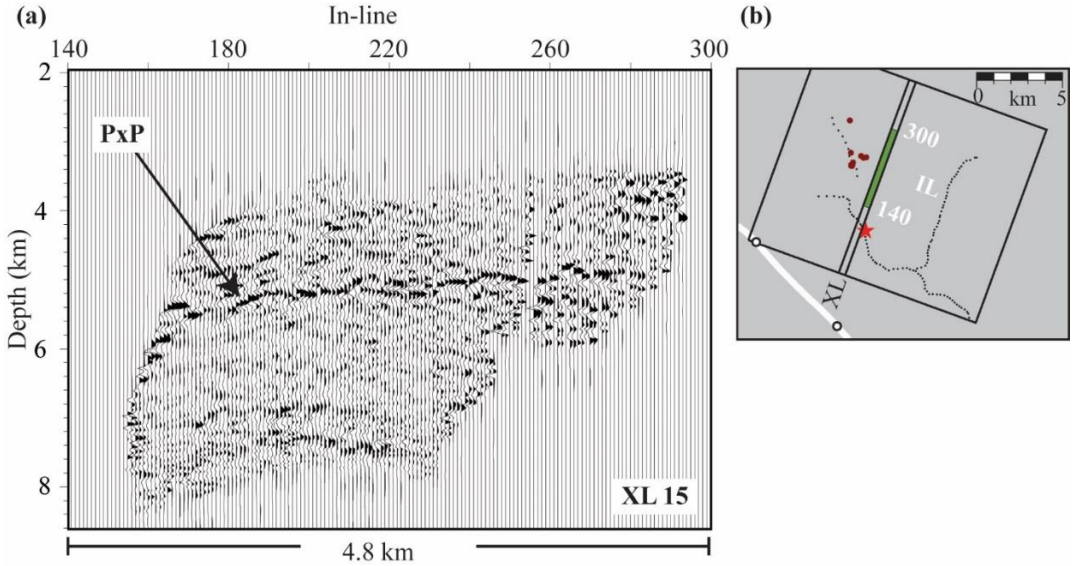

Figure 5.19: (a) VSP-CRP mapping and stacking result for the subset of 13 events shown in Fig. 16. The figure has a horizontal exaggeration of 1.2x. The most prominent reflector (PxP) is indicated in the profile. (b) Orientation of the profile in (a).

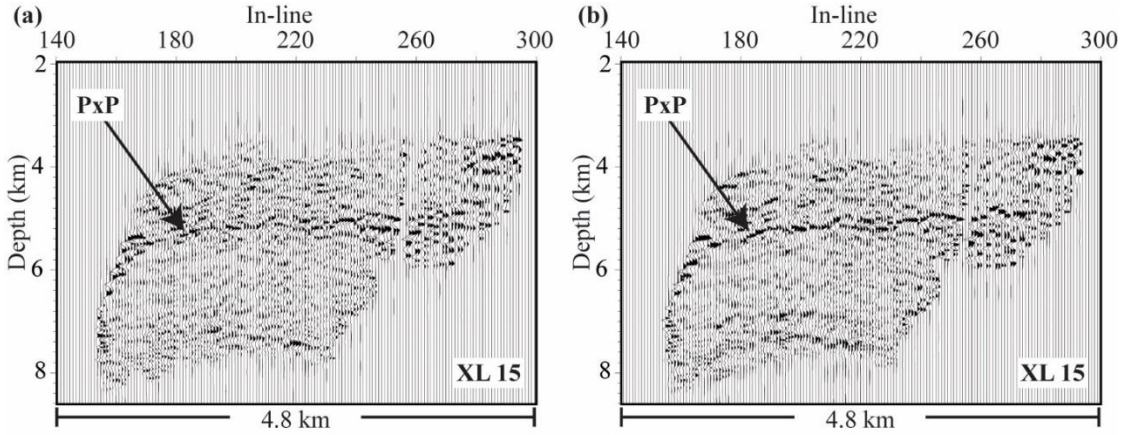

Figure 5.20: Example of how deconvolution improves the coherence of the reflector. (a) VSP-CRP mapping and stacking result of the 13 events in Fig. 16 without the application of deconvolution in the pre-processing sequence. (b) VSP-CRP mapping and stacking result with deconvolution as one of the pre-processing steps applied.

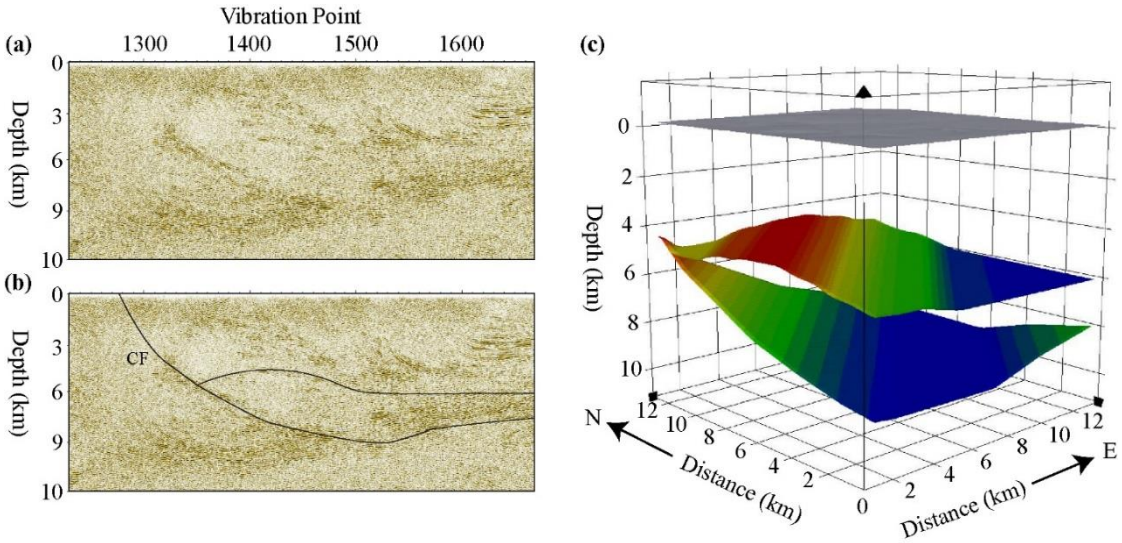

Figure 5.21: (a) Upper 10 km of the processed USGS I-64 profile [*Pratt et al.*, 2014]. (b) Same as in (a) with two structures marked for the creation of a 3D structural model (see text for discussion). (c) The simplified 3D structural earth model to be used in the illumination analyses.

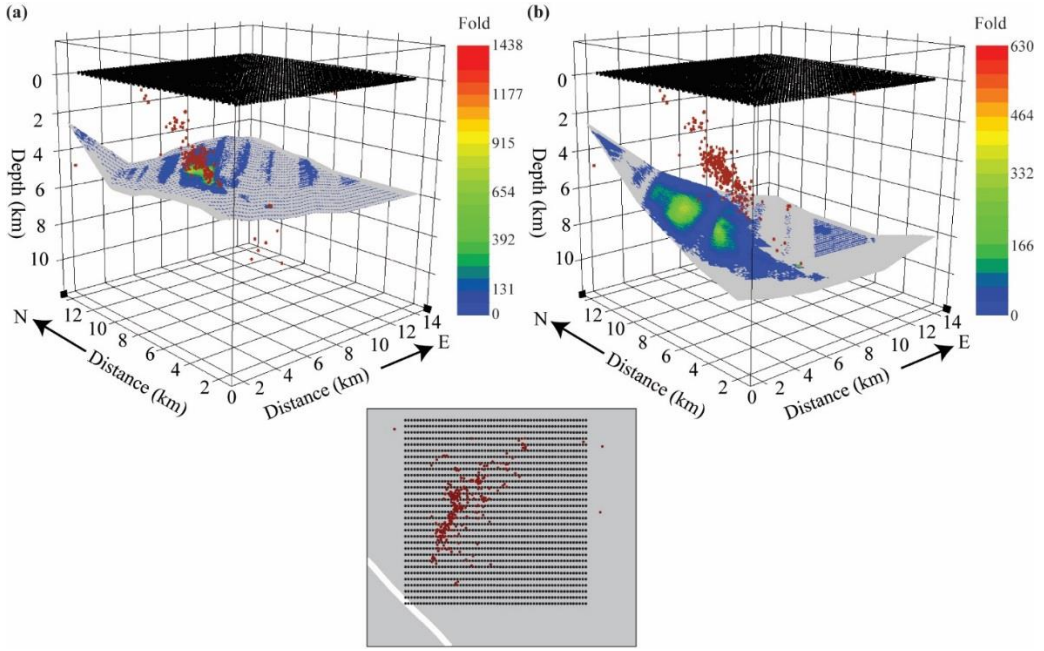

Figure 5.22. (a) Illumination analysis of the antiformal structure (Figs 21b and 21c) using the aftershock distribution and a 2D surface receiver array. (b) Illumination analysis of the CF structure (Figs 21b and 21c) using the same source and receiver geometry as in (a). Map shows the receiver array (black dots) geometry relative to the aftershock distribution (red dots).

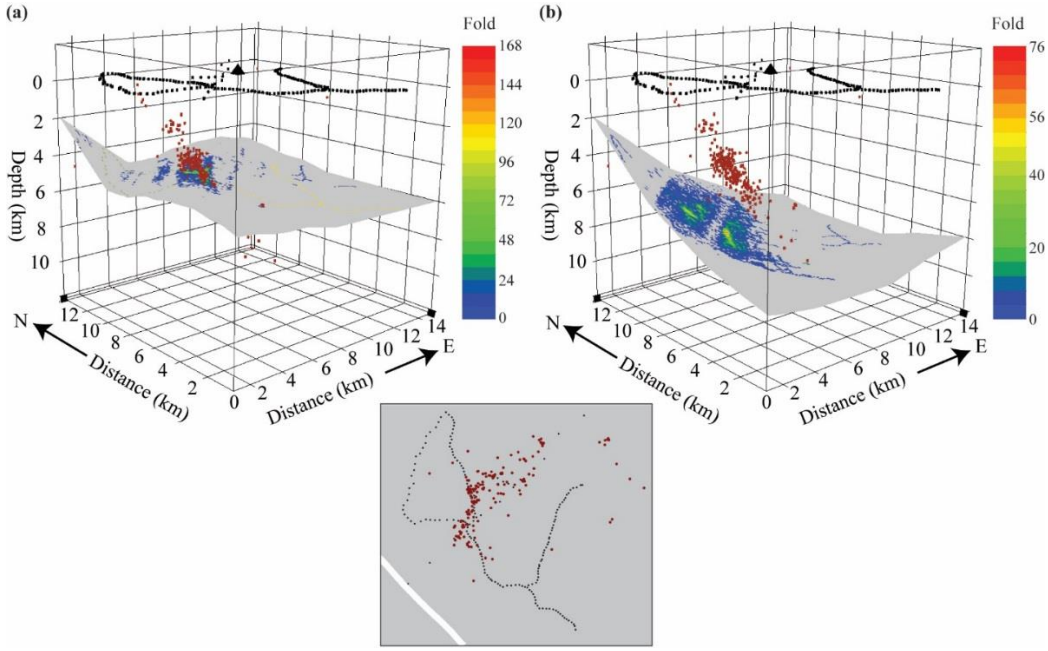

Figure 5.23: (a) Illumination analysis of the antiformal structure using the aftershock distribution and the AIDA receiver array. (b) Illumination analysis of the CF structure using the same source receiver geometry as in (a). Map shows the receiver array (black dots) geometry relative to the aftershock distribution (red dots).

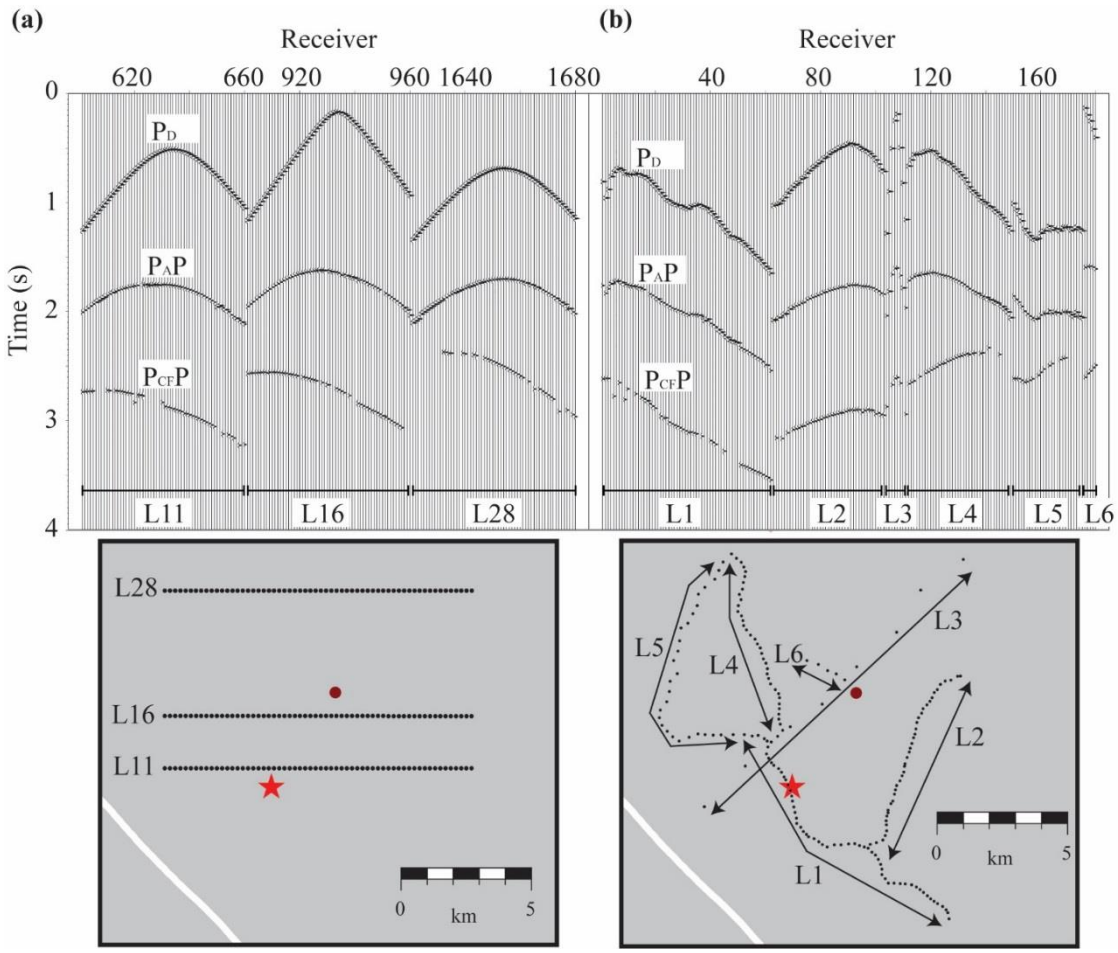

Figure 5.24: Synthetic seismograms. (a) Records for three lines of stations (black dots) of the 2D surface receiver array. Map below shows locations of receivers (black dots), the source (red dot) and the location of the mainshock (red star) for reference. (b) Synthetic seismograms for all vertical component seismometers in the AIDA deployment. Map below shows locations of receiver lines (black dots), the same source location as in (a) and, the location of the mainshock (red star) for reference. Arrivals are indicated with P_D for the direct P-wave, primary reflection of the antiformal structure (P_AP), and primary reflection of the CF structure ($P_{CF}P$).

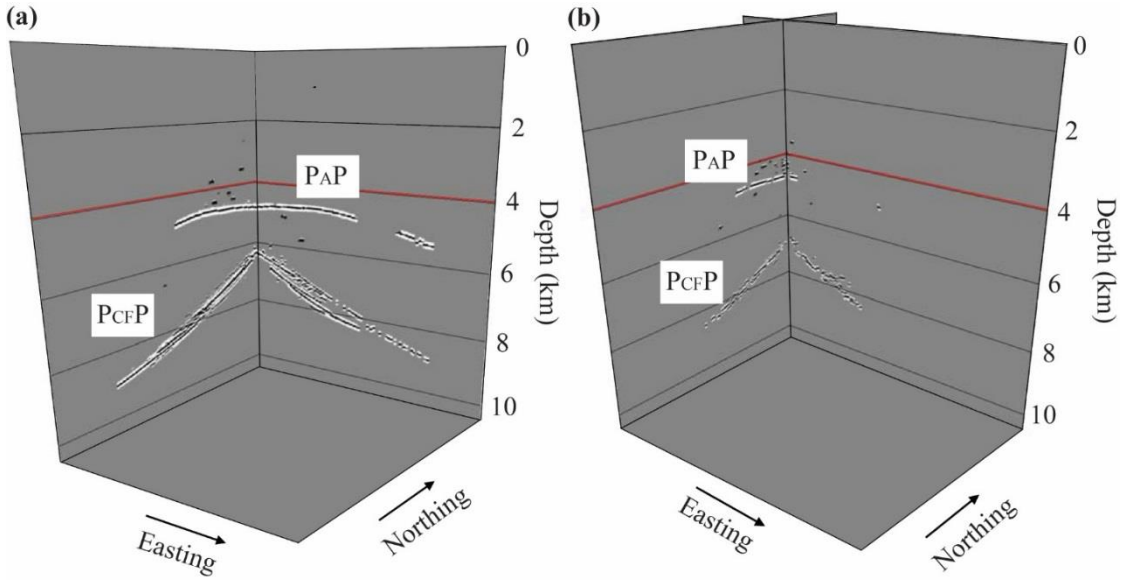

Figure 5.25: Result of applying the VSP-CRP mapping and stacking process to (a) synthetic seismograms generated with the structural model in Fig. 21(c), the aftershock cluster, and the 2D array stations (Fig. 24a), and (b) to synthetic seismograms generated with the same structural model and source distribution, but using a AIDA surface array as shown in Fig. 24(b).

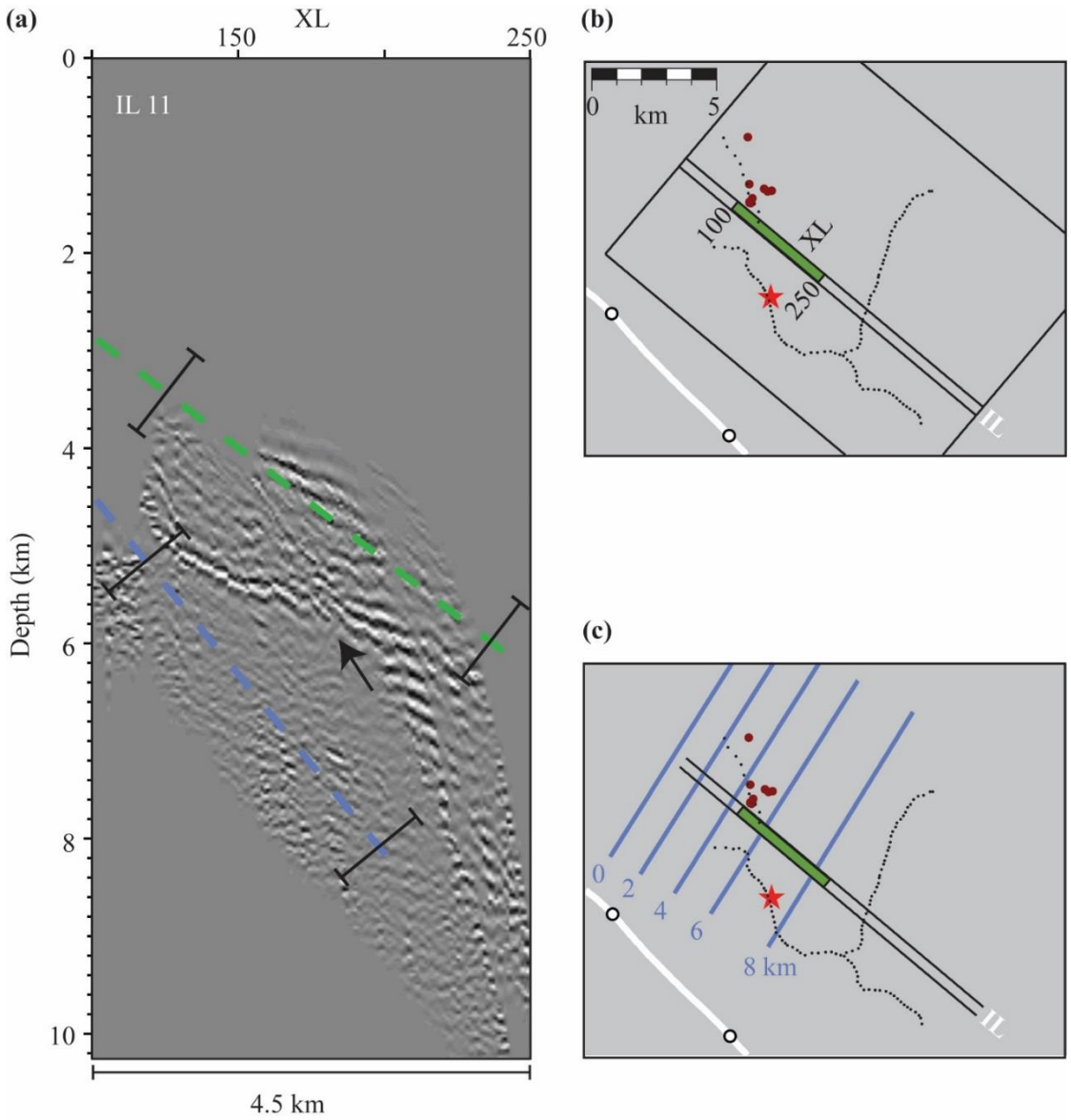

Figure 5.26: (a) Unmigrated VSP-CRP mapping and stacking result for the subset of 13 events shown in Fig. 16. The unmigrated fault projection (dashed green line) is shown relative to its migrated position (dashed blue line) with apparent dip of 47.38º along a 130º azimuth. (b) Orientation of the profile in (a). (c) Same as (b) with the contours of the fault plane by *Wu et al.* [2015].

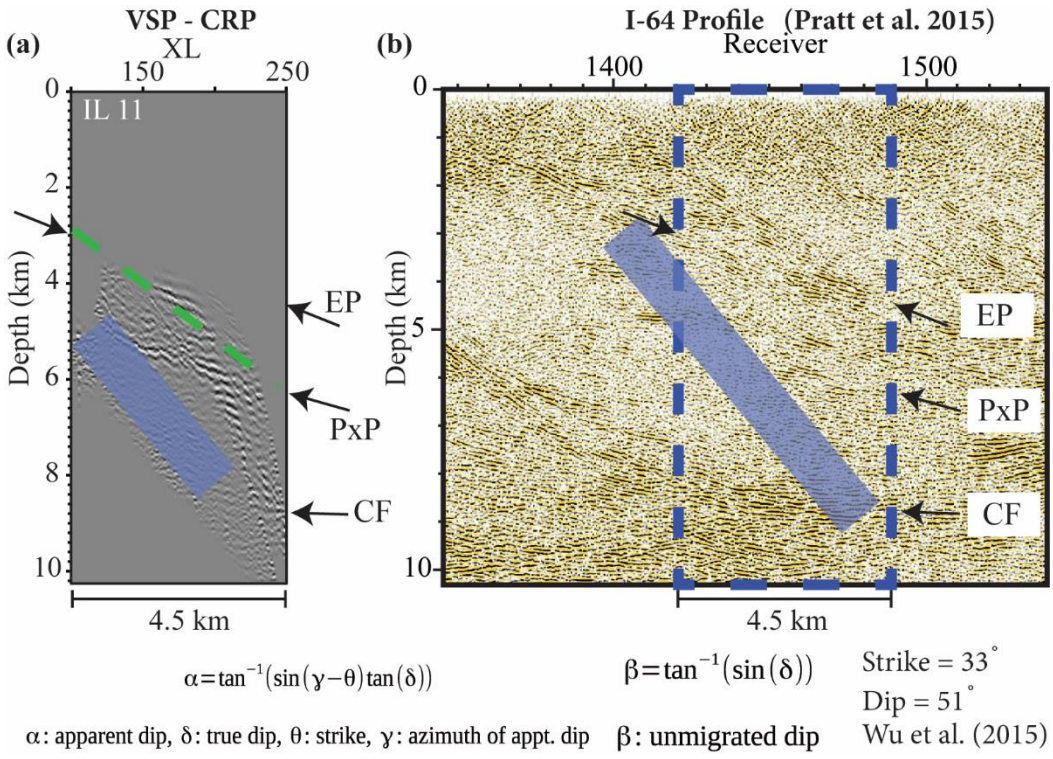

Figure 5.27: (a) VSP-CRP mapping and stacking result for the subset of 13 events shown in Fig. 16. Also shown are the location of reflectors shown in the *Pratt et al.* [2014] reprocessed profile. The unmigrated fault zone projection (green dashed line) and the aftershock zone (blue rectangle) are shown. The reflectors correspond to the Ellisville Pluton (EP), the Chopawamsic Fault (CF), and the PxP event recovered in the analysis presented in this chapter. (b) Top 10 km of the USGS I-64 profile reprocessed by *Pratt et al.* [2014]. Dashed blue box indicates SW projection of (a). Ellisville Pluton (EP), Chopawamsic Fault (CF) and the PxP reflectors are shown. The aftershock zone (blue rectangle) is also shown.

REFERENCES

Al-Deen, K. S., B. Al-Ajmi, W. Zahran, K. S. El-Din, G. Rashed, M. Helal, and M. Hamel (2014), Operating the Largest High Channel Count 3D-Land Survey in Kuwait; Challenges and Success, Society of Exploration Geophysicists.

Brown, L., M. Barazangi, S. Kaufman, and J. Oliver (1986), *The first decade of COCORP: 1974–1984*, Wiley Online Library.

Brown, L. D., P. A. Krumhansl, C. E. Chapin, A. R. Sanford, F. A. Cook, S. Kaufman, J. E. Oliver, and F. S. Schilt (1979), COCORP seismic reflection studies of the Rio Grande rift, *Rio Gd. Rift Tecton. Magmat.*, 169–184.

Brown, L. D. et al. (2011), Aftershock Imaging with Dense Arrays (AIDA) following the August 23, 2011, Mw 5.8, Virginia Earthquake: Feasibility Demonstration and Preliminary Results, *AGU Fall Meet. Abstr.*, *1*, 6.

Byerly, K., L. Brown, B. Voight, and V. Miller (2010), Reflection imaging of deep structure beneath Montserrat using microearthquake sources, *Geophys. Res. Lett.*, *37*, doi:10.1029/2009GL041995.

Chapman, M. C. (2013), On the Rupture Process of the 23 August 2011 Virginia Earthquake, *Bull. Seismol. Soc. Am.*, *103*(2A), 613–628, doi:10.1785/0120120229.

Chavarria, J. A., P. Malin, R. D. Catchings, and E. Shalev (2003), A look inside the San Andreas fault at Parkfield through vertical seismic profiling, *Science*, *302*(5651), 1746–1748.

Chávez-Pérez, S., and J. N. Louie (1995), Seismic reflection views of a blind thrust fault system using earthquake data PP2. 5,

Chávez-Pérez, S., and J. N. Louie (1998), Crustal imaging in southern California using earthquake sequences, *Tectonophysics*, *286*(1), 223–236.

Çoruh, C., G. A. Bollinger, and J. K. Costain (1988), Seismogenic structures in the central Virginia seismic zone, *Geology*, *16*(8), 748–751.

Cox, M. (1999), *Static Corrections for Seismic Reflection Surveys*, Geophysical References Series, Society of Exploration Geophysicists.

Davenport, K., J. Hole, D. A. Quiros, L. D. Brown, M. C. Chapman, L. Han, and W. Mooney (2014), Aftershock imaging using a dense seismometer array (AIDA) after the 2011 central Virginia earthquake, edited by J. W. Horton Jr., M. C. Chapman, and R. A. Green, *Geol. Soc. Am. Spec. Pap.*, *The 2011 Mineral, Virginia Earthquake and its Significance for Seismic Hazards in Eastern North America* (509).

Dillon, P. B., and R. C. Thomson (1984), Offset Source VSP Surveys and Their Image Reconstruction, *Geophys. Prospect.*, *32*(5), 790–811.

Doi, I., and K. 'ya Nishigami (2007), Three-dimensional distributions of S wave reflectors in the source region of the 2000 Western Tottori Earthquake, *Geophys. Res. Lett.*, *34*(20), L20312, doi: 10.1029/2007GL031169.

Fessenden, R. A. (1917), *Method and apparatus for locating ore-bodies.*, Google Patents.

Gutenberg, B. (1951), *Internal constitution of the earth*, Dover Publications.

Hardage, B. A. (2000), *Vertical seismic profiling: Principles*, Handbook of Geophysical Exploration: Seismic Exploration, 3rd ed., edited by K. Helbig and S. Treitel, Elsevier Science, Oxford, UK.

Harris, L. D., W. De Witt Jr, and K. C. Bayer (1986), *Interpretive seismic profile along Interstate I-64 from the valley and ridge to the coastal plain in central Virginia*.

Hatcher Jr, R. D. (1987), Tectonics of the southern and central Appalachian internides, *Annu. Rev. Earth Planet. Sci.*, *15*, 337.

Horiuchi, S., A. Hasegawa, A. Takagi, A. Ito, M. Suzuki, and H. Kameyama (1988), Mapping of a melting zone near Mt. Nikko-Shirane in northern Kanto, Japan, as inferred from S$\times$ P and S$\times$ S reflections, *Tohoku Geophys J*, *31*, 43–55.

Horton, J. W., A. K. Shah, D. E. McNamara, S. L. Snyder, and A. M. Carter (2015), Aftershocks illuminate the 2011 Mineral, Virginia, earthquake causative fault zone and nearby active faults, *Geol. Soc. Am. Spec. Pap.*, *509*, 253–271, doi:10.1130/2015.2509(14).

Horton Jr, J. W., and R. A. Williams (2012), The 2011 Virginia earthquake: What are scientists learning, *Eos Trans. Am. Geophys. Union*, *93*(33), 317–318.

Hughes, K. S., J. P. Hibbard, and B. V. Miller (2013), Relationship between the Ellisville pluton and Chopawamsic fault: Establishment of significant Late Ordovician faulting in the Appalachian Piedmont of Virginia, *Am. J. Sci.*, *313*(6), 584–612, doi:10.2475/06.2013.03.

Iidaka, T., K. Miura, and A. Ikami (1993), Evidence for the existence of a mid-crustal reflector in the Beppu-Shimabara Graben, Kyushu, Japan, *Geophys. Res. Lett.*, *20*(16), 1699, doi: 10.1029/92GL02800.

Inamori, T., S. Horiuchi, and A. Hasegawa (1992), Location of Mid-Crustal Reflectors by a Reflection Method Using Aftershock Waveform Data in the Focal Area of the 1984 Western Nagano Prefecture Earthquake., *J. Phys. Earth*, *40*(2), 379–393.

James, D. E., T. J. Clarke, and R. P. Meyer (1987), Seismic Studies of the Continental Lithosphere A study of seismic reflection imaging using microearthquake sources, *Tectonophysics*, *140*(1), 65–79, doi:10.1016/0040-1951(87)90140-5.

Jupe, A. J., R. H. Jones, S. A. Wilson, and J. F. Cowles (2003), Microseismic monitoring of geomechanical reservoir processes and fracture-dominated fluid flow, *Geol. Soc. Lond. Spec. Publ.*, *209*(1), 77–86, doi:10.1144/GSL.SP.2003.209.01.08.

Lin, F.-C., D. Li, R. W. Clayton, and D. Hollis (2013), High-resolution 3D shallow crustal structure in Long Beach, California: Application of ambient noise tomography on a dense seismic array, *Geophysics*, *78*(4), Q45–Q56.

Malin, P. E., J. A. Waller, R. D. Borcherdt, E. Cranswick, E. G. Jensen, and J. Van Schaack (1988), Vertical seismic profiling of Oroville microearthquakes: velocity spectra and particle motion as a function of depth, *Bull. Seismol. Soc. Am.*, *78*(2), 401–420.

Matsumoto, S., and A. Hasegawa (1996), Distinct S wave reflector in the midcrust beneath Nikko-Shirane volcano in the northeastern Japan arc, *J. Geophys. Res. Solid Earth*, *101*(B2), 3067–3083, doi: 10.1029/95JB02883.

McNamara, D. E., H. M. Benz, R. B. Herrmann, E. A. Bergman, P. Earle, A. Meltzer, M. Withers, and M. C. Chapman (2014), The Mw 5.8 mineral, Virginia, earthquake of August 2011 and aftershock sequence: Constraints on earthquake source parameters and fault geometry, *Bull. Seismol. Soc. Am.*, *104*, doi: 10.1785/0120130058.

Meyer, R. P., and D. E. James (1987), Seismic reflection studies using local earthquake sources, *Geophys. J. Int.*, *89*(1), 27–34, doi:10.1111/j.1365-246X.1987.tb04383.x.

Mizoue, M., I. Nakamura, and T. Yokota (1982), Mapping of an unusual crustal discontinuity by microearthquake reflections in the earthquake swarm area near Ashio, northwestern part of Tochigi Prefecture, central Japan,

Nishigami, K. ’ya (1997), Spatial distribution of coda scatterers in the crust around two active volcanoes and one active fault system in central Japan: Inversion analysis of coda envelope, *Phys. Earth Planet. Inter.*, *104*(1–3), 75–89, doi: 10.1016/S0031-9201(97)00058-7.

Pratt, T. L., J. W. Horton Jr., D. B. Spears, A. K. Gilmer, and D. E. McNamara (2014), The 2011 Virginia M w 5.8 earthquake: Insights from seismic-reflection imaging into influence of older structures on eastern US seismicity, in *The 2011 Mineral, Virginia Earthquake and its Significance for Seismic Hazards in Eastern North America*, edited by J. W. Horton Jr., M. C. Chapman, and R. A. Green, The Geological Society of America.

Quiros, D., L. D. Brown, A. Cabolova, C. Chen, K. Davenport, J. Hole, L. Han, M. C. Chapman, W. Mooney, and others (2015a), Reflection Imaging using Earthquake Sources: A Novel Application of Reverse Vertical Seismic Profiling (RVSP), in *2015 SEG Annual Meeting*, Society of Exploration Geophysicists.

Quiros, D. A., A. Cabolova, L. D. Brown, C. Chen, J. E. Ebel, and J. Starr (2015b), Aftershock Imaging with Dense Arrays (AIDA) Following the Mw 4.0

Waterboro Earthquake of 16 October 2012 Maine, U.S.A., *Seismol. Res. Lett.*, doi: 10.1785/0220140169.

Sanford, A. R., and L. T. Long (1965), Microearthquake crustal reflections, Socorro, New Mexico, *Bull. Seismol. Soc. Am.*, *55*(3), 579–586.

Sanford, A. R., O. Alptekin, and T. R. Toppozada (1973), Use of reflection phases on microearthquake seismograms to map an unusual discontinuity beneath the Rio Grande rift, *Bull. Seismol. Soc. Am.*, *63*(6–1), 2021.

Sbar, M. L., and L. R. Sykes (1973), Contemporary compressive stress and seismicity in eastern North America: an example of intra-plate tectonics, *Geol. Soc. Am. Bull.*, *84*(6), 1861–1882.

Taber, S. (1913), Earthquakes in Buckingham County, Virginia, *Bull. Seismol. Soc. Am.*, *3*(3), 124–133.

Umino, N., H. Ujikawa, S. Hori, and A. Hasegawa (2002), Distinct S-wave reflectors (bright spots) detected beneath the Nagamachi-Rifu fault, NE Japan, *Earth Planets Space*, *54*(11), 1021–1026, doi:10.1186/BF03353295.

Wald, D. J., V. Quitoriano, C. B. Worden, M. Hopper, and J. W. Dewey (2012), USGS "Did You Feel It?" Internet-based macroseismic intensity maps, *Ann. Geophys.*, *54*(6), doi:10.4401/ag-5354.

Wu, Q., M. C. Chapman, and J. N. Beale (2015), The Aftershock Sequence of the 2011 Mineral, Virginia, Earthquake: Temporal and Spatial Distribution, Focal Mechanisms, Regional Stress, and the Role of Coulomb Stress Transfer, *Bull. Seismol. Soc. Am.*, doi: 10.1785/0120150032.

Yilmaz, Ö. (2001), *Seismic data analysis*, Society of Exploration Geophysicists Tulsa.

Zoback, M. D., and M. L. Zoback (1981), State of Stress and Intraplate Earthquakes in the United States, *Science*, *213*(4503), 96–104, doi:10.1126/science.213.4503.96.